UNIVERSITY OF THESSALY

SCHOOL OF ENGINEERING

DEPARTMENT OF MECHANICAL ENGINEERING

Doctor of Philosophy Dissertation

NUMERICAL SIMULATION OF INELASTIC SHELL BUCKLING AND POST-BUCKLING BEHAVIOR

PATRICIA PAPPA

Diploma in Mechanical Engineering, U.Th., 2006

Master of Science (M.Sc.), Department of Mechanical Engineering, U.Th., 2008

Supervisor: *Dr. Spyros A. Karamanos, Professor*

Submitted in Partial Fulfillment
of the Requirements for the degree
of Doctor of Philosophy
Volos 2016

ΠΑΝΕΠΙΣΤΗΜΙΟ ΘΕΣΣΑΛΙΑΣ

ΠΟΛΥΤΕΧΝΙΚΗ ΣΧΟΛΗ

ΤΜΗΜΑ ΜΗΧΑΝΟΛΟΓΩΝ ΜΗΧΑΝΙΚΩΝ

Διδακτορική Διατριβή

ΑΡΙΘΜΗΤΙΚΗ ΕΠΙΛΥΣΗ ΛΥΓΙΣΜΟΥ ΚΑΙ ΜΕΤΑΛΥΓΙΣΜΙΚΗΣ ΣΥΜΠΕΡΙΦΟΡΑΣ ΣΕ ΑΝΕΛΑΣΤΙΚΑ ΚΕΛΥΦΗ

ΠΑΤΡΙΚΙΑ ΠΑΠΠΑ

Διπλωματούχος Μηχανολόγος Μηχανικός, Π.Θ., 2006

Μεταπτυχιακό Δίπλωμα, Τμήμα Μηχανολόγων Μηχανικών, Π.Θ, 2008

Επιβλέπων: *Δρ. Σπύρος Α. Καραμάνος, Καθηγητής*

Διδακτορική Διατριβή

Υπεβλήθη για την εκπλήρωση μέρους

των απαιτήσεων για την απόκτηση

του Διδακτορικού Διπλώματος

Βόλος 2016

NUMERICAL SIMULATION OF INELASTIC SHELL BUCKLING AND POST-BUCKLING BEHAVIOR

Approved by Dissertation Committee:

Dr. Spyros A. Karamanos (Supervisor), Professor,
Department of Mechanical Engineering,University of Thessaly

Dr. Nikolaos Aravas, Professor,
Department of Mechanical Engineering,University of Thessaly

Dr. Antonios E. Giannakopoulos, Professor,
Department of Civil Engineering, University of Thessaly

Dr. Euripidis Mistakidis, Professor,
Department of Civil Engineering, University of Thessaly

Dr. Vlasios K. Koumousis, Professor,
Department of Civil Engineering,National Technical University of Athens

---

Dr. Vassilis Panoskaltsis, Professor,
Department of Civil Engineering,Democritus University of Thrace

---

Dr. Michalis Agoras, Lecturer,
Department of Mechanical Engineering, University of Thessaly

Αντί Προλόγου

Ευχαριστίες

Η εκπόνηση μιας διδακτορικής διατριβής είναι ένας δρόμος στον οποίο βρίσκεσαι αντιμέτωπος με πολλές δυσκολίες, αποτυχίες και απογοητεύσεις. Μέσα όμως από τις δυσκολίες και τις πιο αντίξοες στιγμές αναδύονται πολλές ευκαιρίες, αρκεί να μπορέσουμε να τις αντιληφθούμε. Στη διάρκεια της διδακτορικής μου έρευνας, ένα «ταξίδι» που ξεκίνησε πριν από αρκετά χρόνια, είχα την ευκαιρία να συζητήσω με συναδέλφους, επιστήμονες, ακαδημαϊκούς και φίλους, που ο καθένας από την πλευρά του, εμπλούτιζε τις σκέψεις μου και τις ιδέες μου και φώτιζε διαστάσεις που δεν ήταν πάντοτε άμεσα αντιληπτές από μένα. Σε μία από τις πολλές συζητήσεις, ένας συνάδελφος πριν καιρό, μου ανέφερε μια μικρή, υπαρξιακή αλλά και αστεία ιστορία από το βιβλίο «The Hitchhiker's Guide to the Galaxy» (Γυρίστε τον Γαλαξία με ωτοστόπ) του Adams Douglas. Στην ιστορία αυτή, αναζητείται η "Ύψιστη Απάντηση στη Ζωή, στο Σύμπαν και στα Πάντα", χρησιμοποιώντας τον υπερυπολογιστή *Deep Thought*. Ύστερα από έναν πολύ μεγάλο χρόνο υπολογισμού, ο Deep Thought δίνει την απάντηση "αριθμός 42". Όμως, όταν ρωτήθηκε για να παράσχει την Απόλυτη Ερώτηση στην οποία αναφερόταν η προηγούμενη απάντηση, ο υπολογιστής δεν ήταν επαρκώς ισχυρός για να απαντήσει. Μία ιστορία που θα ήθελα να μοιραστώ γιατί...

όταν τα πράγματα περιπλέκονται, αξίζει τον κόπο να σταθεί κάνεις και να αναλογιστεί: έχω κάνει την σωστή ερώτηση;

Ελπίζοντας να βοηθήσει κι άλλους σε στιγμές αδιεξόδου...

Στη διάρκεια αυτής της προσπάθειας, που ακόμα δυσκολεύομαι να πιστέψω ότι τελειώνει, δεν θα μπορούσα να παραλείψω και να μην ευχαριστήσω όλους όσους με βοήθησαν στην ολοκλήρωση αυτής της διατριβής. Σε όλους όσους αναφέρομαι παρακάτω αλλά και σε όλους εκείνους που είναι αδύνατο να αναφερθώ ονομαστικά, να γνωρίζουν ότι τους ευχαριστώ θερμά για την συνειδητή ή ακόμα και εν αγνοία τους καθοδήγηση (επιστημονική και μη) και τη στήριξή τους, την πολύτιμη και ανιδιοτελή βοήθεια που μου προσέφεραν σε στιγμές αδιεξόδου, θέτοντας σωστές ερωτήσεις και προβληματισμούς.

Πρώτο απ'όλους θα ήθελα να ευχαριστήσω τον καθηγητή μου και μέντορα μου κ. **Σπύρο Καραμάνο**, για τη συνεχή εμπιστοσύνη και στήριξή του κατά την πολυετή συνεργασία μας. Με απόλυτη ελευθερία στις κινήσεις μου και τις επιλογές μου, την σε κάθε βήμα αμέριστη εμπιστοσύνη προς το πρόσωπό μου, αλλά και με την πατρική και διάφανη καθοδήγησή του, κατόρθωσα να επιτύχω τον πιο σημαντικό έως τώρα ακαδημαϊκό στόχο μιας μακράς και επίπονης πορείας. Είναι γεγονός ότι χωρίς το διαρκές ενδιαφέρον του, την επιμονή και υπομονή του, τις γνώσεις του και την εμπειρία του τόσο σε επιστημονικό όσο και σε προσωπικό επίπεδο, η διατριβή αυτή δε θα είχε περατωθεί. Δεν μπορώ παρά να του είμαι υπόχρεη, κυρίως γιατί με επηρέασε ως άνθρωπο με την οπτική του στα πράγματα και τη στάση ζωής του.

Θα ήθελα επίσης, να ευχαριστήσω τα μέλη της εξεταστικής επιτροπής, για τις πολύτιμες παρατηρήσεις και υποδείξεις τους, οι οποίες συνέβαλαν στην βελτίωση του τελικού κειμένου.

Επιπλέον, θα ήθελα επίσης να ευχαριστήσω όλους τους καθηγητές, διδακτορικούς φοιτητές και συναδέλφους μηχανικούς με τους οποίους συνεργάστηκα και με βοήθησαν κατά τη διάρκεια αυτής της έρευνας. Ιδιαίτερα ευχαριστώ τους συναδέλφους μου Σωτηρία Χουλιαρά, Δανιήλ Βασιλική,

Γιώργο Βαρέλη, Αγλαΐα Πουρνάρα, Χάρη Παπαθεοχάρη, Μαρία Βάθη, Γιαννούλα Χατζοπούλου και Γρηγόρη Σαρβάνη για τη συνεργασία τους, τις πολύτιμες υποδείξεις τους και το ενδιαφέρον που έδειχναν κάθε φορά που χρειαζόμουνα τη βοήθεια τους. Παράλληλα θα ήθελα να ευχαριστήσω τους ανθρώπους που μου στάθηκαν και με πίστεψαν σε κάθε μου βήμα, συμβάλλοντας με τον δικό τους τρόπο κι από διαφορετικό πόστο ο καθένας, στην προσπάθεια αυτή που τώρα ολοκληρώνεται.

Για το τέλος άφησα τους σημαντικότερους ανθρώπους στη ζωή μου. Δεν θα μπορούσα να παραβλέψω φυσικά την ίδια μου την οικογένεια, η οποία στεκόταν πάντα δίπλα μου, διακριτικά, σε όλη την διάρκεια κι αυτής της προσπάθειάς. Ήταν οι άνθρωποι που με την ανιδιοτελή αγάπη τους, την υπομονή τους και την αέναη υποστήριξή τους έκαναν τις δύσκολες στιγμές να μοιάζουν ευκολότερες. Επειδή, δεν βρίσκω λόγια να τους εκφράσω την ευγνωμοσύνη και τη χαρά μου, τους υπόσχομαι να το κάνω με έργα, για πάντα. Η εργασία αφιερώνεται σε σας, λοιπόν, που μου μάθατε ότι:

«żeby coś znaleźć, trzeba wiedzieć, czego się szuka»

Τελικά, ο δρόμος που ακολούθησα δεν ήταν διόλου μοναχικός, εκτός από ένα του σημείο. Φέρω ακέραιη την ευθύνη για τις απόψεις που εκφράζονται στη διατριβή και τα λάθη που υπάρχουν είναι όλα δικά μου.

Πατρίτσια Παππά,

Βόλος 2016

It always seems impossible until its done.

Nelson Mandela

NUMERICAL SIMULATION OF INELASTIC SHELL

BUCKLING AND POST-BUCKLING BEHAVIOR

PATRICIA PAPPA

University of Thessaly

Department of Mechanical Engineering

2016

Supervisor: Dr. Spyros A. Karamanos, Professor

Abstract

The research in the present dissertation is aimed at developing advanced numerical tools for the simulation of shell buckling and post-buckling behavior, in the inelastic range. In particular, this work describes the development and the implementation of a J_2 - non-associative plasticity model, which takes into account the "corner-like" effects at the loading point on the yield surface, and is suitable for shell buckling calculations.

It has been widely recognized that although J_2 - flow theory can accurately describe the general material behavior of metal components in the inelastic range, bifurcation predictions based on the J_2 - flow theory may not be reliable in cases where buckling occurs well into the inelastic range. On the other hand, J_2 - deformation moduli may provide a much more reliable prediction of

buckling load on the primary equilibrium path. To account for this discrepancy, several previous works have used the flow theory to trace the load-displacement equilibrium path, while employing the J_2 - deformation theory moduli (instead of the J_2 - flow theory moduli) to detect bifurcation on the primary equilibrium path.

The superiority of J_2 – deformation theory is attributed to the "softer" moduli of the deformation theory, simulating the development of a "vertex" or "corner" (i.e. a high-curvature region on the yield surface at the point of loading on the yield surface), reported in experimental observations in aluminum alloy and steel materials.

The vertex forms on the yield surface at the loading point and this can be very important in cases, where strong deviations from proportional loading occurs, e.g. in the case of shell structural instability in the inelastic range.

The main task of the present work consists of the development and the numerical implementation of a special-purpose constitutive model, suitable for large-scale structural stability computations within a finite element framework. The model employs von Mises yield surface (J_2 - plasticity) and the rate form of J_2 - deformation theory, it accounts for large strains, and leads to a non-associated flow rule. Special emphasis is paid on the continuity of plastic flow, to overcome numerical problems of convergence. The numerical implementation is conducted through both the backward-Euler and a forward-Euler substitution scheme, where stress and strain tensors are described in curvilinear coordinates,

accounting for the extra constraint of zero normal stress through the shell thickness.

The model is incorporated in a special-purpose nonlinear cylindrical shell finite element methodology, where the shell is described through a Lagrangian approach with convected coordinates and discretization is considered through a three-node "tube element". The above technique is suitable for identifying bifurcation, investigating imperfection sensitivity and determining post-bifurcation behavior of the steel cylinder under compressive loads (uniform compression or bending).

The numerical results are compared with available experimental data and analytical predictions and is demonstrated that the present methodology is capable of describing accurately and efficiently buckling and post-buckling behavior of rather thick-walled cylindrical shells in the inelastic range. Furthermore, wrinkling and post-wrinkling behavior of thick-walled high-strength seamless tubular (circular hollow section) members are presented in terms of both the ultimate load and the deformation capacity of typical cross-sections, in order to determine their ability to sustain load well above the first yield level. The results are aimed at evaluating the applicability of EN 1993-1-1 provisions for cross-sectional classification in the case of high-strength steel CHS seamless tubular members an issue of major importance for the design of tubular structures. The numerical results are compared with available experimental data, performed elsewhere.

The contributions of the present work can be summarized as follows:

- A J_2 - non-associative plasticity model is developed, capable of describing the effects of yield surface vertex on the structural response and buckling of shells in an efficient manner.
- Robust integration schemes are presented, accounting for zero stress normal to shell surface and the "consistent moduli" are reported.
- A large-strain J_2 - non-associative plasticity model is also developed for efficient large-strain nonlinear analysis of cylindrical shells, and is integrated using the polar decomposition of deformation gradient and appropriate rotation of stress and rate of deformation tensors.
- The constitutive model is implemented in a user material subroutine and incorporated in an in-house finite element technique for shell buckling analysis.
- The present numerical results are compared successfully with available experimental data and analytical predictions.
- The comparison with test data demonstrates the superiority of this non-associative model with respect to the classical associative J_2 - plasticity model in predicting shell buckling in the inelastic range.

- Buckling calculations on thick-walled seamless tubulars made of high-strength subjected to axial compression and bending are performed, in terms of both the ultimate load and the deformation capacity, and their ability to sustain load well beyond the elastic range is determined.
- Based on the numerical results, considering imperfections and residual stresses obtained from real measurements on high-strength steel seamless tubes, those tubes exhibit significantly higher ultimate load and deformation capacity with respect to the predictions of existing design rules, indicating the conservativeness of current design practice for the case of high-strength steel tubulars.

ΑΡΙΘΜΗΤΙΚΗ ΕΠΙΛΥΣΗ ΛΥΓΙΣΜΟΥ ΚΑΙ ΜΕΤΑΛΥΓΙΣΜΙΚΗΣ ΣΥΜΠΕΡΙΦΟΡΑΣ ΣΕ ΑΝΕΛΑΣΤΙΚΑ ΚΕΛΥΦΗ

Πατρικία Παππά

Πανεπιστήμιο Θεσσαλίας
Τμήμα Μηχανολόγων Μηχανικών
2016

Επιβλέπων: Δρ. Σπύρος Α. Καραμάνος, Καθηγητής

Περίληψη

Αντικείμενο της διδακτορικής διατριβής είναι η προσομοίωση της συμπεριφοράς μεταλλικών κελυφών σε λυγισμό, με στόχο να χαράσσεται με ακρίβεια ο δρόμος ισορροπίας της μεταλυγισμικής συμπεριφοράς και να περιγράφεται η ευαισθησία σε αρχικές ατέλειες μέσω της ανάπτυξης ενός ειδικού μοντέλου μη-συνηρτημένης πλαστικότητας. Ο κύριος στόχος της εργασίας είναι η ανάπτυξη ενός μη-συνηρτημένου μοντέλου πλαστικότητας (*J2* - non-associative plasticity model), το οποίο λαμβάνει υπόψη την δημιουργία μιας εικονικής γωνίας ("corner-like" effects) στην επιφάνεια διαρροής στο σημείο της φόρτισης και είναι κατάλληλο για την εξέταση του λυγισμού και τη μεταλυγισμική συμπεριφορά των κελυφών.

Η αριθμητική επίλυση λυγισμού και μεταλυγισμικής συμπεριφοράς ανελαστικών κελυφών αποτελεί το βασικό πρόβλημα της Διατριβής. Στα πλαίσια, επομένως αυτής της μελέτης διεξήχθη μια εκτενής βιβλιογραφική ανασκόπηση των εξεταζόμενων προβλημάτων όπου γίνεται αξιολόγηση των διαθέσιμων πειραματικών δεδομένων και αναλυτικών λύσεων. Θα πρέπει να σημειωθεί ότι οι αναλύσεις πεπερασμένων στοιχείων που χρησιμοποιούν συνηρτημένο μοντέλο

πλαστικότητας (J_2 - associative plasticity model) παρουσιάζουν μία σημαντική απόκλιση από τα πειράματα (δείχνουν γενικώς μεγαλύτερη αντοχή από την πειραματική), λόγω κυρίως της αδυναμίας των συνήθων καταστατικών εξισώσεων ελαστοπλαστικής συμπεριφοράς να περιγράψουν την εντατική κατάσταση στο μεταλλικό υλικό την στιγμή του λυγισμού. Αντιθέτως, τα αντίστοιχα μοντέλα που εμπίπτουν στην κατηγορία των μη-συνηρτημένων μοντέλων πλαστικότητας (non-associative plasticity models), τα οποία περιγράφουν προσεγγιστικά την δημιουργία ενός κώνου στην επιφάνεια διαρροής, στο σημείο της φόρτισης, περιγράφουν με καλύτερη ακρίβεια την απότομη αλλαγή στο πεδίο των τάσεων την στιγμή του λυγισμού. Τα μοντέλα όμως που προκύπτουν είναι αρκετά περίπλοκα και δεν έχουν δοκιμαστεί σε μεγάλης κλίμακας υπολογισμούς πεπερασμένων στοιχείων.

Στόχος της εργασίας είναι να αναπτυχθεί ένα νέο μοντέλο το οποίο να ενσωματώνει τα πλεονεκτήματα των μοντέλων που έχουν προταθεί ως τώρα και να είναι εύχρηστο για αριθμητικούς υπολογισμούς πεπερασμένων στοιχείων μεγάλης κλίμακας, καθώς και να επαληθεύει τα πειραματικά αποτελέσματα που αναφέρονται στην βιβλιογραφία.

Για την δημιουργία του νέου μη-συνηρτημένου μοντέλου πλαστικότητας χρησιμοποιήθηκε η αυξητική μορφή του μοντέλου πλαστικότητας συνολικών τάσεων παραμορφώσεων (J_2 – deformation plasticity model). Ο ρυθμός αύξησης της πλαστικής παραμόρφωσης αποτελείται από δύο συνιστώσες, μία κάθετη και μία εφαπτομενική στην επιφάνεια διαρροής, σε αντίθεση με τα συνηρτημένα μοντέλα που έχουν μία συνιστώσα κάθετη στην επιφάνεια διαρροής. Αυτό έχει σαν αποτέλεσμα, οι ελαστοπλαστικές σταθερές που προκύπτουν να είναι λιγότερο «δύσκαπτες», και να περιγράφουν με ακρίβεια την απότομη αλλαγή στο πεδίο των τάσεων την στιγμή του λυγισμού. Ιδιαίτερη έμφαση έχει δοθεί στην συνέχεια του ρυθμού αύξησης της πλαστικής παραμόρφωσης. Μια τροποποίηση του ρυθμού αύξησης της πλαστικής παραμόρφωσης έχει προταθεί, ώστε να ξεπεραστούν προβλήματα αριθμητικής σύγκλισης. Το νέο μοντέλο πλαστικότητας διατηρεί τα

βασικά χαρακτηριστικά της κλασσικής θεωρίας, αλλά επεκτείνει την βασική θεωρία ώστε να μπορεί να προσομοιώνει με ακρίβεια το λυγισμό των κελυφών, χωρίς επιπλέον παραμέτρους που απαιτούν τα μοντέλα corner/pseudo-corner theory of plasticity. Το μοντέλο θεωρεί μηδενική τάση κάθετη στην επιφάνεια του κελύφους, και ολοκληρώνεται με μία εύρωστη μέθοδο backward-Euler καθώς επίσης και με την μέθοδο forward-Euler. Το μοντέλο επεκτείνεται και για μεγάλες παραμορφώσεις, όπου ολοκληρώνεται μέσω μιας εύρωστης μεθοδολογίας που βασίζεται στην πολική ανάλυση του τανυστή κλίσης της παραμόρφωσης.

Για την προσομοίωση της ελαστοπλαστικής συμπεριφοράς του κελύφους και των αρχικών ατελειών, έχει χρησιμοποιηθεί ένας πηγαίος κώδικας πεπερασμένων στοιχείων που αναπτύχθηκε από την ερευνητική ομάδα του Πανεπιστημίου Θεσσαλίας και έχει δώσει εξαιρετικά αποτελέσματα για κυλινδρικά κελύφη. Το καταστατικό μοντέλο ελαστοπλαστικής συμπεριφοράς έχει ενσωματωθεί στο πρόγραμμα πεπερασμένων στοιχείων, όπου χρησιμοποιείται μία μεθοδολογία μη γραμμικής ανάλυσης κατασκευών, η οποία βασίζεται σε μία Λαγκρανζιανή περιγραφή του παραμορφώσιμου στερεού με «ενσωματωμένες» συντεταγμένες. Ο κώδικας έχει την δυνατότητα ελαστοπλαστικής ανάλυσης με μεγάλες παραμορφώσεις/μετατοπίσεις και μεταλυγισμικής ανάλυσης του κελύφους και χρησιμοποιεί ένα εξειδικευμένο τρικομβικό “στοιχείο σωλήνα” (“tube element”)για την ανάλυση των κυλινδρικών κελυφών το οποίο συνδυάζει την διαμήκη παραμόρφωση τύπου δοκού με την παραμόρφωση της διατομής του σωλήνα. Ο πηγαίος κώδικας έχει την δυνατότητα να λαμβάνει υπόψη οιαδήποτε μορφή αρχικής ατέλειας και οιαδήποτε κατανομή παραμενουσών τάσεων, επιτρέποντας την συστηματική παραμετρική διερεύνηση της οριακής αντοχής των αγωγών.

Στα πλαίσια της παρούσας έρευνας μελετήθηκε ο ελαστοπλαστικός λυγισμός κυλινδρικών κελυφών, με λόγο διαμέτρου-προς-πάχος D/t_s μεταξύ 20 και 60, σε συνθήκες αξονικής και καμπτικής φόρτισης, συμπεριλαμβανομένης της μεταλυγισμικής συμπεριφοράς. Παράλληλα με την αριθμητική προσομοίωση έχουν διεξαχθεί συγκρίσεις με αναλυτικά και πειραματικά αποτελέσματα όπου

αυτό ήταν εφικτό, που αποσκοπούν στην επαλήθευση των αριθμητικών αποτελεσμάτων, την βαθμονόμηση του υπολογιστικού μοντέλου και την εξακρίβωση της ακρίβειάς και αποτελεσματικότητας του. Τα αποτελέσματα είναι σε συμφωνία με αναλυτικές λύσεις και πειραματικά δεδομένα, τόσο στο κρίσιμο φορτίο όσο και στην μεταλυγισμική συμπεριφορά και την ευαισθησία σε αρχικές ατέλειες.

Στο τελευταίο μέρος της διατριβής παρουσιάζεται μια σημαντική πρακτική εφαρμογή της ανωτέρω μεθοδολογίας, που αφορά τον λυγισμό σωλήνων από χάλυβα υψηλής αντοχής. Η εφαρμογή αυτή είναι σημαντική για τον δομικό σχεδιασμό σωληνωτών κατασκευών, ιδιαίτερα για την αξιολόγηση των ισχυόντων σχεδιαστικών διατάξεων του αντίστοιχου Ευρωπαϊκού κανονισμού.

Η πρωτοτυπία της διδακτορικής διατριβής συνοψίζεται στα ακόλουθα σημεία:

- Στην ανάπτυξη του μη-συνηρτημμένου μοντέλου πλαστικότητας για μικρές και μεγάλες παραμορφώσεις, το οποίο προσομοιώνει εμμέσως την δημιουργία ακμής πάνω στην επιφάνεια διαρροής, και την επιρροή της ακμής στην δομική συμπεριφορά και ευστάθεια μεταλλικών κελυφών.
- Στην εύρωστη ολοκλήρωση του ανωτέρω μοντέλου, συμβατής με την απαίτηση μηδενικής τάσης κάθετα προς την επιφάνεια του κελύφους για μικρές και μεγάλες παραμορφώσεις.
- Στην αριθμητική εφαρμογή του μοντέλου με κατάλληλη υπορουτίνα και στην ενσωμάτωσή της σε ένα περιβάλλον πεπερασμένων στοιχείων για τη μη-γραμμική ανάλυση κυλινδρικών κελυφών.
- Στην πιστοποίηση της υπεροχής του προτεινόμενου μη-συνηρτημμένου μοντέλου, σε σχέση με το κλασσικό μοντέλο, με βάση συγκρίσεις των αποτελεσμάτων με αναλυτικές λύσεις και πειραματικά αποτελέσματα.
- Στην εφαρμογή της ανωτέρω μεθοδολογίας για τον υπολογισμό της αντοχής και κατηγοριοποίησης της διατομής μεταλλικών σωλήνων από χάλυβα υψηλής αντοχής.

Table of Contents

Table of Figures

Table of Tables

Acronyms/Notations

Al	Aluminum
ATTEL	is an acronym for the European project: "Performance-Based Approaches for High Strength Tubular Columns and Connections under Earthquakes and Fire Loadings"
CHS	Circular Hollow Section
DMV	Donnell – Mushtari – Vlasov (shell theory)
HP	High Pressure
HT	High Temperature
VHS	Very High Strength
A_i (i=1,2,3)	Principal invariants of $\mathbf{U}$
B_i (i=1,2,3)	Principal invariants of $\mathbf{U}^{-1}$,
$\mathbf{C}$	Right Cauchy-Green strain tensor
D	Diameter of the tube
$\mathbf{D}$	Elastic rigidity (fourth order elastic stiffness tensor)
$\mathbf{D}_{ep}$	Instantaneous elastoplastic rigidity tensor (tangent moduli)
$\mathbf{D}_{ep}^{c}$	The consistent (algorithmic) elastoplastic rigidity tensor
$\mathbf{d}$	Rate-of-deformation tensor
$\mathbf{d}^{e}$	Elastic part of rate-of-deformation tensor $\mathbf{d}$
$\mathbf{d}^{p}$	Plastic part of rate-of-deformation tensor $\mathbf{d}$

E	Young's modulus
E_s	Secant modulus
E_T	Tangent modulus
$\dot{\mathbf{E}}$	Rate-of- logarithmic strain tensor
$\dot{\mathbf{E}}^e$	Elastic part of $\dot{\mathbf{E}}$
$\dot{\mathbf{E}}^p$	Plastic part of $\dot{\mathbf{E}}$
$\mathbf{e}$	Deviatoric part of total strain tensor $\boldsymbol{\varepsilon}$
$\mathbf{F}$	Deformation gradient tensor
G	Shear modulus of elasticity
G_s	$G_s = \dfrac{1}{\dfrac{1}{G}+\dfrac{3}{h}}$
G_T	$G_T = \dfrac{1}{\dfrac{1}{G}+\dfrac{3}{H}}$
$\mathbf{G}^i$	Contravariant base vector at the beginning of the step
$\mathbf{g}_i$	Covariant base vector in the current configuration (curvilinear system)
$\mathbf{g}^j$	Contravariant base vector in the current configuration (curvilinear system)
H	Hardening modulus
h_1	$h_1 = \dfrac{1}{E_T}-\dfrac{1}{E_s}$
i_1, i_2, i_3	Principal invariants of a tensor

$\mathbf{I}$	Symmetric fourth-order identity tensor $I_{ijkl} = \frac{1}{2}\left(\delta_{ik}\delta_{jl} + \delta_{il}\delta_{jk}\right)$
$\mathbf{J}$	Volumetric fourth-order identity tensor $J_{ijkl} = \frac{1}{3}\delta_{ij}\delta_{kl}$
K	Bulk modulus
k	Material yield stress in uniaxial tension
L	Length of the tube
$\mathcal{L}$	Geometric rigidity fourth-order tensor
$\mathbf{N}$	Dimensionless tensor, defined at a certain stress state $\boldsymbol{\sigma}$, $\mathbf{N} = \frac{3}{2q}\mathbf{s}$
$\mathbf{n}$	Unit outward normal tensor to the yield surface
$\mathbf{P}$	Fourth-order tensor $\mathbf{P} = \mathbf{I} - \mathbf{J}$
p	Hydrostatic parts of the stress
$\mathbf{R}$	Rotation tensor
$\mathcal{R}$	Fourth order tensor,
q	von Mises equivalent stress
$\dot{q}$	Rate of von Mises equivalent stress q
$\mathbf{s}$	Deviatoric stress tensor
$\dot{\mathbf{s}}$	Rate of deviatoric stress tensor
$\|\mathbf{s}\|$	Magnitude of $\mathbf{s}$
$\dot{\mathbf{s}}^t$	Component of $\dot{\mathbf{s}}$ tangent to the yield surface
$\dot{\mathbf{s}}^n$	Component of $\dot{\mathbf{s}}$ normal to the yield surface

$\overset{\nabla}{\mathbf{s}}$	Jaumann rate of deviatoric part of the Kirchhoff stress
t	Time
t_s	Thickness of the tube
$\boldsymbol{\tau}$	Kirchhoff stress
$\dot{\boldsymbol{\tau}}$	Rate of Kirchhoff stress $\boldsymbol{\tau}$
$\overset{\nabla}{\boldsymbol{\tau}}$	Jaumann rate of Kirchhoff stress $\boldsymbol{\tau}$
$\overset{\circ}{\boldsymbol{\tau}}$	Convected rate of Kirchhoff stress tensor
$\hat{\boldsymbol{\tau}}$	Rotational stress tensor
$\mathbf{U}$	Stretch tensor
u_{ij}	Components of $\mathbf{U}$ with respect to the $\left(\mathbf{G}^i \otimes \mathbf{G}^j\right)$ basis
$\overline{u}_{ij}$	Components of $\mathbf{U}^{-1}$ with respect to the $\left(\mathbf{G}^i \otimes \mathbf{G}^j\right)$ basis
$\mathbf{W}$	Spin tensor
$\Delta\mathbf{E}$	Logarithmic strain
$\Delta\boldsymbol{\varepsilon}$	Total strain increment
$\Delta\boldsymbol{\varepsilon}^p$	Plastic strain increment
$\Delta\overline{\boldsymbol{\varepsilon}}$	Known part of the total strain increment $\Delta\boldsymbol{\varepsilon}$
$\Delta\varepsilon_{33}$	Unknown part of the total strain increment $\Delta\boldsymbol{\varepsilon}$
$\boldsymbol{\varepsilon}$	Total strain
$\boldsymbol{\varepsilon}^e$	Elastic strain
$\boldsymbol{\varepsilon}^p$	Plastic strain
$\dot{\boldsymbol{\varepsilon}}$	Rate of total strain $\boldsymbol{\varepsilon}$

$\dot{\boldsymbol{\varepsilon}}^e$	Elastic strain rate
$\dot{\boldsymbol{\varepsilon}}^p$	Plastic strain rate
ε_q	Equivalent plastic strain
$\lambda_1, \lambda_2, \lambda_3$	Principal stretches
ξ^1, ξ^2, ξ^3	Curvilinear system (where coordinate line ξ^1 is directed in the hoop direction of the cylinder, ξ^2 in the axial direction of the cylinder and ξ^3 is initially directed through the shell thickness)
$\dot{\boldsymbol{\sigma}}$	Rate of stress $\boldsymbol{\sigma}$
$\boldsymbol{\sigma}^e$	Purely elastic (trial) stress
$\mathbf{1}$	Second-order unit tensor

Chapter 1

Introduction

Relatively thick cylindrical metal shells, with diameter-to-thickness ratio D/t_s less than 50, are widely used in pipeline and piping applications for hydrocarbon transportation and distribution. Those elongated metal cylinders, often referred to as "tubes" or "pipes", can be subjected to severe structural loading, which induces significant compressive strains in the cylinder wall. As an example, high-pressure/high-temperature (HP/HT) buried steel pipelines, restrained by the surrounding ground, may experience severe axial compression (Yun and Kyriakides, 1990). In offshore pipeline operations, significant bending may occur in a pipeline during the installation process at the stinger (Corona and Kyriakides, 1988; Karamanos and Tassoulas, 1991). Furthermore, the differential motion of the surrounding soil in a buried steel pipeline caused by fault movement, landslides, ground subsidence, permafrost melting, or soil liquefaction, can also result in severe compression of the line (Vazouras *et al.* 2010, 2012, 2015).

Excessive compressive action on the pipe wall may result in buckling failure in the form of wrinkles, sometimes referred to as "local buckling". This is a

shell-type buckling, and is quite different from the one that thin-walled shells exhibit. More specifically, thin-walled cylindrical shells under axial compression buckle in the elastic range, and their behavior is characterized by sudden collapse and imperfection sensitivity. Figure 1 - 1(a) shows the buckled shape of thin-walled cylindrical vessel ($D/t_s \leq 609$) subjected to axial compression (Karcher *et al.* 2009), whereas Figure 1 - 1(b) and Figure 1 - 1(c) show the buckled shape of two relatively thin-walled cylinders ($D/t_s \simeq 100$) subjected to bending (Van Foeken and Gresnigt, 1994). In both cases, failure of the cylinders occurs suddenly and is catastrophic. On the contrary, thick-walled cylinders buckle in the plastic range and failure occurs more gradually, after a sequence of events.

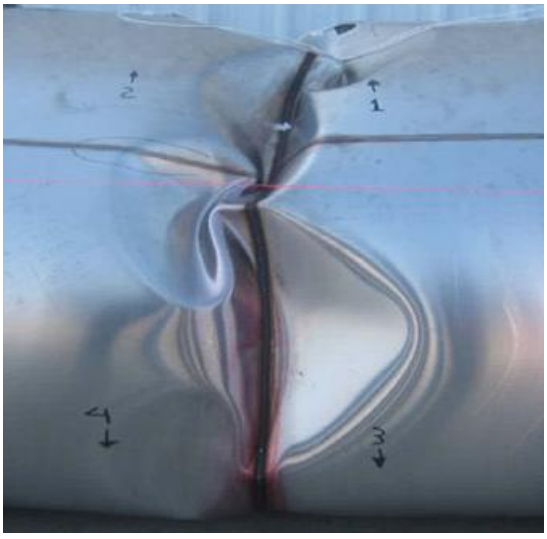

(a)

(b)

(c)

Figure 1 - 1: Thin-walled cylindrical shell buckling; (a) axial compression of a thin-walled tank (D/t=609); (b) and (c) buckling of thin-walled cylinders under bending.

1.1 Experimental and numerical work on buckling of thick-wall cylindrical shells

Early experimental work has been reported on relatively-thick aluminum cylinders by Lee (1962) and Batterman (1965), supported by analytical bifurcation calculations based on nonlinear elastic-plastic shell analysis. Lee (1962) tested ten tubes made of Al-3003-0 with yield stress equal to 6 *ksi* (41.4 *MPa*) and significant hardening. The tubes had diameter-to-thickness ratios $\left(D/t_s\right)$ of 20, 40, 59.7 and 93 and length-to-diameter ratios $\left(L/D\right)$ between about 2 and 5. The cylinders were clamped at the ends and, as a result, edge bulges developed, dominating the response, and no ‘‘bifurcation’’ stress or wrinkle wavelength was reported although axial waves were observed in the test section. Batterman (1965) tested 16 shell specimens from Al-2024-T4, with yield stress equal to 56.5 *ksi* (390 *MPa*) and D/t_s values between about 20 and 180. The shells had length-to-diameter L/D ratios between 1.5 and 0.18. The specimens were compressed between lubricated rigid platens to alleviate end (boundary) effects and axisymmetric modes of failure have been reported for tubes with the lower D/t_s values. In both series of experiments, the buckling resistance was reported in terms of the maximum (limit) stress and it was indicated that the buckling resistance of relatively-thick metal cylindrical shells is less sensitive to initial imperfections than of thin-walled elastic shells. Nevertheless, the relatively short length of most of the specimens does not allow

for a direct comparison with bifurcation analysis predictions.

Bending tests of cylindrical shells were reported by Bouwkamp and Stephen (1974). Eight tests were carried out on seven specimens. Test specimens were longitudinal-seam tubes manufactured from X60 steel with a yield stress of 60 *ksi* (414 *MPa*), with the exception of one specimen. The nominal diameter of the pipes was 48 *in.* (1,200 *mm*) and the nominal thickness was 0.462 *in.* (11.7 *mm*). Bending was accompanied by the application of axial loads and internal pressure.

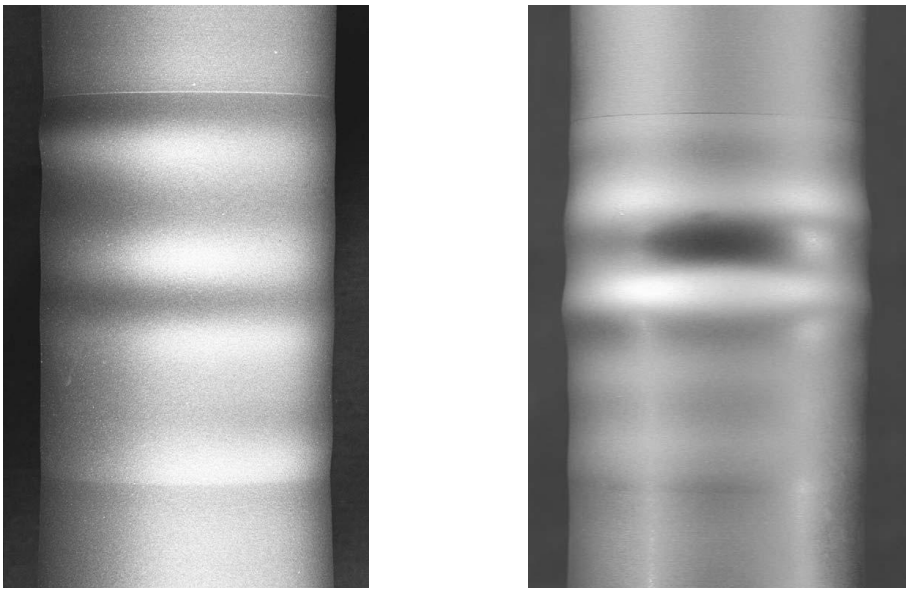

(a) (b)

Figure 1 - 2: Thick-walled cylindrical shell buckling under axial compression (D/t=26.5); (a) first wrinkling; (b) localization of buckled shape.

Tests on small-scale aluminum-alloy and stainless steel cylinders with D/t_s ratios ranging from approximately 30 to 80 were reported by Reddy (1979), motivated by the need to provide design guidelines for submarine pipeline installation. Ten steel and nine aluminum specimens were tested. The nominal diameter of the specimens was 1 *in.* (25.4 *mm*). The tests were carried out under pure bending conditions in the absence of sheer through a four-point loading set-up, and the results were reported in terms of extreme fiber compressive strain. It was also reported that wrinkles steadily grew from initial imperfections into sine-wave patterns on the compressive side of the specimens before collapse took place.

The imperfection sensitivity of axially compressed cylindrical shells has been investigated analytically by Gellin (1979), extending Koiter's methodology for cylindrical shells in the inelastic range considering a uniform axisymmetric initial imperfection (Koiter, 1963). Using nonlinear shell kinematics, deformation theory of plasticity, and axisymmetric imperfections, Gellin calculated the stage where a secondary bifurcation occurs, assuming that this is representative of buckling strength of the compressed cylinder.

A thorough investigation of pure bending buckling of inelastic tubes and the various instabilities that can be encountered was reported by Kyriakides and Ju (1992) in a series of experiments on Al-6061-T6 tubes with diameter-to-thickness values $\left(D/t_s\right)$ in the range of approximately 20–60. It was shown that

D/t_s governs which of the possible instabilities becomes dominant. For the particular aluminum alloy used, axial wrinkling was found to develop when the D/t_s exceeded a value of about 25. In a companion paper, Ju and Kyriakides (1992) developed a sequence of modeling features for calculating the inelastic response of tubes under bending, in terms of the onset of tube wall wrinkling and its evolution until failure. The basic formulation is an extension of the ovalization model presented in Shaw and Kyriakides (1985) and Corona and Kyriakides (1988), and the possibility of buckling into a wrinkling mode was checked by a bifurcation analysis that is based on the instantaneous moduli of the deformation theory of plasticity. Secondary bifurcation, localization of buckled patterns and imperfection sensitivity were also examined. The numerical results in terms of wrinkling curvatures were in good agreement with the corresponding experimental values.

Zimmerman, *et al.*, (1995) performed five tests with and without internal pressure on Grade 483 steel pipeline specimens with D/t_s ratios of 87 and 41, and a total length of 32.8 *ft* (10 *m*). The pipe material was steel. The primary aim of this work was to provide experimental data for calibration of finite element models. The specimens were loaded in uniform bending moment until failure and subsequently, the tests were simulated using finite element models; good comparison was reported between tests and simulations in terms of the moment-curvature response.

A more recent combined experimental and analytical investigation of buckling behavior of thick cylindrical shells under pure axial compression has been reported by Bardi and Kyriakides (2006) and Bardi *et al.* (2006), which followed a methodology similar to the works of Kyriakides and Ju (1992), and Ju and Kyriakides (1992) for bent cylinders, described above.

In the paper of Tutuncu and O'Rourke (2006), the compression response of 300 *mm* internal diameter steel cylinders with D/t_s of 48 and yield stress equal to 334 *MPa* is assessed by both experimental and analytical procedures. The investigation referred to test specimens with small-scale global geometric imperfections, typical of irregularities that occur during fabrication and handling, and the large-scale local geometric imperfection generated by locally indenting a test specimen to a depth exceeding 180% of its thickness. Analytical procedures were also developed to represent these imperfections and their effects on the compressive response and ultimate load strength.

Finally, eight very-high-strength (VHS) steel stub columns were tested under axial compression by Jiao and Zhao (2003) with D/t_s ratios between 24 and 46, aiming to determine the yield slenderness limit, considering geometrical imperfections and residual stresses. Two non-heat-treated tubes were also tested to show the effect of manufacturing process on geometrical imperfections and residual stresses.

1.2 Material modeling in shell buckling simulations

In simulating metal shell buckling in the inelastic range, the choice of appropriate material models constitutes a key issue. It has been recognized that J_2 - flow theory can accurately describe the general material behavior of metals in the inelastic range and it is widely used for the nonlinear elastic-plastic finite element stress analysis of shell structures (Dvorkin *et al.*, 1995, Argyris *et al.*, 2002, Paraskevopoulos and Talaslidis, 2006). Nevertheless, buckling predictions based on the J_2 - flow theory may not be reliable in cases where bifurcation from the prebuckling state occurs well into the inelastic range. This is attributed to the vertex (corner) that develops on the yield surface at the point of loading. The formation of such vertex on the yield surface at the loading point has been detected experimentally in aluminum and steel materials (Kuroda and Tvergaard, 2001), as shown in (Figure 1 - 3) and can be very important in cases, where abrupt deviations from proportional loading occur, such as in the case of shear band formation and localization of plastic flow, as well as in the case of structural instability of shells in the inelastic range, where the shell wall exhibits a transition from a smooth pre-buckling configuration to a wavy-pattern associated with multi-axial state of stress.

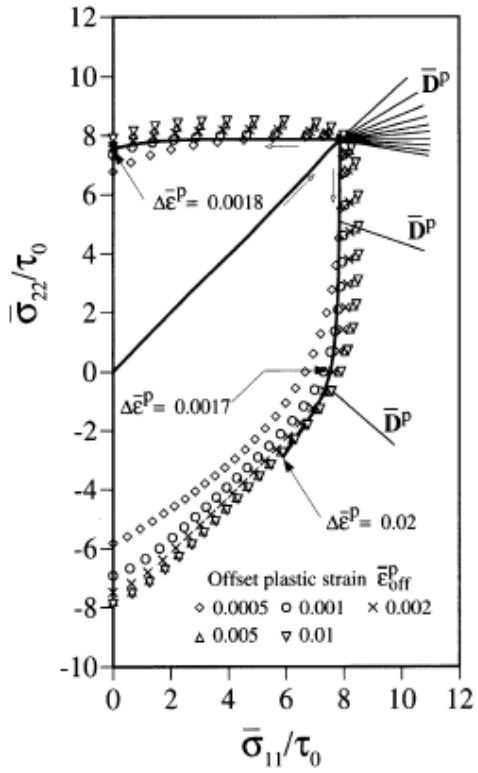

Figure 1 - 3: A typical example of the use of an abrupt path change for determining the subsequent yield surface (Kuroda and Tvergaard, 2001).

To obtain more reliable buckling predictions, in axially-compressed cylindrical metal shells, Tvergaard (1983) and Mikkelsen (1995) conducted stability calculations through a special enhancement of J_2 (von Mises) plasticity theory, referred to as the J_2 - corner theory, initially proposed by Christoffersen and Hutchinson (1979). This theory provides a phenomenological framework for the observations regarding the development of a corner (vertex) on the yield surface at the loading point. Using J_2 - corner theory, the corresponding instantaneous moduli are less stiff than those predicted by the J_2 - flow theory.

Therefore, the response is significantly different for the case of abrupt change of direction in the stress space (e.g. when buckling occurs), while for proportional loading the two theories coincide. Nevertheless, the corner theory, despite its good results for the prediction of shear band formation (Needleman and Tvergaard, 1984) and its rigorousness in describing the corner of the yield surface, may not be suitable for large-scale structural computations that involve complex stress paths and loading/unloading response; a finite element procedure that uses corner theory would require monitoring of all the previously formed corners and their current evolution, and this may not be computationally efficient. Furthermore, calibration of this theory from simple mechanical testing of material coupons is also an open issue.

As an alternative to the above corner theory, several "pseudo-corner" theories have been proposed. Hughes and Shakib (1986) presented a modified J_2 - flow theory with a hardening modulus that depends on the angle between the deviatoric strain increment and the outward vector normal to the yield surface. In this simplistic manner, the model attempts to account for some essential characteristic of the corner theory, such as reduced material stiffness and increased plastic flow, while keeping the basic features of the classical J_2 - flow theory. Nevertheless, this model is rather simplified and may not be a reliable alternative to corner theory for shell buckling calculations in the plastic range.

In a subsequent paper, Simo (1987) proposed a J_2 - non-associative flow

"pseudo-corner" model, which imitates some corner theory characteristics through the adoption of a non-associative flow rule without introducing the complexity associated with keeping track of the formation and evolution of yield surface corners. Simo also presented an efficient backward-Euler scheme for the numerical integration of the pseudo-corner model within a non-linear finite element framework. However, Simo's pseudo-corner model requires the definition of several parameters related to the yield surface "vertex". In addition it is not clear how the proposed integration scheme can be implemented in shell analysis problems. This model has not been used in large-scale inelastic shell buckling calculations.

So far, most of the attempts to predict bifurcation buckling in the inelastic range use the flow theory for tracing the prebuckling solution and employ the deformation theory moduli to detect bifurcation on the prebuckling path (e.g. Ju and Kyriakides, 1992; Bardi *et al.* 2006). However, such an approach does not describe accurately the entire structural response, and most importantly, the correct postbuckling performance. In a more recent publication, Peek (2000) developed a J_2 - plasticity model, which uses a non-associated flow rule similar to the rate form of the J_2 - deformation theory referred to as "incrementally continuous" deformation theory with unloading and the proposed constitutive model can be implemented with minimal changes to an algorithm based on associative flow theory. This model constitutes an important contribution

towards elastic-plastic buckling analysis. However the main drawback of this model is that unloading is no longer elastic, but it contains an amount of inelastic deformation. Furthermore, its implementation to shell buckling problems, where zero normal stress should be zero through shell thickness has not been described.

The above discussion and presentation of the shortcomings of the above models motivate the development of a new model for accurate and efficient buckling and post-buckling analysis of shell metal structures. In particular, the main objective of the present dissertation is the development and the numerical implementation of an efficient special-purpose constitutive model, suitable for accurate and efficient large-scale metal shell buckling computations within a finite element environment. The material model is based on the von Mises yield surface (J_2 plasticity) with isotropic hardening and employs the rate form of J_2 - deformation theory, leading to a non-associated flow rule. The numerical implementation follows a backward-Euler or a forward-Euler substitution scheme, developed for elastic-plastic shell analysis, accounting for zero normal stress through the shell thickness. The model maintains the basic features of the classical J_2 - flow plasticity implementation, while introducing the key enhancements for accurate and efficient shell buckling predictions. Furthermore an enhanced version of the model is developed, which allows the simple and efficient extension of the model for large strains through an additive

decomposition of the rate-of-deformation tensor.

1.3 Contents and scope of present dissertation

The main purpose of the present research is the development, implementation and application of a special-purpose non-associative plasticity model that can be used for efficient inelastic shell buckling and post-buckling calculations. In addition, in the final part of the dissertation, the non-associative model is employed for investigating the local buckling resistance of thick-walled high-strength steel cylinders, towards their evaluating classification according to existing design provisions.

The proposed constitutive model and its numerical integration are presented in the framework of small-strain plasticity in Chapter 2, whereas Chapter 3 describes the direct enhancement of the constitutive model for large strain analysis. The non-associative constitutive model is incorporated in a special-purpose finite element methodology, outlined in Chapter 4; this finite element methodology has been introduced elsewhere for the analysis of nonlinear cylindrical shells, and has been shown very efficient for analyzing the structural behavior of steel cylinders (Karamanos and Tassoulas 1996). In Chapter 5, the issue of plastic flow continuity is addressed in terms of the plastic production ratio.

Using the above mentioned numerical technique shell buckling problems,

involving nonlinear equilibrium paths; bifurcation and limit points are analyzed, whereas the issues of post-buckling response and imperfection sensitivity are considered as well. In particular, the problem of inelastic elongated cylinders under uniform axial compression and the bending response of inelastic cylinders are examined in Chapter 6. The problems examined in the course of this study may considered as benchmarks for the capabilities of the proposed special-purpose model and its numerical implementation, in terms of its accuracy and computational efficiency. The numerical results are compared with existing analytical results, as well as with available experimental data.

In Chapter 7, wrinkling and post-wrinkling behavior of thick-walled CHS seamless tubular members, made of high-strength steel (with yield stress above 590 MPa, up to 735 MPa), subjected to both axial and bending loading are investigated, in order to determine their ability to sustain axial load or bending moment above the first yield level. Furthermore, the deformation capacity of those structural members in the inelastic range until the occurrence of local buckling is also examined. The results are compared with available test data, and are employed for evaluating the EN 1993 classification provisions. Those provisions have been proposed for tubes made of steel grade equal or less than 460 MPa and the present investigation examines their applicability in the design of high-strength steel tubes.

Finally, in Chapter 8, some important conclusions from this dissertation are summarized.

Chapter 2

Constitutive Model

Materials models are presented for the description of elastic-plastic material behavior assuming small and large deformations. In small strain plasticity the most commonly employed constitutive laws are the "J_2 - flow theory" and "J_2 - deformation theory" relations. Deformation theory was proposed by Hencky (1924), [see also Lubliner (1990), pp. 123, 330], is clearly inadequate for characterizing the most general path-dependent features of plastic behavior; however, if the loading history is "proportional", as in classical bifurcation analyses, is simply the integrated result of the corresponding J_2 - flow theory. The classical associative J_2 - flow theory is presented in Appendix I, followed by its numerical integration and the development of the consistent elastic rigidity matrix. In this chapter, a description of the non-associative J_2 - incremental model for small-strain analysis that employs the rate form of J_2 - deformation theory for plastic loading is presented, followed by its numerical integration and the development of the consistent elastic rigidity matrix.

The purpose of the work described in this chapter, is the development of an enhanced J_2 - incremental theory of plasticity, capable of describing buckling and post-buckling response in the plastic range.

2.1 Model description

The equations describing the behavior of an elastic-plastic isotropic material are well known and have been presented in many sources. In the framework of incremental plasticity, the rate of stress $\dot{\boldsymbol{\sigma}}$ is related to the elastic strain rate $\dot{\boldsymbol{\varepsilon}}^e$ as follows:

$$\dot{\boldsymbol{\sigma}} = \mathbf{D}\dot{\boldsymbol{\varepsilon}}^e = \mathbf{D}\left(\dot{\boldsymbol{\varepsilon}} - \dot{\boldsymbol{\varepsilon}}^p\right) \tag{2.1}$$

where $\mathbf{D}$ is the fourth order elastic stiffness tensor, $\dot{\boldsymbol{\varepsilon}}$ is the rate of total strain and $\dot{\boldsymbol{\varepsilon}}^p$ is the plastic strain rate. The elastic rigidity $\mathbf{D}$ can be expressed as follows:

$$\mathbf{D} = 2G\,\mathbf{I} + 3\left(K - \frac{2}{3}G\right)\mathbf{J} \tag{2.2}$$

where K is the bulk modulus, G is the shear modulus, $\mathbf{I}$ is the symmetric fourth-order identity tensor and $\mathbf{J}$ is the volumetric fourth-order identity tensor. Tensor $\mathbf{D}$ can also be written in the following form:

$$\mathbf{D} = 2G\,\mathbf{P} + 3K\,\mathbf{J} \tag{2.3}$$

where the fourth-order tensor $\mathbf{P}$ is defined as

$$\mathbf{P} = \mathbf{I} - \mathbf{J} \tag{2.4}$$

In the present model, the flow rule adopts the rate form of the J_2 - deformation theory:

$$\dot{\boldsymbol{\varepsilon}}^p = \frac{3}{2}\left(\frac{1}{E_s} - \frac{1}{E}\right)\dot{\mathbf{s}} + \frac{3}{2}\frac{\dot{q}}{q}\left(\frac{1}{E_T} - \frac{1}{E_s}\right)\mathbf{s} \tag{2.5}$$

where $\mathbf{s}$ is the deviatoric stress tensor, q is the von Mises equivalent stress,

defined as follows

$$q = \sqrt{\frac{3}{2}\mathbf{s}\cdot\mathbf{s}} = \sqrt{3J_2} \tag{2.6}$$

so that

$$\dot{q} = \frac{3}{2q}\mathbf{s}\cdot\dot{\mathbf{s}} \tag{2.7}$$

and E, E_s, E_T are the Young's modulus, the secant modulus and the tangent modulus respectively. Yielding is defined by the von Mises yield function with isotropic hardening

$$F\left(\boldsymbol{\sigma},\varepsilon_q\right) = \frac{1}{2}\mathbf{s}\cdot\mathbf{s} - \frac{1}{3}k^2\left(\varepsilon_q\right) = 0 \tag{2.8}$$

where $k = k\left(\varepsilon_q\right)$ is the material yield stress in uniaxial tension, which defines the size of the yield surface, ε_q is the equivalent plastic strain, defined as follows

$$\dot{\varepsilon}_q = \sqrt{\frac{2}{3}}\,\dot{\boldsymbol{\varepsilon}}^p\cdot\mathbf{n} \tag{2.9}$$

and $\mathbf{n} = \dfrac{\mathbf{s}}{\|\mathbf{s}\|}$ is the unit outward normal tensor to the yield surface and $\|\mathbf{s}\|$ is the magnitude of $\mathbf{s}$ $\left(\|\mathbf{s}\| = \sqrt{\mathbf{s}\cdot\mathbf{s}}\right)$. Function $k\left(\varepsilon_q\right)$ can be nonlinear, and is calibrated from a uniaxial tension test.

The plastic strain rate equation (2.5) can be rewritten in the following, more illustrative vector form

$$\dot{\boldsymbol{\varepsilon}}^p = \frac{3\dot{\varepsilon}_q}{2q}\mathbf{s} + \frac{3}{2}\left(\frac{1}{E_s} - \frac{1}{E}\right)\dot{\mathbf{s}}^t \tag{2.10}$$

where

$$\dot{\mathbf{s}}^t = \dot{\mathbf{s}} - \left(\mathbf{n}\cdot\dot{\mathbf{s}}\right)\mathbf{n} \tag{2.11}$$

The deviatoric stress tensor $\dot{\mathbf{s}}^t$ is the component of $\dot{\mathbf{s}}$ tangent to the yield surface shown in Figure 2 - 1. The flow rule in equation (2.10) implies that the plastic strain increment is composed by two components, one normal to the yield surface and one tangent to the yield surface. This makes the elastic-plastic instantaneous moduli of the J_2 - deformation less stiff than the corresponding moduli of the J_2 - flow theory. More specifically, the instantaneous rigidity tensor (tangent moduli) for this model can be written as follows

$$\mathbf{D}_{ep} = 2G_s\mathbf{I} + 3\left(K - \frac{2}{3}G_s\right)\mathbf{J} - \frac{3}{q^2}\left(G_s - G_T\right)\left(\mathbf{s}\otimes\mathbf{s}\right) \tag{2.12}$$

where

$$G_s = \frac{1}{\frac{1}{G} + \frac{3}{h}} \tag{2.13}$$

$$G_T = \frac{1}{\frac{1}{G} + \frac{3}{H}} \tag{2.14}$$

$$h = \frac{1}{\frac{1}{E_s} - \frac{1}{E}} \tag{2.15}$$

and H is the hardening modulus, equal to $d\,k/d\,\varepsilon_q$, and also is defined as

$$H = \frac{1}{\frac{1}{E_T} - \frac{1}{E}} \tag{2.16}$$

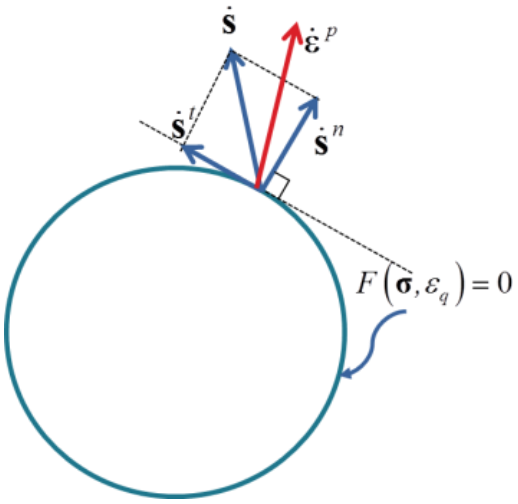

Figure 2 - 1: Schematic representation of stress and strain tensor increments in the deviatoric plane, with respect to von Mises surface.

A curvilinear system ξ^1, ξ^2, ξ^3 is considered to describe stress and deformation within the shell, where coordinate lines ξ^1 and ξ^2 are directed in the hoop and in the axial direction of the cylinder, respectively, and for a constant value of ξ^3, they define a shell surface (lamina), whereas the coordinate line ξ^3 is initially directed through the shell thickness. The covariant and contravariant base vectors of this coordinate system are denoted as $\mathbf{g}_i$ and $\mathbf{g}^j$ respectively, as shown in Figure 2 - 2. Therefore, the stress tensor can be written in terms of the covariant tensor base as

$$\boldsymbol{\sigma} = \sigma^{ij}\left(\mathbf{g}_i \otimes \mathbf{g}_j\right) \tag{2.17}$$

and the components of fourth-order rigidity tensors $\mathbf{D}$ and $\mathbf{D}_{ep}$ with respect to the covariant basis can be written

$$D^{ijkl} = G\left(g^{jl}g^{ik} + g^{il}g^{jk}\right) + \left(K - \frac{2}{3}G\right)g^{ij}g^{kl} \tag{2.18}$$

and

$$D_{ep}^{ijkl} = G_s\left(g^{jl}g^{ik} + g^{il}g^{jk}\right) + \left(K - \frac{2}{3}G_s\right)g^{ij}g^{kl} - \frac{3}{q^2}\left(G_s - G_T\right)s^{ij}\,s^{kl} \tag{2.19}$$

Finally, in the present formulation, following shell theory, it is required that the traction component normal to any shell lamina is imposed to be zero at any stage of deformation. Considering that the traction on the lamina is $\frac{1}{\left\|\mathbf{g}^3\right\|}\boldsymbol{\sigma}\mathbf{g}^3$, where $\left\|\mathbf{g}^3\right\|$ is the magnitude of $\mathbf{g}^3$, i.e. the contravariant base vector normal to the ξ^1, ξ^2-surface (as shown in Figure 2 - 2), and that traction component normal to the lamina is $\frac{1}{\left\|\mathbf{g}^3\right\|^2}\boldsymbol{\sigma}\cdot(\mathbf{g}^3\otimes\mathbf{g}^3)$, which is equal to $\frac{1}{\left\|\mathbf{g}^3\right\|^2}\sigma^{33}$, one obtains the following condition for zero traction component nornal to any shell lamina.

$$\sigma^{33} = 0 \tag{2.20}$$

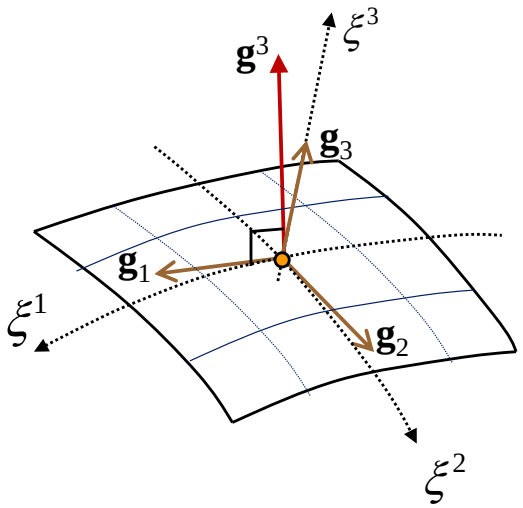

Figure 2 - 2: Curvilinear coordinate system and base vectors for shell description.

2.2 Numerical Integration of the Constitutive Model

The above material model is integrated numerically towards implementation within a nonlinear finite element analysis procedure. The problem can be started as follows. Consider that at a material point, the stress $\boldsymbol{\sigma}_n$, strain $\boldsymbol{\varepsilon}_n$ and the equivalent plastic strain $\varepsilon_{q|n}$ are given at time t_n, as well as the strain $\boldsymbol{\varepsilon}_{n+1} = \boldsymbol{\varepsilon}_n + \Delta\boldsymbol{\varepsilon}$ at time t_{n+1}. The calculation of $\boldsymbol{\sigma}_{n+1}$ and $\varepsilon_{q\,|\,n+1}$ requires integration of the above constitutive equations from t_n to t_{n+1}. An elastic predictor – plastic corrector scheme (Simo &Taylor, 1986) is adopted where a purely elastic trial state is followed by a plastic corrector phase. The purely elastic (trial) stress is defined by the formula

$$\boldsymbol{\sigma}^e = \boldsymbol{\sigma}_n + \mathbf{D}\Delta\boldsymbol{\varepsilon} \tag{2.21}$$

In accordance with condition (2.20), the strain increment is decomposed as follows

$$\Delta\boldsymbol{\varepsilon} = \Delta\overline{\boldsymbol{\varepsilon}} + \Delta\varepsilon_{33}\left(\mathbf{g}^3 \otimes \mathbf{g}^3\right) \tag{2.22}$$

where $\Delta\overline{\boldsymbol{\varepsilon}}$ is the known part of the total strain increment $\Delta\boldsymbol{\varepsilon}$, and $\Delta\varepsilon_{33}$ is an extra unknown (Aravas, 1987).

If the trial stress violates the yield condition, an elastic-plastic behavior should be taken into account, integrating equation (2.1) between stages t_n and t_{n+1},

$$\boldsymbol{\sigma}_{n+1} = \boldsymbol{\sigma}_n + \mathbf{D}\left(\Delta\boldsymbol{\varepsilon} - \Delta\boldsymbol{\varepsilon}^p\right) \tag{2.23}$$

Using an backward-Euler integration scheme for equation (2.5), the

increment of plastic strain is written

$$\Delta\boldsymbol{\varepsilon}^{p}=\frac{3}{2h_{n+1}}\left(\mathbf{s}_{n+1}-\mathbf{s}_{n}\right)+\frac{3}{2}\frac{\Delta\varepsilon_{q}H_{n+1}}{q_{n+1}h_{1|n+1}}\mathbf{s}_{n+1} \tag{2.24}$$

where the von Mises equivalent final stress is

$$q_{n+1}=\sqrt{\frac{3}{2}\mathbf{s}_{n+1}\cdot\mathbf{s}_{n+1}} \tag{2.25}$$

and

$$h_{1}=\frac{1}{E_{T}}-\frac{1}{E_{s}} \tag{2.26}$$

Using equations (2.22) and (2.24), the final stress becomes

$$\boldsymbol{\sigma}_{n+1}=\overline{\boldsymbol{\sigma}}^{e}+2G\Delta\varepsilon_{33}\mathbf{a}-\frac{3G}{h_{n+1}}\left(\mathbf{s}_{n+1}-\mathbf{s}_{n}\right)-\frac{3G\Delta\varepsilon_{q}H_{n+1}}{q_{n+1}h_{1|n+1}}\mathbf{s}_{n+1} \tag{2.27}$$

where

$$\overline{\boldsymbol{\sigma}}^{e}=\boldsymbol{\sigma}_{n}+\mathbf{D}\Delta\overline{\boldsymbol{\varepsilon}} \tag{2.28}$$

$$\mathbf{a}=\mathbf{g}^{3}\otimes\mathbf{g}^{3} \tag{2.29}$$

and $\mathbf{a}'$ is the deviatoric part of $\mathbf{a}$. From equation (2.27), the hydrostatic and the deviatoric parts of the final stress are written as

$$p_{n+1}=\overline{p}^{e}-K\Delta\varepsilon_{33}g^{33} \tag{2.30}$$

$$\mathbf{s}_{n+1}=\frac{1}{1+\dfrac{3G}{h_{n+1}}+\dfrac{3G\Delta\varepsilon_{q}H_{n+1}}{qh_{1|n+1}}}\left(\overline{\mathbf{s}}^{e}+2G\Delta\varepsilon_{33}\mathbf{a}'+\frac{3G}{h_{n+1}}\mathbf{s}_{n}\right) \tag{2.31}$$

where $\overline{p}^{e}\mathbf{1}$, $\overline{\mathbf{s}}^{e}$ are the hydrostatic and deviatoric parts of $\overline{\boldsymbol{\sigma}}^{e}$ ($\overline{\boldsymbol{\sigma}}^{e}=-\overline{p}^{e}\mathbf{1}+\overline{\mathbf{s}}^{e}$). Equation (2.31) shows that $\mathbf{s}_{n+1}$ and $\overline{\mathbf{s}}^{e}$ may not be co-linear and the "plastic

correction" may not be on the deviatoric plane. Squaring equation (2.31), the effective stress at the final state is calculated as follows

$$q_{n+1}=\frac{1}{1+\dfrac{3G}{h_{n+1}}}\left\{\left(\left(\bar{q}^{e}\right)^{2}+\left(\frac{3G}{h_{n+1}}q_{n}\right)^{2}+\frac{6G}{h_{n+1}}Q^{2}+4G^{2}\,\Delta\varepsilon_{33}^{2}\,g^{33}\,g^{33}+\right.\right.$$
$$\left.\left.+6G\,\Delta\varepsilon_{33}\left(\bar{s}^{(e)^{33}}+\frac{3G}{h_{n+1}}s_{n}^{33}\right)\right)^{1/2}-\frac{3G\,H_{n+1}}{h_{1|n+1}}\Delta\varepsilon_{q}\right\} \tag{2.32}$$

where

$$\bar{q}^{e}=\sqrt{\frac{3}{2}\bar{\mathbf{s}}^{e}\cdot\bar{\mathbf{s}}^{e}} \tag{2.33}$$

and

$$Q=\sqrt{\frac{3}{2}\bar{\mathbf{s}}^{e}\cdot\mathbf{s}_{n}} \tag{2.34}$$

The yield criterion (2.8) at stage $(n+1)$ is written as

$$q_{n+1}\left(\Delta\varepsilon_{q},\Delta\varepsilon_{33}\right)=k\left(\varepsilon_{q}\big|_{n}+\Delta\varepsilon_{q}\right) \tag{2.35}$$

Enforcing the conditions of zero stress normal to any shell lamina ($\sigma_{n+1}^{33}=0$), and using (2.27) the following equation is obtained

$$\left(1+\frac{3G}{h_{n+1}}+\frac{3G\,\Delta\varepsilon_{q}\,H_{n+1}}{q_{n+1}h_{1|n+1}}\right)p_{n+1}\,g^{33}-\left(\bar{s}^{(e)^{33}}+\frac{4G}{3}\Delta\varepsilon_{33}\,g^{33}\,g^{33}+\frac{3G}{h_{n+1}}s^{33}\right)=0 \tag{2.36}$$

Summarizing, equations (2.30), (2.32), (2.36) and the yield criterion (2.35), constitute a system of four equations with four unknowns, namely, q_{n+1}, p_{n+1}, $\Delta\varepsilon_{q}$ and $\Delta\varepsilon_{33}$. Considering $\Delta\varepsilon_{q}$ and $\Delta\varepsilon_{33}$ as the primary unknowns, equations

(2.36) and (2.35), can be solved in terms of $\Delta\varepsilon_q$, $\Delta\varepsilon_{33}$ using Newton's method as described in more detail in Appendix II.

Alternatively, a forward-Euler method can be employed to integrate the above constitutive equations, within an elastic predictor–plastic corrector scheme. The forward-Euler integration of plastic strain rate gives

$$\Delta\boldsymbol{\varepsilon}^p = \frac{3}{2h_n}\left(\mathbf{s}_{n+1}-\mathbf{s}_n\right)+\frac{3}{2}\frac{\dot{\varepsilon}_q H_n}{q_n h_{1|n}}\mathbf{s}_n \tag{2.37}$$

The final stress and its deviatoric part are written as

$$\boldsymbol{\sigma}_{n+1} = \overline{\boldsymbol{\sigma}}^e + 2G\,\Delta\varepsilon_{33}\mathbf{a} - \frac{3G}{h_n}\left(\mathbf{s}_{n+1}-\mathbf{s}_n\right)-\frac{3G\,\Delta\varepsilon_q H_n}{q_n h_{1|n}}\mathbf{s}_n \tag{2.38}$$

$$\mathbf{s}_{n+1} = \frac{1}{1+\dfrac{3G}{h_n}}\left(\overline{\mathbf{s}}^e + 2G\,\Delta\varepsilon_{33}\mathbf{a}' + \left(\frac{3G}{h_n}-\frac{3G\,H_n}{q_n h_{1|n}}\Delta\varepsilon_q\right)\mathbf{s}_n\right) \tag{2.39}$$

Squaring equation (2.39), the effective stress at the final state is calculated as follows

$$\begin{aligned} q_{n+1} = \frac{1}{\left(1+\dfrac{3G}{h_n}\right)}\Bigg\{ & \left(\overline{q}^e\right)^2 + \left(\frac{3G}{h_n}-\frac{3GH}{q_n h_{1|n}}\Delta\varepsilon_q\right)^2 \left(q_n\right)^2 \\ & + \left(\frac{6G}{h_n}-\frac{6GH_n}{q_n h_{1|n}}\Delta\varepsilon_q\right)\left(Q\right)^2 + 4G^2\,\Delta\varepsilon_{33}^2\, g^{33}\, g^{33} \\ & + 6G\,\Delta\varepsilon_{33}\left(\overline{s}^{(e)^{33}} + \left(\frac{3G}{h_n}-\frac{3GH}{q_n h_{1|n}}\Delta\varepsilon_q\right)s_n^{33}\right)\Bigg\}^{1/2} \end{aligned} \tag{2.40}$$

In addition, enforcing $\sigma_{n+1}^{33}=0$ in equation (2.38), the following equation is obtained

$$\left(1+\frac{3G}{h_n}\right)p_{n+1}\,g^{33}-\left(\overline{s}^{(e)^{33}}+\frac{4}{3}G\,\Delta\varepsilon_{33}\,g^{33}\,g^{33}+\left(\frac{3G}{h_n}-\frac{3G\,\Delta\varepsilon_q\,H}{q_n h_{1|n}}\right)s_n^{33}\right)=0 \qquad (2.41)$$

Equations (2.30), (2.40), (2.41) and the yield criterion (2.35) constitute a system of four equations with four unknowns, namely, q_{n+1}, p_{n+1}, $\Delta\varepsilon_q$ and $\Delta\varepsilon_{33}$. Considering $\Delta\varepsilon_q$ and $\Delta\varepsilon_{33}$ as the primary unknowns, equations (2.41) and (2.35) can be solved in terms of $\Delta\varepsilon_q$, $\Delta\varepsilon_{33}$ using Newton's method as described in more detail in Appendix II.

2.3 Linearization moduli

The consistent (algorithmic) rigidity moduli (Simo & Taylor, 1985) are computed from the following basic equation:

$$\mathbf{D}_{ep}^{c}=\frac{\partial\boldsymbol{\sigma}_{n+1}}{\partial\boldsymbol{\varepsilon}_{n+1}} \qquad (2.42)$$

The final stress is written in terms of its deviatoric part

$$\boldsymbol{\sigma}_{n+1}=\mathbf{s}_{n+1}+K\left(\boldsymbol{\varepsilon}_{n+1}\cdot\mathbf{1}\right)\mathbf{1} \qquad (2.43)$$

where $\mathbf{1}$ is the second-order unit tensor, and the final strain

$$\boldsymbol{\varepsilon}_{n+1}=\mathbf{e}_{n+1}+\frac{1}{3}\left(\boldsymbol{\varepsilon}_{n+1}\cdot\mathbf{1}\right)\mathbf{1} \qquad (2.44)$$

where $\mathbf{e}$ is the deviatoric strain tensor. Differentiation of equation (2.44) gives

$$\frac{\partial\mathbf{e}_{n+1}}{\partial\boldsymbol{\varepsilon}_{n+1}}=\mathbf{P} \qquad (2.45)$$

Equation (2.42), with the consideration of equations (2.43) and (2.45), leads to

$$\mathbf{D}_{ep}^{c}=\frac{\partial\boldsymbol{\sigma}_{n+1}}{\partial\boldsymbol{\varepsilon}_{n+1}}=\frac{\partial\mathbf{s}_{n+1}}{\partial\mathbf{e}_{n+1}}\mathbf{P}+3K\,\mathbf{I} \qquad (2.46)$$

In the following, four-order tensor $\partial\boldsymbol{\sigma}_{n+1}/\partial\boldsymbol{\varepsilon}_{n+1}$ is computed for the backward-Euler integration scheme and presented in the previous section. In particular using equations (2.21), (2.22) and (2.24), the final stress $\boldsymbol{\sigma}_{n+1}$ can be written as

$$\boldsymbol{\sigma}_{n+1} = \boldsymbol{\sigma}^{e} - 2G\left\{\frac{3}{2h_{n+1}}\left(\mathbf{s}_{n+1} - \mathbf{s}_{n}\right) + \frac{H\,\Delta\varepsilon_{q}}{h_{1|n+1}}\mathbf{N}_{n+1}\right\} \tag{2.47}$$

where the dimensionless tensor $\mathbf{N}$ is defined at a certain stress state $\boldsymbol{\sigma}$ by the following expression:

$$\mathbf{N} = \frac{3}{2q}\mathbf{s} \tag{2.48}$$

Using the definition of the equivalent stress in equation (2.6), it can be readily verified that

$$\frac{\partial q}{\partial \boldsymbol{\sigma}} = \mathbf{N} \tag{2.49}$$

The corresponding deviatoric stress is

$$\mathbf{s}_{n+1} = \mathbf{s}^{e} - 2G\left\{\frac{3}{2h_{n+1}}\left(\mathbf{s}_{n+1} - \mathbf{s}_{n}\right) + \frac{H\,\Delta\varepsilon_{q}}{h_{1|n+1}}\mathbf{N}_{n+1}\right\} \tag{2.50}$$

or equivalently,

$$\mathbf{s}_{n+1} = \frac{1}{1 + \dfrac{3G}{h_{n+1}} + \dfrac{3G\,H\,\Delta\varepsilon_{q}}{q_{n+1}\,h_{1|n+1}}}\left(\mathbf{s}^{e} + \frac{3G}{h_{n+1}}\mathbf{s}_{n}\right) \tag{2.51}$$

Differentiation of equation (2.50) gives

$$d\,\mathbf{s}_{n+1} = d\,\mathbf{s}^{e} - 3G\,d\left(\frac{\mathbf{s}_{n+1}}{h_{n+1}}\right) - 3G\,d\left(\frac{H\,\Delta\varepsilon_{q}}{q_{n+1}\,h_{1|n+1}}\mathbf{s}_{n+1}\right) + 3G\,d\left(\frac{1}{h_{n+1}}\right)\mathbf{s}_{n} \tag{2.52}$$

From the definition of the trial stress in equation (2.21), it is readily obtained

that

$$d\,\mathbf{s}^e = 2G\,d\,\mathbf{e}_{n+1} = 2G\,\mathbf{P}\,d\,\boldsymbol{\varepsilon}_{n+1} \tag{2.53}$$

Furthermore, it is necessary to express differential quantities $d\,\varepsilon_q$, $d\,\mathbf{s}_{n+1}$ and dq_{n+1} in terms of $d\,\boldsymbol{\varepsilon}_{n+1}$. Squaring equation (2.51) the von Mises equivalent stress at the final state is calculated as follows

$$q_{n+1} = \frac{1}{1+\dfrac{3G}{h_{n+1}}}\left\{\left(\left(q^e\right)^2 + \left(\frac{3G}{h_{n+1}}q_n\right)^2 + \frac{6G}{h_{n+1}}Q^2\right)^{1/2} - \frac{3G\,H_{n+1}}{h_{1|n+1}}\Delta\varepsilon_q\right\} \tag{2.54}$$

where

$$q^e = \sqrt{\frac{3}{2}\mathbf{s}^e\cdot\mathbf{s}^e} \tag{2.55}$$

$$q_n = \sqrt{\frac{3}{2}\mathbf{s}_n\cdot\mathbf{s}_n} \tag{2.56}$$

$$Q = \sqrt{\frac{3}{2}\mathbf{s}^e\cdot\mathbf{s}_n} \tag{2.57}$$

From the definition of the hardening modulus,

$$d\,q_{n+1} = H_{n+1}\,d\,\varepsilon_q \tag{2.58}$$

The final stress has to satisfy the yield criterion and using equations (2.35) and (2.58) this can be expressed as follows

$$\left(\left(q^e\right)^2 + \left(\frac{3G}{h_{n+1}}q_n\right)^2 + \frac{6G}{h_{n+1}}Q^2\right)^{1/2} - \frac{3G\,H_{n+1}}{h_{1|n+1}}\Delta\varepsilon_q = \left(1+\frac{3G}{h_{n+1}}\right)k\left(\varepsilon_{q|n}+\Delta\varepsilon_q\right) \tag{2.59}$$

Differentiation of equation (2.59) gives

$$\frac{2q^e\,dq^e+\left(3Gq_n\right)^2 d\left(\frac{1}{h_{n+1}^2}\right)+6G\,d\left(\frac{Q^2}{h_{n+1}}\right)}{2\left(\left(q^e\right)^2+\left(\frac{3G}{h_{n+1}}q_n\right)^2+\frac{6G}{h_{n+1}}Q^2\right)^{1/2}}-3G\,d\left(\frac{H_{n+1}\Delta\varepsilon_q}{h_{1|n+1}}\right)=$$

$$\left(1+\frac{3G}{h_{n+1}}\right)d\,k\left(\varepsilon_{q|n}+\Delta\varepsilon_q\right)+3G\,k\,d\left(\frac{1}{h_{n+1}}\right) \tag{2.60}$$

Furthermore,

$$\frac{\partial q^e}{\partial\boldsymbol{\sigma}^e}\partial\boldsymbol{\sigma}^e=\left(\frac{3}{2q^e}\mathbf{s}^e\right)\left(\mathbf{D}\,d\,\boldsymbol{\varepsilon}_{n+1}\right) \tag{2.61}$$

$$\frac{\partial Q}{\partial\boldsymbol{\sigma}^e}\partial\boldsymbol{\sigma}^e=\left(\frac{3}{4Q}\mathbf{s}_n\right)\left(\mathbf{D}\,d\,\boldsymbol{\varepsilon}_{n+1}\right) \tag{2.62}$$

$$3Gq_n\,d\left(\frac{1}{h_{n+1}}\right)=3Gq_n\left(-\frac{h'_{n+1}}{h_{n+1}^2}\right)d\,\varepsilon_q \tag{2.63}$$

$$3G\,d\left(\frac{H_{n+1}\Delta\varepsilon_q}{h_{1|n+1}}\right)=\left[-\frac{3GH_{n+1}\Delta\varepsilon_q\,h'_{1|n+1}}{h_{1|n+1}^2}+\frac{3G\Delta\varepsilon_q\,H'_{n+1}}{h_{1|n+1}}+\frac{3GH_{n+1}}{h_{1|n+1}}\right]d\,\varepsilon_q \tag{2.64}$$

$$\left(1+\frac{3G}{h_{n+1}}\right)d\,k\left(\varepsilon_{q|n}+\Delta\varepsilon_q\right)+3G\,k\,d\left(\frac{1}{h_{n+1}}\right)=\left[\left(1+\frac{3G}{h_{n+1}}\right)H_{n+1}-\frac{3Gk\,h'_{n+1}}{h_{n+1}^2}\right]d\,\varepsilon_q \tag{2.65}$$

Finally, equation (2.60) becomes

$$d\,\varepsilon_q=\frac{2G}{2A_1B_1-C_1}\left(3\mathbf{s}^e+\frac{9G}{h_{n+1}}\mathbf{s}_n\right)d\,\boldsymbol{\varepsilon}_{n+1} \tag{2.66}$$

where

$$A_1=\left(\left(q^e\right)^2+\left(\frac{3G}{h_{n+1}}q_n\right)^2+\frac{6G}{h_{n+1}}Q^2\right)^{1/2} \tag{2.67}$$

$$B_1 = \left(1+\frac{3G}{h_{n+1}}\right)H_{n+1} - \frac{3Gk\,h'_{n+1}}{h^2_{n+1}} - \frac{3G\,H_{n+1}\,\Delta\varepsilon_q\,h'_{1|n+1}}{h^2_{1|n+1}} + \frac{3G\,\Delta\varepsilon_q\,H'_{n+1}}{h_{1|n+1}} + \frac{3G\,H_{n+1}}{h_{1|n+1}} \quad (2.68)$$

$$C_1 = \left(3G\,q_n\right)^2\left(-\frac{2\,h'_{n+1}}{h^3_{n+1}}\right) + 6GQ^2\left(-\frac{h'_{n+1}}{h^2_{n+1}}\right) \quad (2.69)$$

Subsequently, equations (2.53), (2.58) and (2.66) are substituted into (2.52)

$$d\,\mathbf{s}_{n+1} = \frac{2G}{B}\mathbf{P}\,d\,\boldsymbol{\varepsilon}_{n+1} - \frac{4G}{3}\left[\frac{\left(\frac{B_1}{B}-H\right)\mathbf{N}_{n+1} + \frac{3Gq_n\,h'_{n+1}}{h^2_{n+1}}\mathbf{N}_n}{2A_1B_1 - C_1}\right]\otimes\left(3\mathbf{s}^e + \frac{9G}{h_{n+1}}\mathbf{s}_n\right)d\,\boldsymbol{\varepsilon}_{n+1} \quad (2.70)$$

where

$$B = 1+\frac{3G}{h_{n+1}} + \frac{3G\,H\,\Delta\varepsilon_q}{q_{n+1}\,h_{1|n+1}} \quad (2.71)$$

Substituting,

$$d\,\boldsymbol{\sigma}_{n+1} = \mathbf{D}\,d\,\boldsymbol{\varepsilon}_{n+1} - \frac{4G}{3}\left[\frac{\left(\frac{B_1}{B}-H\right)\mathbf{N}_{n+1} + \frac{3Gq_n\,h'_{n+1}}{h^2_{n+1}}\mathbf{N}_n}{2A_1B_1 - C_1}\otimes\left(3\mathbf{s}^e + \frac{9G}{h_{n+1}}\mathbf{s}_n\right) + \frac{3}{2}\left(1-\frac{1}{B}\right)\mathbf{P}\right]d\,\boldsymbol{\varepsilon}_{n+1} \quad (2.72)$$

so that

$$\mathbf{D}^c_{ep} = \mathbf{D} - \frac{4G}{3}\left[\frac{\left(\frac{B_1}{B}-H\right)\mathbf{N}_{n+1} + \frac{3Gq_n\,h'_{n+1}}{h^2_{n+1}}\mathbf{N}_n}{2A_1B_1 - C_1}\otimes\left(3\mathbf{s}^e + \frac{9G}{h_{n+1}}\mathbf{s}_n\right) + \frac{3}{2}\left(1-\frac{1}{B}\right)\mathbf{P}\right] \quad (2.73)$$

Finally, the condition of zero stress normal to shell laminae is imposed considering $d\,\sigma^{33} = 0$ in the rigitidy moduli of equation (2.73). The linearization

procedure leads to a non-symmetric consistent rigidity moduli.

2.4 A Note on Linearization Moduli

In the following the linearization procedure is described with simplified assumption that tensor $\mathbf{s}^e$ and $\mathbf{s}_n$ are co-axial. This results in a concise and symmetric form of rigidity moduli.

Consequently, squaring equation (2.51) and assuming for simplicity that tensor $\mathbf{s}^e$ is parallel to $\mathbf{s}_n$, the von Mises equivalent stress at the final state is calculated as follows

$$q_{n+1} = \frac{1}{1+\dfrac{3G}{h_{n+1}}}\left(q^e + \frac{3G}{h_{n+1}} q_n - \frac{3G\,H_{n+1}}{h_{1|n+1}} \Delta\varepsilon_q \right) \tag{2.74}$$

The final stress has to satisfy the yield criterion and using equations (2.35) and (2.74) this can be expressed as follows

$$q^e + \frac{3G}{h_{n+1}} q_n - \frac{3G\,H_{n+1}}{h_{1|n+1}} \Delta\varepsilon_q = \left(1+\frac{3G}{h_{n+1}}\right)\; k\left(\varepsilon_{q|n} + \Delta\varepsilon_q\right) \tag{2.75}$$

Differentiation of equation (2.75) gives

$$\begin{aligned} &\frac{3}{2q^e}\mathbf{s}^e\left(\mathbf{D}\,d\,\boldsymbol{\varepsilon}_{n+1}\right) + 3G\,q_n\left(-\frac{h'_{n+1}}{h^2_{n+1}}\right)d\,\varepsilon_q - 3G\,H_{n+1}\Delta\varepsilon_q\left(-\frac{h'_{1|n+1}}{h^2_{1|n+1}}\right)d\,\varepsilon_q \\ &-\frac{3G\,\Delta\varepsilon_q\,H'_{n+1}}{h_{1|n+1}}d\,\varepsilon_q - \frac{3G\,H_{n+1}}{h_{1|n+1}}d\,\varepsilon_q = 3G\,k\left(-\frac{h'_{n+1}}{h^2_{n+1}}\right)d\,\varepsilon_q + \left(1+\frac{3G}{h_{n+1}}\right)H_{n+1}\,d\,\varepsilon \end{aligned} \tag{2.76}$$

or equivalently,

$$d\,\varepsilon_q = \frac{2G}{A}\mathbf{N}^e\,d\,\boldsymbol{\varepsilon}_{n+1} \tag{2.77}$$

where

$$A=\left(1+\frac{3G}{h_{n+1}}\right)H_{n+1}-\frac{3G\,q_{n+1}\,h'_{n+1}}{h^2_{n+1}}-\frac{3G\,H_{n+1}\,\Delta\varepsilon_q\,h'_{1|n+1}}{h^2_{1|n+1}} + \frac{3G\,\Delta\varepsilon_q\,H'_{n+1}}{h_{1|n+1}}+\frac{3G\,H_{n+1}}{h_{1|n+1}}+\frac{3G\,h'_{n+1}\,q_n}{h^2_{n+1}} \tag{2.78}$$

Subsequently, equations (2.53), (2.58) and (2.77) are substituted into (2.52)

$$d\,\mathbf{s}_{n+1}=\frac{2G}{B}\mathbf{P}\,d\,\boldsymbol{\varepsilon}_{n+1}-\frac{4G}{3}\left(\frac{1}{B}-\frac{H}{A}\right)\mathbf{N}\otimes\mathbf{N}\,d\,\boldsymbol{\varepsilon}_{n+1} \tag{2.79}$$

where

$$B=1+\frac{3G}{h_{n+1}}+\frac{3G\,H\,\Delta\varepsilon_q}{q_{n+1}\,h_{1|n+1}} \tag{2.80}$$

Substituting,

$$d\,\boldsymbol{\sigma}_{n+1}=\mathbf{D}\,d\,\boldsymbol{\varepsilon}_{n+1}-\frac{4G}{3}\left[\left(\frac{1}{B}-\frac{H}{A}\right)\mathbf{N}_{n+1}\otimes\mathbf{N}_{n+1}+\frac{3}{2}\left(1-\frac{1}{B}\right)\mathbf{P}\right]d\,\boldsymbol{\varepsilon}_{n+1} \tag{2.81}$$

so that

$$\mathbf{D}^c_{ep}=\mathbf{D}-\frac{4G}{3}\left[\left(\frac{1}{B}-\frac{H}{A}\right)\mathbf{N}_{n+1}\otimes\mathbf{N}_{n+1}+\frac{3}{2}\left(1-\frac{1}{B}\right)\mathbf{P}\right] \tag{2.82}$$

Finally, the condition of zero stress normal to shell laminae is imposed considering $d\,\sigma^{33}=0$ in the rigidity moduli of equation (2.82).

Chapter 3

Large Strain Formulation

In this chapter, the extension of the previous model for large strains is presented, towards efficient inelastic analysis of geometrically nonlinear shells based on an additive decomposition of the rate-of-deformation tensor. Following a short presentation of the constitutive equations, their numerical intergation is described in detail.

3.1 Large-strain constitutive model

The starting point is a basic constitutive equation that relates the Jaumann rate of Kirchhoff stress $\boldsymbol{\tau}$ to the elastic part of rate-of-deformation tensor $\mathbf{d}$ by a linear hypoelastic equation of the form

$$\overset{\nabla}{\boldsymbol{\tau}} \equiv \dot{\boldsymbol{\tau}} + \boldsymbol{\tau}\mathbf{W} - \mathbf{W}\boldsymbol{\tau} = \mathbf{D}\mathbf{d}^{e} = \mathbf{D}\left(\mathbf{d} - \mathbf{d}^{p}\right) \tag{3.1}$$

where $\mathbf{d}^{e}$ and $\mathbf{d}^{p}$ are the elastic and the plastic parts of rate-of-deformation tensor $\mathbf{d}$, and $\mathbf{W}$ is the spin tensor and the Kirchhoff stress tensor $\boldsymbol{\tau}$, which is parallel to the Cauchy streess $\boldsymbol{\sigma}$ is defined as

$$\boldsymbol{\tau} = \frac{dV}{dV_0}\boldsymbol{\sigma} \tag{3.2}$$

where V_0 and V are the volume in the reference and in the current configuration, respectively.

Assuming von Mises plasticity with isotropic hardening, the yield criterion is defined by equation (2.8), where $\mathbf{s}$ is the deviatoric part of $\boldsymbol{\tau}$, and the flow rule is

$$\mathbf{d}^p = \frac{3}{2}\left(\frac{1}{E_s} - \frac{1}{E}\right)\overset{\nabla}{\mathbf{s}} + \frac{3}{2}\frac{\dot{q}}{q}\left(\frac{1}{E_T} - \frac{1}{E_s}\right)\mathbf{s} \tag{3.3}$$

which is an extension of the rate form of deformation theory for large strains (Neale, 1981). In this equation, E_s and E_T are functions of the equivalent plastic strain ε_q, defined as the time integral of $\dot{\varepsilon}_q$

$$\dot{\varepsilon}_q = \sqrt{\frac{2}{3}}\,\mathbf{d}^p \cdot \mathbf{n} \tag{3.4}$$

an equation analogous to (2.9). Using a standard inversion procedure in equation (3.1), one obtains the elastic-plastic rigidity tensor $\mathbf{D}_{ep}$ so that

$$\overset{\nabla}{\boldsymbol{\tau}} = \mathbf{D}_{ep}\,\mathbf{d} \tag{3.5}$$

For the purposes of inserting the present model within a finite element formulation, to be discussed in the next section, the constitutive equation (3.5) is written in terms of the convected rate of Kirchhoff stress tensor $\overset{\circ}{\boldsymbol{\tau}}$ defined as follows

$$\overset{o}{\boldsymbol{\tau}} = \dot{\tau}^{ij}\left(\mathbf{g}_i \otimes \mathbf{g}_j\right) \tag{3.6}$$

From continuum mechanics [Malvern, (1969), pp.402-405], one may show that the convected rate is related to the Jaumann rate as follows

$$\overset{o}{\boldsymbol{\tau}} = \overset{\nabla}{\boldsymbol{\tau}} - \mathcal{L}\mathbf{d} \tag{3.7}$$

where $\mathcal{L}$ is the geometric rigidity fourth-order tensor, with components:

$$\mathcal{L}^{ijkl} = \frac{1}{2}\left[g^{ik}\,\tau^{jl} + g^{jk}\,\tau^{il} + g^{il}\,\tau^{jk} + g^{jl}\,\tau^{ik}\right] \tag{3.8}$$

so that

$$\overset{o}{\boldsymbol{\tau}} = \left(\mathbf{D}_{ep} - \mathcal{L}\right)\mathbf{d} = \mathcal{R}\,\mathbf{d} \tag{3.9}$$

and $\mathcal{R}$ is a fourth order tensor, equal to:

$$\mathcal{R}^{ijkl} = D_{ep}^{ijkl} - \mathcal{L}^{ijkl} \tag{3.10}$$

It can be verified that the components of tensor $\mathcal{R}$ exhibit the symmetries $\mathcal{R}^{ijkl} = \mathcal{R}^{jikl} = \mathcal{R}^{ijlk}$ (due to symmetry of $\overset{o}{\boldsymbol{\tau}}$ and $\mathbf{d}$) and the nontrivial symmetry $\mathcal{R}^{ijkl} = \mathcal{R}^{klij}$.

3.2 Numerical integration of the large-strain model

To integrate the above constitutive equations, an equivalent expression of the equations in a "rotated" coordinate system is developed, using the rotation tensor $\mathbf{R}$ from the decomposition of the deformation gradient $\Delta\mathbf{F}$ that corresponds to the time step under consideration (from state n to state $n+1$). This methodology has been first suggested by Nagtegaal (1982) and it is

adjusted herein for the purpose of analyzing nonlinear shells. More specifically, the deformation gradient tensors at the beginning of the step $\mathbf{F}_n$ and at the end of the step $\mathbf{F}_{n+1}$ are related as follows

$$\Delta\mathbf{F} = \mathbf{F}_{n+1}\mathbf{F}_n^{-1} = \mathbf{g}_i \otimes \mathbf{G}^i \tag{3.11}$$

where $\mathbf{g}_i$ are the covariant base vectors at the current configuration (end of the step), and $\mathbf{G}^i$ are the contravariant base vectors at the beginning of the step. Tensor $\Delta\mathbf{F}$ is decomposed into a stretch tensor $\mathbf{U}$ and a rotation tensor $\mathbf{R}$ so that

$$\Delta\mathbf{F} = \mathbf{R}\,\mathbf{U} \tag{3.12}$$

Tensors $\mathbf{R}$ and $\mathbf{U}$ refer to the step under consideration and should be regarded as incremental quantities from state n to state $n+1$. The stretch tensor $\mathbf{U}$ is the square root of the right Cauchy-Green tensor $\mathbf{C}$ (defined as $\mathbf{C} = \Delta\mathbf{F}^T\,\Delta\mathbf{F}$), and can be written in the following expression [Ting (1985); Simo & Hughes (1998), pp. 240-244].

$$\mathbf{U} = A_1\mathbf{C}^2 + A_2\mathbf{C} + A_3\mathbf{1} \tag{3.13}$$

where $\mathbf{1}$ is the unit tensor, which can be written in the following form

$$\mathbf{1} = G_{ij}\left(\mathbf{G}^i \otimes \mathbf{G}^j\right) \tag{3.14}$$

tensor $\mathbf{C}^2$ is the square of the right Cauchy-Green tensor $\mathbf{C}$ defined as

$$\mathbf{C}^2 \equiv \mathbf{C}\mathbf{C} = g_{ik}g_{jl}G^{kj}\left(\mathbf{G}^i \otimes \mathbf{G}^l\right) \tag{3.15}$$

And A_i $(i=1,2,3)$ depend on the principal invariants of $\mathbf{U}$, defined in Appendix III. An expression similar to equation (3.13) can be derived for the inverse

tensor $\mathbf{U}^{-1}$ [Ting (1985); Simo & Hughes (1998), pp. 240-244].

$$\mathbf{U}^{-1} = B_1\mathbf{C} + B_2\mathbf{U} + B_3\mathbf{1} \tag{3.16}$$

where B_i $(i=1,2,3)$ depend on the principal invariants of $\mathbf{U}^{-1}$, also defined in Appendix III. From equations (3.13) and (3.16) the components of $\mathbf{U}$ and $\mathbf{U}^{-1}$ with respect to the $\left(\mathbf{G}^i \otimes \mathbf{G}^j\right)$ basis denoted as u_{ij}, $\overline{u}_{ij}$ respectively, are given by the following expressions

$$u_{ij} = A_1 a_{ij} + A_2 g_{ij} + A_3 G_{ij} \tag{3.17}$$

$$\overline{u}_{ij} = B_1 g_{ij} + B_2 u_{ij} + B_3 G_{ij} \tag{3.18}$$

where

$$a_{ij} = g_{ik} g_{jl} G^{kl} \tag{3.19}$$

Since $\mathbf{U}$ is symmetric and positive definite, the rotation tensor is written

$$\mathbf{R} = \Delta\mathbf{F}\,\mathbf{U}^{-1} \tag{3.20}$$

Therefore, the components of $\mathbf{R}$ with respect to the $\left(\mathbf{g}_k \otimes \mathbf{G}^j\right)$ basis are

$$r_j^k = \overline{u}_{ij} G^{ik} \tag{3.21}$$

so that

$$\mathbf{R} = r_j^k \left(\mathbf{g}_k \otimes \mathbf{G}^j\right) \tag{3.22}$$

Subsequently, the so-called rotated stress tensor $\hat{\boldsymbol{\tau}}$ and the logarithmic strain $\Delta\mathbf{E}$ are defined as follows

$$\hat{\boldsymbol{\tau}} = \mathbf{R}^T \boldsymbol{\tau}\, \mathbf{R} \tag{3.23}$$

$$\Delta\mathbf{E} = \ln\mathbf{U} \tag{3.24}$$

For computational purposes, a truncated Taylor series expression for the $\ln\mathbf{U}$ is

considered

$$\ln \mathbf{U} = (\mathbf{U}-\mathbf{1}) - \frac{1}{2}(\mathbf{U}-\mathbf{1})^2 + \frac{1}{3}(\mathbf{U}-\mathbf{1})^3 + O(\mathbf{U}-\mathbf{1})^4 \tag{3.25}$$

where the higher-order terms are omitted. Combining equations (3.17), (3.24) and (3.25), the components of $\Delta\mathbf{E}$ with respect to $\mathbf{G}^i \otimes \mathbf{G}^i$ reference basis are

$$\Delta E_{ij} \cong u_{ij}^{(11)} - \frac{1}{2} u_{ik}^{(11)} u_{jm}^{(11)} G^{km} + \frac{1}{3} u_{ik}^{(12)} u_{jm}^{(11)} G^{km} \tag{3.26}$$

where

$$u_{ij}^{(11)} = u_{ij} - G_{ij} \tag{3.27}$$

$$u_{ij}^{(12)} = u_{ik}^{(11)} u_{jm}^{(11)} G^{km} \tag{3.28}$$

If the directions of the principal stretches (*i.e.*, the eigenvectors of $\mathbf{U}$) remain fixed within the time period between t_n and t_{n+1}, it can be shown (Nagtegaal, 1982) that over that time period the following expressions can be written

$$\overset{\nabla}{\boldsymbol{\tau}} = \mathbf{R}\,\hat{\dot{\boldsymbol{\tau}}}\,\mathbf{R}^T \tag{3.29}$$

and

$$\dot{\mathbf{E}} = \mathbf{R}^T \mathbf{d}\, \mathbf{R} \tag{3.30}$$

Consequently,

$$\dot{\mathbf{E}} = \mathbf{R}^T \left(\mathbf{d}^e + \mathbf{d}^p\right) \mathbf{R} = \mathbf{R}^T \mathbf{d}^e\ \mathbf{R} + \mathbf{R}^T \mathbf{d}^p\ \mathbf{R} = \dot{\mathbf{E}}^e + \dot{\mathbf{E}}^p \tag{3.31}$$

where the elastic and plastic part of $\dot{\mathbf{E}}$ are defined as follows:

$$\dot{\mathbf{E}}^e = \mathbf{R}^T \mathbf{d}^e\ \mathbf{R} \tag{3.32}$$

$$\dot{\mathbf{E}}^p = \mathbf{R}^T \mathbf{d}^p\ \mathbf{R} \tag{3.33}$$

The proof of equations (3.29) and (3.30) is stated below in Box 3 - 1.

Box 3 - 1: Proof of equations (3.29) and (3.30).

Lemma:

If the directions of the principal stretches (*i.e.*, the eigenvectors of $\mathbf{U}$) remain fixed within the time period between t_n and t_{n+1}, it can be shown that over that time period the rate-of-deformation tensor $\mathbf{d}$ and the spin tensor $\mathbf{W}$ can be written

$$\mathbf{d}(t) = \mathbf{R}(t)\ \dot{\mathbf{E}}(t)\ \mathbf{R}^T(t) \tag{3.34}$$

$$\mathbf{W}(t) = \dot{\mathbf{R}}(t)\ \mathbf{R}^T(t) \tag{3.35}$$

where $\mathbf{E}(t) = \ln \mathbf{U}(t)$ is the logarithmic strain tensor.

Furthermore,

$$\overset{\nabla}{\boldsymbol{\tau}} = \mathbf{R}\,\dot{\hat{\boldsymbol{\tau}}}\,\mathbf{R}^T \tag{3.36}$$

Proof:

The stretch tensor $\mathbf{U}$ and the inverse tensor $\mathbf{U}^{-1}$, since $\mathbf{U}$ is symmetric and positive definite, can be written in the following expressions:

$$\mathbf{U}(t) = \sum_{i=1}^{3} \lambda_i(t)\,\mathbf{N}_i \otimes \mathbf{N}_i \tag{3.37}$$

$$\mathbf{U}^{-1}(t) = \sum_{i=1}^{3} \frac{1}{\lambda_i(t)}\,\mathbf{N}_i \otimes \mathbf{N}_i \tag{3.38}$$

In case that $\dot{\mathbf{N}}_i = \mathbf{0}$, the tensor $\dot{\mathbf{U}}$ is given by:

$$\dot{\mathbf{U}}(t) = \sum_{i=1}^{3} \dot{\lambda}_i(t)\mathbf{N}_i \otimes \mathbf{N}_i \tag{3.39}$$

Using the above equations,

$$\dot{\mathbf{U}}\mathbf{U}^{-1} = \mathbf{U}^{-1}\dot{\mathbf{U}} = \sum_{i=1}^{3} \frac{\dot{\lambda}_i(t)}{\lambda_i(t)}\mathbf{N}_i \otimes \mathbf{N}_i = \sum_{i=1}^{3} \frac{\mathrm{d}}{\mathrm{d}t}\left(\ln \lambda_i(t)\right)\mathbf{N}_i \otimes \mathbf{N}_i \tag{3.40}$$

From equation (3.12), the rate form of the deformation tensor is

$$\Delta\dot{\mathbf{F}} = \dot{\mathbf{R}}\mathbf{U} + \mathbf{R}\dot{\mathbf{U}} \tag{3.41}$$

and

$$\Delta\mathbf{F}^{-1} = \mathbf{U}^{-1}\mathbf{R}^{-1} = \mathbf{U}^{-1}\mathbf{R}^{T} \tag{3.42}$$

Using the above equations and defined the velocity gradient as

$$\mathbf{L} = \Delta\dot{\mathbf{F}}\Delta\mathbf{F}^{-1} = \left(\dot{\mathbf{R}}\mathbf{U} + \mathbf{R}\dot{\mathbf{U}}\right)\left(\mathbf{U}^{-1}\mathbf{R}^{T}\right) = \dot{\mathbf{R}}\mathbf{R}^{T} + \mathbf{R}\dot{\mathbf{U}}\mathbf{U}^{-1}\mathbf{R}^{T} \tag{3.43}$$

The symmetric and skew-symmetric parts of the velocity gradient are the rate-of-strain tensor $\mathbf{d}$ and the spin tensor $\mathbf{W}$, respectively and are defined as follows:

$$
\begin{aligned}
\mathbf{d} &= \frac{1}{2}\left(\mathbf{L}+\mathbf{L}^T\right) \\
&= \frac{1}{2}\left(\dot{\mathbf{R}}\mathbf{R}^T+\mathbf{R}\dot{\mathbf{U}}\mathbf{U}^{-1}\mathbf{R}^T-\dot{\mathbf{R}}\mathbf{R}^T+\mathbf{R}\mathbf{U}^{-1}\dot{\mathbf{U}}\mathbf{R}^T\right) \\
&= \frac{1}{2}\mathbf{R}\left(\dot{\mathbf{U}}\mathbf{U}^{-1}+\mathbf{U}^{-1}\dot{\mathbf{U}}\right)\mathbf{R}^T \\
&= \frac{1}{2}\mathbf{R}\left(\sum_{i=1}^{3}\frac{2\dot{\lambda}_i(t)}{\lambda_i(t)}\mathbf{N}_i\otimes\mathbf{N}_i\right)\mathbf{R}^T \\
&= \frac{1}{2}\mathbf{R}\left[\ln\left(\lambda_i(t)\right)\right]^{\bullet}\mathbf{N}_i\otimes\mathbf{N}_i\mathbf{R}^T \\
&= \frac{1}{2}\mathbf{R}\left(\ln\mathbf{U}\right)^{\bullet}\mathbf{R}^T \\
&= \mathbf{R}\,\dot{\mathbf{E}}\,\mathbf{R}^T
\end{aligned}
\tag{3.44}
$$

where $\mathbf{E}=\left(\ln\mathbf{U}\right)$ and

$$
\begin{aligned}
\mathbf{W} &= \frac{1}{2}\left(\mathbf{L}-\mathbf{L}^T\right) \\
&= \frac{1}{2}\left(\dot{\mathbf{R}}\mathbf{R}^T+\mathbf{R}\dot{\mathbf{U}}\mathbf{U}^{-1}\mathbf{R}^T+\dot{\mathbf{R}}\mathbf{R}^T-\mathbf{R}\mathbf{U}^{-1}\dot{\mathbf{U}}\mathbf{R}^T\right) \\
&= \frac{1}{2}\left(2\dot{\mathbf{R}}\mathbf{R}^T+\mathbf{R}\left(\dot{\mathbf{U}}\mathbf{U}^{-1}-\mathbf{U}^{-1}\dot{\mathbf{U}}\right)\mathbf{R}^T\right) \\
&= \dot{\mathbf{R}}\,\mathbf{R}^T
\end{aligned}
\tag{3.45}
$$

Tensor $\dot{\mathbf{R}}\,\mathbf{R}^T$ is skew-symmetric on account of the orthogonality of $\mathbf{R}$.

$$
\begin{aligned}
&\mathbf{R}\,\mathbf{R}^T=\mathbf{I}\Rightarrow \\
&\dot{\mathbf{R}}\mathbf{R}^T+\mathbf{R}\dot{\mathbf{R}}^T=\mathbf{0}\Rightarrow \\
&\left(\dot{\mathbf{R}}\mathbf{R}^T\right)^T=-\dot{\mathbf{R}}\mathbf{R}^T
\end{aligned}
\tag{3.46}
$$

Using equations (3.45) and (3.46), the Jaumann rate of Kirchhoff stress can be written for that time period in terms of the rate form of the “rotated stress”

$$\begin{aligned}\overset{\nabla}{\boldsymbol{\tau}} &= \dot{\boldsymbol{\tau}} + \boldsymbol{\tau}\dot{\mathbf{R}}\,\mathbf{R}^T + \mathbf{R}\,\dot{\mathbf{R}}^T\,\boldsymbol{\tau} \\ &= \mathbf{R}\,\mathbf{R}^T\,\dot{\boldsymbol{\tau}}\,\mathbf{R}\,\mathbf{R}^T + \mathbf{R}\,\mathbf{R}^T\,\boldsymbol{\tau}\dot{\mathbf{R}}\,\mathbf{R}^T + \mathbf{R}\dot{\mathbf{R}}^T\,\boldsymbol{\tau}\,\mathbf{R}\,\mathbf{R}^T \\ &= \mathbf{R}\left(\mathbf{R}^T\,\dot{\boldsymbol{\tau}}\,\mathbf{R} + \mathbf{R}^T\,\boldsymbol{\tau}\dot{\mathbf{R}} + \dot{\mathbf{R}}^T\,\boldsymbol{\tau}\,\mathbf{R}\right)\mathbf{R}^T \\ &= \mathbf{R}\,\dot{\hat{\boldsymbol{\tau}}}\,\mathbf{R}^T\end{aligned} \tag{3.47}$$

where $\hat{\boldsymbol{\tau}} = \mathbf{R}\,\boldsymbol{\tau}\,\mathbf{R}^T$ is the "rotated stress" tensor.

Using the equations (3.47) and (3.44), and the properties of the rotation tensor $\mathbf{R}$, the constitutive relation (3.1) and the flow rule (3.3) can be written for that time period in terms of the rotated stress and strain rates, as follows

$$\dot{\hat{\boldsymbol{\tau}}} = \mathbf{D}\dot{\mathbf{E}}^e = \mathbf{D}\left(\dot{\mathbf{E}} - \dot{\mathbf{E}}^p\right) \tag{3.48}$$

and

$$\dot{\mathbf{E}}^p = \frac{3}{2}\left(\frac{1}{E_s} - \frac{1}{E}\right)\dot{\hat{\mathbf{s}}} + \frac{3}{2}\frac{\dot{\hat{q}}}{\hat{q}}\left(\frac{1}{E_T} - \frac{1}{E_s}\right)\hat{\mathbf{s}} \tag{3.49}$$

where $\hat{q}$ is the von Mises equivalent stress of the rotated stress

$$\hat{q} = \sqrt{\frac{3}{2}\hat{\mathbf{s}}\cdot\hat{\mathbf{s}}} \tag{3.50}$$

One can readily show that

$$\hat{q} = \sqrt{\frac{3}{2}\mathbf{s}\cdot\mathbf{s}} = q \tag{3.51}$$

and

$$\dot{\hat{\varepsilon}}_q = \sqrt{\frac{2}{3}}\,\dot{\mathbf{E}}^p\cdot\hat{\mathbf{n}} \tag{3.52}$$

is equal to $\dot{\varepsilon}_q$, so that during plastic loading $\dot{\hat{q}} = \dot{\hat{\varepsilon}}_q H$. Using the rotated quantities of stress and strain, the hypoelastic equation (3.48) can be integrated exactly as follows

$$\hat{\boldsymbol{\tau}}_{n+1} = \boldsymbol{\tau}_n + \mathbf{D}\left(\Delta\mathbf{E} - \Delta\mathbf{E}^p\right) \tag{3.53}$$

where it was taken into account that $\hat{\boldsymbol{\tau}}_n = \boldsymbol{\tau}_n$. The above equations (3.48)-(3.53) are similar to the "small-strain" plasticity equations (2.1), (2.5)-(2.6), (2.9) and (2.23). Therefore, the integration of the elasto-plastic equations can be carried out by using a procedure similar to that described in the previous section for small-strain plasticity.

In addition, one should account for the condition of zero stress normal to the shell surface, requiring that throughout the analysis

$$\left(\boldsymbol{\tau}\mathbf{g}^3\right)\cdot\mathbf{g}^3 = \boldsymbol{\tau}\cdot\left(\mathbf{g}^3\otimes\mathbf{g}^3\right) = 0 \tag{3.54}$$

where $\mathbf{g}^3$ is the contravariant base vector normal to the shell laminae. Defining the "rotated" base vectors $\hat{\mathbf{g}}^m$ and $\hat{\mathbf{g}}_j$ as

$$\hat{\mathbf{g}}_j = \mathbf{R}^T\mathbf{g}_j \tag{3.55}$$

$$\hat{\mathbf{g}}^m = \mathbf{R}^T\mathbf{g}^m \tag{3.56}$$

the zero normal stress condition (3.54) implies that

$$\left(\hat{\boldsymbol{\tau}}\hat{\mathbf{g}}^3\right)\cdot\hat{\mathbf{g}}^3 = \hat{\boldsymbol{\tau}}\cdot\left(\hat{\mathbf{g}}^3\otimes\hat{\mathbf{g}}^3\right) = 0 \tag{3.57}$$

or equivalently

$$\hat{\tau}^{33} = \hat{s}^{33} - \hat{p}\,\hat{g}^{33} = 0 \tag{3.58}$$

where $\hat{\tau}^{km}$ are the contravariant components of $\hat{\boldsymbol{\tau}}$ with respect to the $\hat{\mathbf{g}}_i$ basis, and from equations (3.21) and (3.56) one can readily show that

$$\hat{\mathbf{g}}^m = \bar{u}_{ij} G^{im} \mathbf{G}^j \tag{3.59}$$

Using an backward-Euler scheme for the integration of the flow rule (3.49), equation (3.48) becomes

$$\hat{\boldsymbol{\tau}}_{n+1} = \boldsymbol{\tau}_n + \mathbf{D}\Delta\mathbf{E} - 3G\left(\frac{1}{E_s} - \frac{1}{E}\right)\left(\hat{\mathbf{s}}_{n+1} - \hat{\mathbf{s}}_n\right) - 3G\,\frac{\dot{\hat{q}}}{\hat{q}}\left(\frac{1}{E_T} - \frac{1}{E_s}\right)\hat{\mathbf{s}}_{n+1} \tag{3.60}$$

Expressing tensors $\hat{\boldsymbol{\tau}}_n$, $\hat{\boldsymbol{\tau}}_{n+1}$, $\Delta\mathbf{E}$, in terms of tensor bases defined by the rotated vectors $\hat{\mathbf{g}}^m$, $\hat{\mathbf{g}}^k$

$$\Delta\mathbf{E} = \Delta\mathcal{E}_{km}\left(\hat{\mathbf{g}}^k \otimes \hat{\mathbf{g}}^m\right) \tag{3.61}$$

$$\hat{\boldsymbol{\tau}}_{n+1} = \hat{\tau}^{ij}_{n+1}\left(\hat{\mathbf{g}}_i \otimes \hat{\mathbf{g}}_j\right) \tag{3.62}$$

$$\hat{\boldsymbol{\tau}}_n = \hat{\tau}^{ij}_n\left(\hat{\mathbf{g}}_i \otimes \hat{\mathbf{g}}_j\right) \tag{3.63}$$

where

$$\Delta\mathcal{E}_{km} = \Delta E_{ij}\left(\mathbf{G}^i \cdot \hat{\mathbf{g}}_m\right)\left(\mathbf{G}^j \cdot \hat{\mathbf{g}}_k\right) \tag{3.64}$$

$$\hat{\tau}^{km}_{n+1} = \hat{\tau}^{ij}_{n+1}\left(\hat{\mathbf{g}}^k \cdot \mathbf{G}_j\right)\left(\hat{\mathbf{g}}^m \cdot \mathbf{G}_i\right) \tag{3.65}$$

so that equation (3.60) becomes

$$\hat{\tau}^{ij}_{n+1} = \hat{\tau}^{ij}_n + \hat{D}^{ijkm}\Delta\mathcal{E}_{km} - 3G\left(\frac{1}{E_s} - \frac{1}{E}\right)\left(\hat{s}^{ij}_{n+1} - \hat{s}^{ij}_n\right) - 3G\,\frac{\dot{\hat{q}}}{\hat{q}}\left(\frac{1}{E_T} - \frac{1}{E_s}\right)\hat{s}^{ij}_{n+1} \tag{3.66}$$

where $\hat{D}^{ijkm}$ are the components of the 4$^{\text{th}}$ order elastic rigidity tensor $\mathbf{D}$ with respect to the rotated basis $\hat{\mathbf{g}}_i \otimes \hat{\mathbf{g}}_j \otimes \hat{\mathbf{g}}_k \otimes \hat{\mathbf{g}}_l$. For the purposes of accounting for the zero stress condition normal to shell laminae, the strain increment is

decomposed in a "known" and "unknown" part

$$\Delta\mathbf{E} = \Delta\bar{\mathbf{E}} + \Delta E_{33}\,\hat{\mathbf{a}} \tag{3.67}$$

where $\Delta\bar{\mathbf{E}}$ is the known part of the total strain increment $\Delta\mathbf{E}$ and

$$\hat{\mathbf{a}} = \hat{\mathbf{g}}^{\mathbf{3}} \otimes \hat{\mathbf{g}}^{\mathbf{3}} = \hat{g}^{3k}\hat{g}^{3m}\left(\hat{\mathbf{g}}_k \otimes \hat{\mathbf{g}}_m\right) \tag{3.68}$$

so that

$$\hat{\boldsymbol{\tau}}_{n+1} = \hat{\bar{\boldsymbol{\tau}}}^{e} + \Delta E_{33}\left(\mathbf{D}\hat{\mathbf{a}}\right) - 3G\left(\frac{1}{E_s} - \frac{1}{E}\right)\left(\hat{\mathbf{s}}_{n+1} - \hat{\mathbf{s}}_n\right) - 3G\,\frac{\dot{\hat{q}}}{\hat{q}}\left(\frac{1}{E_T} - \frac{1}{E_s}\right)\hat{\mathbf{s}}_{n+1} \tag{3.69}$$

where

$$\hat{\bar{\boldsymbol{\tau}}}^{\,e} = \boldsymbol{\tau}_n + \mathbf{D}\Delta\bar{\mathbf{E}} \tag{3.70}$$

The solution algorithm proceeds exactly as described in the previous chapter for small strains, considering the "rotated" base vectors $\hat{\mathbf{g}}_i$, $\hat{\mathbf{g}}_j$ and that $\hat{\boldsymbol{\tau}}^{33}_{n+1} = 0$. Upon calculations of $\hat{\tau}^{ij}_{n+1}$, i.e., the components of tensor $\hat{\boldsymbol{\tau}}$ with respect to the «rotated» base $\left(\hat{\mathbf{g}}_i \otimes \hat{\mathbf{g}}_j\right)$, the components τ^{pm}_{n+1} of tensor $\hat{\boldsymbol{\tau}}_{n+1}$ with respect to the current base $\left(\mathbf{g}_p \otimes \mathbf{g}_m\right)$ should be computed, using the definition of $\hat{\boldsymbol{\tau}}$. More specifically, the final stress is

$$\boldsymbol{\tau}_{n+1} = \mathbf{R}\hat{\boldsymbol{\tau}}_{n+1}\mathbf{R}^T \tag{3.71}$$

After some tensor algebra and using equation (3.21), one obtains

$$\boldsymbol{\tau}_{n+1} = r^q_p r^m_k \hat{\tau}^{ij}_{n+1}\left(\hat{\mathbf{g}}_i \cdot \mathbf{G}^q\right)\left(\hat{\mathbf{g}}_j \cdot \mathbf{G}^p\right)\left(\mathbf{g}_p \otimes \mathbf{g}_m\right) \tag{3.72}$$

and therefore the components of the final stress with respect to the current covariant basis can be computed as follows:

$$\tau^{pm}_{n+1} = r^q_p r^m_k \left(\hat{\mathbf{g}}_i \cdot \mathbf{G}^q\right)\left(\hat{\mathbf{g}}_j \cdot \mathbf{G}^p\right)\hat{\tau}^{ij}_{n+1} \tag{3.73}$$

Chapter 4

Finite Element Formulation

In the present chapter, a finite element technique is briefly presented, which simulates the nonlinear structural behavior of elastic and inelastic cylinders. It is a continuum-based formulation with finite-element discretization, through a special-purpose element, the so-called ‘‘tube-element’’. The technique is based on the large-strain formulation of Needleman (1982) and was employed for the nonlinear analysis of relatively thick elastic-plastic offshore tubular members (Karamanos and Tassoulas 1996) and, more recently, for the elastic stability of thin-walled cylinders under bending and pressure (Karamanos, 2002; Houliara and Karamanos, 2006, 2010). Herein, this element formulation is further elaborated and enhanced for the stability analysis (buckling and postbuckling) of thick-walled cylinders in the inelastic range.

4.1 Governing Equations

The cylindrical shell is considered as an elastic-plastic continuum with embedded (convected) coordinates are denoted by $\xi^i \left(i=1,2,3\right)$, as described in previous chapters. The position vector of the material point $\left(\xi^1,\xi^2,\xi^3\right)$ in the

current (deformed) configuration at time t is denoted as

$$\mathbf{x} = \mathbf{x}\left(\xi^1, \xi^2, \xi^3, t\right) \tag{4.1}$$

whereas the position of the material point $\left(\xi^1, \xi^2, \xi^3\right)$ at $t = 0$ in the reference (undeformed) configuration is denoted by

$$\mathbf{X} = \mathbf{X}\left(\xi^1, \xi^2, \xi^3\right) \tag{4.2}$$

At any material point, the covariant base vectors in the reference configuration are

$$\tilde{\mathbf{G}}_i = \frac{\partial \mathbf{X}}{\partial \xi^i} \tag{4.3}$$

and in the current configuration are

$$\mathbf{g}_i = \frac{\partial \mathbf{x}}{\partial \xi^i} \tag{4.4}$$

Furthermore, $\tilde{\mathbf{G}}^k$ and $\mathbf{g}^k$ denote the contravariant (reciprocal) base vectors in the reference and current configuration, respectively and are defined by

$$\tilde{\mathbf{G}}^k \cdot \mathbf{G}_i = \delta_i^k \tag{4.5}$$

$$\mathbf{g}^k \cdot \mathbf{g}_i = \delta_i^k \tag{4.6}$$

The constitutive equations, extensively discussed in the previous section, relate the convected rate of Kirchhoff stress tensor $\overset{\circ}{\boldsymbol{\tau}}$ to the rate of deformation tensor $\mathbf{d}$ through the relationship

$$\overset{\circ}{\boldsymbol{\tau}} = \left(\mathbf{D}_{ep} - \mathcal{L}\right)\mathbf{d} = \mathcal{R}\,\mathbf{d} \tag{4.7}$$

where $\mathbf{D}_{ep}$ is the elastoplastic rigidy fourth-order tensor and $\mathcal{L}$ is the geometric rigidity fourth-order tensor. Expressions for the components of $\mathbf{D}_{ep}$, $\mathcal{L}$ and $\mathcal{R}$

are offered in equations (2.19), (3.8) and (3.10) respectively.

Deformation is described by the rate-of-deformation (stretch) tensor $\mathbf{d}$, which is the symmetric part of the velocity gradient. It can be shown that the covariant components of the rate-of-deformation tensor are:

$$d_{kl} = \frac{1}{2}\left[V_{m/l}\left(\tilde{\mathbf{G}}^m \cdot \mathbf{g}_k\right) + V_{m/k}\left(\tilde{\mathbf{G}}^m \cdot \mathbf{g}_l\right)\right] \tag{4.8}$$

where $V_{m/l}$ is the covariant derivative of the velocity vector component V_m with respect to the reference basis.

Equilibrium is expressed through the principle of virtual work, considering an admissible displacement field $\delta\mathbf{u}$. For a continuum occupying the region V_0 and V in the reference and in the current configuration, respectively, and with boundary B in the deformed configuration, the principle of virtual work is expressed as:

$$\int_{V_0} \delta U_{i/j}\left(\tilde{\mathbf{G}}^{\mathrm{i}} \cdot \mathbf{g}_{\mathrm{k}}\right)\tau^{kj} dV_0 = \int_B \delta\mathbf{u} \cdot \mathbf{t} dB_q \tag{4.9}$$

where $\mathbf{t}$ is the surface traction and τ^{ij} are the contravariant components of the Kirchhoff stress tensor $\boldsymbol{\tau}$, which is parallel to the Cauchy stress $\boldsymbol{\sigma}$ (equation (3.2)) and

$$\delta U_{i/j} = \frac{\partial\left(\delta\mathbf{u}\right)}{\partial\xi^j} \cdot \tilde{\mathbf{G}}_{\mathrm{i}} \tag{4.10}$$

For the purpose of linearizing the equilibrium equations, the principle of virtual work is considered at a "nearby" configuration $\mathbf{x}'\left(\xi^1, \xi^2, \xi^3\right)$

$$\int_{V_0} \delta U'_{k/j}\left(\tilde{\mathbf{G}}^k \cdot \mathbf{g}'_i\right)\tau'^{ij} dV_0 = \int_{B'_q} \delta\mathbf{u}' \cdot \mathbf{t}' dB'_q \tag{4.11}$$

corresponding to stress tensor $\boldsymbol{\tau}'$ and boundary traction $\mathbf{t}'$. Considering the increment of displacement $\Delta\mathbf{u}$, defined as the difference between, vectors $\mathbf{x}'$ and $\mathbf{x}$ and the linearized form of the principle of virtual work is obtained as follows

$$\int_{V_0} \delta U_{i/j}\, S^{ijpq}\, \Delta U_{p/q}\, dV_0 = \int_{B_q} \delta \mathrm{u} \cdot \mathrm{t}'\, dB_q - \int_{V_0} \delta U_{i/j}\, \hat{\sigma}^{ji}\, dV_0 \tag{4.12}$$

where

$$\Delta U_{p/q} = \frac{\partial(\Delta u)}{\partial \xi^q} \cdot \tilde{\mathbf{G}}_p \tag{4.13}$$

components S^{ijpq} refer to the fourth-order tensor $\mathbf{S}$ and are equal to

$$S^{ijpq} = \left(\tilde{\mathbf{G}}^i \cdot g_k\right) R^{kjmq} \left(g_m \cdot \tilde{\mathbf{G}}^p\right) + \tau^{jq}\, \tilde{G}^{ip} \tag{4.14}$$

and $\hat{\sigma}^{ij}$ are the contravariant components of the non-symmetric nominal stress tensor $\hat{\boldsymbol{\sigma}}$, defined as follows:

$$\hat{\boldsymbol{\sigma}} = \frac{dV}{dV_0} \mathbf{F}^{-1} \boldsymbol{\sigma} \tag{4.15}$$

or, in component form

$$\hat{\sigma}^{ij} = \tau^{ij} \left(\mathrm{g}_k \cdot \tilde{\mathbf{G}}^j\right) \tag{4.16}$$

4.2 Finite element discretization

The numerical solution is based on the finite element discretization of linearized equilibrium equations described in the previous section. Using a finite element discretization and adopting matrix notation, the incremental displacement field can be expressed as

$$\Delta\mathbf{u} = \left[\mathbf{N}\right]\Delta\hat{\mathbf{U}} \tag{4.17}$$

in which $\left[\mathbf{N}\right]$ is the interpolation matrix that contains the appropriate shape functions and $\Delta\hat{\mathbf{U}}$ is a vector that contains the increments of nodal degrees of freedom. Using the same functions for the virtual displacements, one can write

$$\delta\mathbf{u} = \left[\mathbf{N}\right]\delta\hat{\mathbf{U}} \tag{4.18}$$

where $\delta\hat{\mathbf{U}}$ are arbitrary virtual nodal displacements.

The covariant differentiation of equations (4.17) and (4.18) results in:

$$grad\left(\Delta\mathbf{u}\right) = \left\{\Delta U_{k/l}\right\} = \left[\mathbf{B}\right]\Delta\hat{\mathbf{U}} \tag{4.19}$$

$$grad\left(\delta\mathbf{u}\right) = \left\{\delta U_{k/l}\right\} = \left[\mathbf{B}\right]\delta\hat{\mathbf{U}} \tag{4.20}$$

where $\left[\mathbf{B}\right]$ contains the derivatives of the elements of the interpolation matrix. Furthermore, in matrix form, equation (4.14) becomes,

$$\left[\mathbf{S}\right] = \left[\mathbf{W}\right]^{T}\left[\mathfrak{R}\right]\left[\mathbf{W}\right] + \left[\mathbf{C}\right] \tag{4.21}$$

where $\left[\mathbf{W}\right]$ is a 5x9 matrix containing the mixed components of the deformation gradient with respect to the reference base vectors and is introduced

$$\mathbf{W} = \begin{bmatrix} F^{1}_{.1} & F^{2}_{.1} & F^{3}_{.1} & 0 & 0 & 0 & 0 & 0 & 0 \\ 0 & 0 & 0 & F^{1}_{.2} & F^{2}_{.2} & F^{3}_{.2} & 0 & 0 & 0 \\ F^{1}_{.2} & F^{2}_{.2} & F^{3}_{.2} & F^{1}_{.1} & F^{2}_{.1} & F^{3}_{.1} & 0 & 0 & 0 \\ 0 & 0 & 0 & F^{1}_{.3} & F^{2}_{.3} & F^{3}_{.3} & F^{1}_{.2} & F^{2}_{.2} & F^{3}_{.2} \\ F^{1}_{.3} & F^{2}_{.3} & F^{3}_{.3} & 0 & 0 & 0 & F^{1}_{.1} & F^{2}_{.1} & F^{3}_{.1} \end{bmatrix} \tag{4.22}$$

The mixed components of the deformation gradient with respect to the reference base vectors are written as follows,

$$F^{i}_{.j} = \mathrm{F}\cdot\left(\tilde{\mathbf{G}}^{i}\otimes\tilde{\mathbf{G}}_{j}\right) = \left(\mathrm{F}\tilde{\mathbf{G}}_{j}\right)\cdot\tilde{\mathbf{G}}^{i} = \tilde{\mathbf{G}}^{i}\cdot\mathbf{g}_{j} \tag{4.23}$$

and $[\mathfrak{R}]$ contains the components of rigidity tensor $\mathfrak{R}$ defined in (3.10). Another auxiliary matrix $[\mathbf{C}]$ (9x9) is defined so that:

$$C_{IJ} = \tau^{j(I)q(J)} G^{i(I)p(J)} \tag{4.24}$$

with the relations between the indices given by:

I, J	i or p	j or q
1	1	1
2	2	1
3	3	1
4	1	2
5	2	2
6	3	2
7	1	3
8	2	3
9	3	3

(4.25)

This arrangement is consistent with that of gradient components in (4.19)

$$\{\Delta U_{p/q}\} = \begin{bmatrix} \Delta U_{1/1} \\ \Delta U_{2/1} \\ \Delta U_{3/1} \\ \Delta U_{1/2} \\ \Delta U_{2/2} \\ \Delta U_{3/2} \\ \Delta U_{1/3} \\ \Delta U_{2/3} \\ \Delta U_{3/3} \end{bmatrix} \tag{4.26}$$

For arbitrary virtual displacements $\delta\hat{\mathbf{U}}$ the following set of linearized equations of the discretized continuum is obtained:

$$[\mathbf{K}]\Delta\hat{\mathbf{U}} = \mathbf{F}_{ext} - \mathbf{F}_{int} \tag{4.27}$$

where $[\mathbf{K}]$ is the incremental stiffness matrix

$$[\mathbf{K}] = \int_{V_0} [\mathbf{B}]^T [\mathbf{S}][\mathbf{B}] dV_0 \tag{4.28}$$

and $\mathbf{F}_{ext}$, $\mathbf{F}_{int}$ are the external and internal load vectors respectively:

$$\mathbf{F}_{ext} = \int_{B_q} [\mathbf{N}]^T \mathbf{t}' dB_q \tag{4.29}$$

$$\mathbf{F}_{int} = \int_{V_0} [\mathbf{B}]^T [\mathbf{W}]^T \boldsymbol{\tau} dV_0 \tag{4.30}$$

Equilibrium is achieved when $\mathbf{F}_{int}$ equals $\mathbf{F}_{ext}$. An incremental Newton-Raphson iterative numerical procedure is employed, enhanced to enable the tracing of postbuckling "snap-back" equilibrium paths through an arc-length algorithm, which monitors the value of the so-called "arc-length parameter" (Crisfield, 1983).

4.3 "Tube-Element" Description

The cylinder is discretized through a three-node "tube element" (see Figure 4 - 1), introduced in Karamanos and Tassoulas (1996) for the analysis of thick walled tubes also employed for analysis of thin-walled elastic cylinders. This element combines longitudinal (beam-type) with cross-sectional deformation. The convected coordinates $\left(\xi^1,\xi^2,\xi^3\right)$ are assumed in the hoop, axial and radial direction in the reference configuration respectively and are denoted as $\left(\theta,\zeta,\rho\right)$.

Nodes are located along the cylinder axis, which lies on the plane of bending, and each node possesses three degrees of freedom (two translational and one rotational). A reference line is chosen within the cross-section at node $\left(k\right)$ and

a local Cartesian coordinate system is defined, so that the $\bar{x}, \bar{y}$ axes define the cross-sectional plane. The orientation of node (k) is defined by the position of three orthonormal vectors $\mathbf{e}_x^{(k)}$, $\mathbf{e}_y^{(k)}$ and $\mathbf{e}_z^{(k)}$. For in-plane (ovalization) deformation, fibers initially normal to the reference line remain normal to the reference line. Furthermore, those fibers may rotate in the out-of-plane direction by angle $\gamma(\theta)$. Using quadratic interpolation in the longitudinal direction, the position vector $\mathbf{x}(\theta,\zeta,\rho)$ of an arbitrary point at the deformed configuration is:

$$\mathbf{x}(\theta,\zeta,\rho)=\sum_{k=1}^{3}\left[\left(\mathbf{x}^{(k)}+\mathbf{r}^{(k)}(\theta)+\rho\mathbf{n}^{(k)}(\theta)+\rho\gamma(\theta)\mathbf{e}_z^{(k)}\right)N^{(k)}(\zeta)\right] \qquad (4.31)$$

where $\mathbf{x}^{(k)}$is the position vector of node (k), $\mathbf{r}^{(k)}(\theta)$ is the position of the reference line at a certain cross-section relative to the corresponding node (k), $\mathbf{n}^{(k)}(\theta)$ is the "in-plane" outward normal of the reference line at the deformed configuration and $N^{(k)}(\zeta)$ is the corresponding Lagrangian quadratic polynomial. Using nonlinear ring theory (Brush and Almroth, 1975), vector functions $\mathbf{r}^{(k)}(\theta)$ and $\mathbf{n}^{(k)}(\theta)$, can be expressed in terms of the radial, tangential and out-of-plane displacements of the reference line, denoted as $w(\theta), v(\theta), u(\theta)$, respectively. The position of the reference line at the cross-section with the respect to node (k) is

$$\mathbf{r}^{(k)}(\theta)=x_r(\theta)\mathbf{e}_x^{(k)}+y_r(\theta)\mathbf{e}_y^{(k)}+z_r(\theta)\mathbf{e}_z^{(k)} \qquad (4.32)$$

where $x_r(\theta)$, $y_r(\theta)$ and $z_r(\theta)$ are reference line coordinates with respect to the local cross-section axes and are discretized as

$$\begin{aligned} x_r(\theta) &= \left[r + w(\theta)\right]\cos\theta - v(\theta)\sin\theta \\ y_r(\theta) &= \left[r + w(\theta)\right]\sin\theta + v(\theta)\cos\theta \\ z_r(\theta) &= u(\theta) \end{aligned} \tag{4.33}$$

The deformation functions $w(\theta)$, $v(\theta)$, $u(\theta)$ and $\gamma(\theta)$ are discretized as follows:

$$w(\theta) = a_0 + a_1 \sin\theta + \sum_{n=2,4,6,\ldots} a_n \cos n\theta + \sum_{n=3,5,7,\ldots} a_n \sin n\theta \tag{4.34}$$

$$v(\theta) = -a_1 \sin\theta + \sum_{n=2,4,6,\ldots} b_n \sin n\theta + \sum_{n=3,5,7,\ldots} b_n \cos n\theta \tag{4.35}$$

$$u(\theta) = \sum_{n=2,4,6,\ldots} c_n \cos n\theta + \sum_{n=3,5,7,\ldots} c_n \sin n\theta \tag{4.36}$$

$$\gamma(\theta) = \sum_{n=0,2,4,6,\ldots} \gamma_n \cos n\theta + \sum_{n=1,3,5,7,\ldots} \gamma_n \sin n\theta \tag{4.37}$$

Coefficients a_n, b_n refer to in-plane cross-sectional deformation, and express the ovalization of the cross-section, whereas c_n, γ_n refer to out-of-plane cross-sectional deformation, expressing cross-sectional warping.

The outward unit vector $\mathbf{n}^{(k)}(\theta)$, normal to the reference line can be written as:

$$\mathbf{n}^{(k)}(\theta) = n_x(\theta)\mathbf{e}_x^{(k)} + n_y(\theta)\mathbf{e}_y^{(k)} \tag{4.38}$$

where

$$\mathrm{n}_x = \frac{dy_r/d\theta}{ds_r/d\theta} \tag{4.39}$$

$$\mathrm{n}_y = \frac{dx_r/d\theta}{ds_r/d\theta} \tag{4.40}$$

and

$$\frac{dy_r}{d\theta} = -\left[r + w(\theta) + v'(\theta)\right]\sin\theta + \left[w'(\theta) - v(\theta)\right]\cos\theta \tag{4.41}$$

$$\frac{dx_r}{d\theta} = -\left[r + w(\theta) + v'(\theta)\right]\cos\theta - \left[w'(\theta) - v(\theta)\right]\sin\theta \tag{4.42}$$

$$\frac{ds_r}{d\theta} = \sqrt{r^2 + 2r\left[w(\theta) + v'(\theta)\right] + \left[w(\theta) + v'(\theta)\right]^2 + \left[w'(\theta) - v(\theta)\right]^2} \tag{4.43}$$

The position vector expressed through (4.31) can be written alternatively as follows

$$\begin{aligned}\mathbf{x}(\theta,\zeta,\rho) = \sum_{k=1}^{3}\Big[\Big(\mathbf{x}^{(k)} + \left(x_r + \rho n_x\right)\mathbf{e}_x^{(k)} + \left(y_r + \rho n_y\right)\mathbf{e}_y^{(k)} \\ + \left(z_r + \rho\gamma\right)\mathbf{e}_z^{(k)}\Big)N^{(k)}(\zeta)\Big]\end{aligned} \tag{4.44}$$

and differentiating this expression with respect to the time variable and omitting higher-order terms the following for the velocity vector is obtained:

$$\begin{aligned}\dot{\mathbf{x}} = \mathbf{v}(\theta,\zeta,\rho) = \sum_{k=1}^{3}\Big\{\Big[\dot{\mathbf{x}}^{(k)} + \left(\dot{x}_r + \rho\dot{n}_x\right)\mathbf{e}_x^{(k)} + \left(\dot{y}_r + \rho\dot{n}_y\right)\mathbf{e}_y^{(k)} \\ + \left(y_r + \rho n_y\right)\dot{\mathbf{e}}_y^{(k)} + \left(\dot{z}_r + \rho\dot{\gamma}\right)\mathbf{e}_z^{(k)} + \left(z_r + \rho\gamma\right)\dot{\mathbf{e}}_z^{(k)}\Big]N^{(k)}(\zeta)\Big\}\end{aligned} \tag{4.45}$$

Equation (4.45) can be rewritten in terms of incremental displacements

$$\begin{aligned}\Delta\mathbf{u}(\theta,\zeta,\rho) = \sum_{k=1}^{3}\Big\{\Big[\Delta\mathbf{u}^{(k)} + \left(\Delta x_r + \rho\Delta n_x\right)\mathbf{e}_x^{(k)} \\ + \left(\Delta y_r + \rho\Delta n_y\right)\mathbf{e}_y^{(k)} + \left(y_r + \rho n_y\right)\Delta\mathbf{e}_y^{(k)} \\ + \left(\Delta z_r + \rho\Delta\gamma\right)\mathbf{e}_z^{(k)} + \left(z_r + \rho\gamma\right)\Delta\mathbf{e}_z^{(k)}\Big]N^{(k)}(\zeta)\Big\}\end{aligned} \tag{4.46}$$

Considering vector $\Delta\hat{\mathbf{U}}$, which contains the increments of nodal degrees of freedom of the ‘‘tube-element’’ as follows:

$$\left\{\Delta\hat{\mathbf{U}}\right\}=\begin{bmatrix}\vdots\\ \Delta u_2^{(k)}\\ \Delta u_3^{(k)}\\ \Delta\theta_1^{(k)}\\ \vdots\\ \Delta\alpha_i^{(k)}\\ \vdots\\ \Delta b_i^{(k)}\\ \vdots\\ \Delta c_i^{(k)}\\ \vdots\\ \Delta\gamma_i^{(k)}\\ \vdots\end{bmatrix} \tag{4.47}$$

The covariant base vectors that are tangential to the coordinate lines (θ,ζ,ρ) can by calculated by differentiation with respect to the local coordinates of the position vector as follows:

$$\mathbf{g}_1=\mathbf{g}_\theta=\frac{\partial\mathbf{x}}{\partial\theta}=\sum_{k=1}^{3}\left[\left(\frac{d\mathbf{r}^{(k)}(\theta)}{d\theta}+\rho\frac{d\mathbf{n}^{(k)}(\theta)}{d\theta}+\rho\frac{d\gamma(\theta)}{d\theta}\mathbf{e}_z^{(k)}\right)N^{(k)}(\zeta)\right] \tag{4.48}$$

$$\mathbf{g}_2=\mathbf{g}_\zeta=\frac{\partial\mathbf{x}}{\partial\zeta}=\sum_{k=1}^{3}\left[\left(\mathbf{x}^{(k)}+\mathbf{r}^{(k)}(\theta)+\rho\mathbf{n}^{(k)}(\theta)+\rho\gamma(\theta)\mathbf{e}_z^{(k)}\right)\frac{dN^{(k)}(\zeta)}{d\zeta}\right] \tag{4.49}$$

$$\mathbf{g}_3=\mathbf{g}_\rho=\frac{\partial\mathbf{x}}{\partial\rho}=\sum_{k=1}^{3}\left[\left(\mathbf{n}^{(k)}(\theta)+\gamma(\theta)\mathbf{e}_z^{(k)}\right)N^{(k)}(\zeta)\right] \tag{4.50}$$

Considering the covariant base vectors in the reference configuration $\tilde{\mathbf{G}}_1,\tilde{\mathbf{G}}_2,\tilde{\mathbf{G}}_3$, appropriate differentiation of (4.46) and the definition of vector $\Delta\hat{\mathbf{U}}$, matrix $[\mathbf{B}]$ is formed to be used in equation (4.19).

For the purposes of the present study, a 16^{th} degree expansion is used for $w(\theta), v(\theta), u(\theta)$ and $\gamma(\theta)$ [considering $n\le 16$ in equations (4.34)-(4.37)], and

four “tube-elements” per half wavelength are employed. Regarding the number of integration points, 23 equally spaced integration points around the half-circumference, five Gauss points in the radial (through the thickness) direction and two Gauss points in the longitudinal direction of the “tube element” are considered (reduced integration scheme) following relevant convergence studies reported in previous works (Karamanos, 2002; Houliara & Karamanos, 2010).

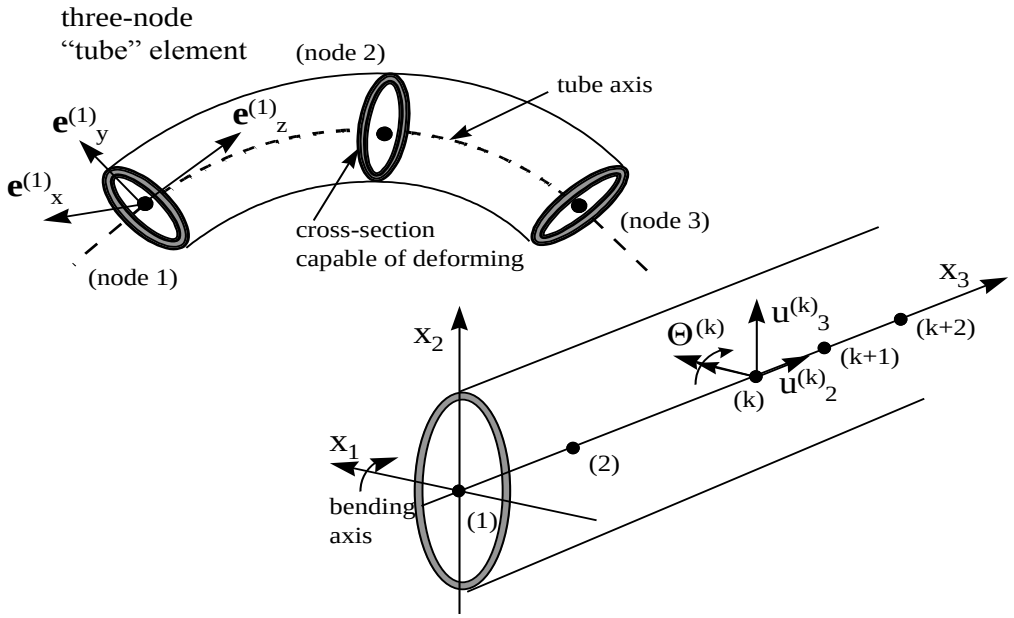

(a)

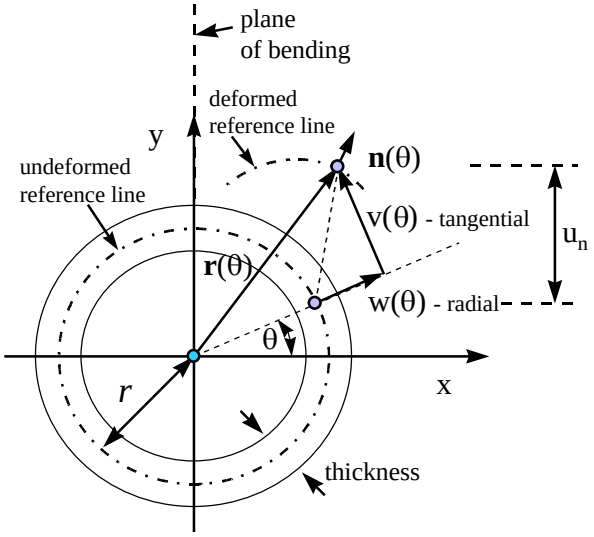

(b)

Figure 4 - 1: (a) Three-node “tube element” and deformation parameters; x_1, x_2 is the plane of bending, (b) Cross-sectional ovalization (in-plane) deformation parameters

4.4 Bifurcation in the inelastic range

Detection of bifurcation from prebuckling to post-buckling is performed upon convergence of solution at the end of each loading increment, adopting Hill's "comparison solid" concept, as described in detail by Hutchinson (1974). The use of "comparison solid" yields lower bound, yet quite accurate, estimates of the bifurcation load, introducing the quadratic functional F :

$$F = \int_V \left(R^{ijkl} \Delta E_{ij} \Delta E_{kl} + \tau^{ij} \Delta U^k_{/j} \Delta U_{k/j} \right) dV \tag{4.51}$$

The positive definiteness of functional (4.51) ensures uniqueness of solution and stability. At the stage where F becomes non-positive definite, bifurcation occurs. Using the following expressions,

$$\tau^{ij} \Delta U^k_{/j} \Delta U_{k/j} = \tau^{ij} \Delta U_{m/j} \tilde{G}^{mk} \Delta U_{k/j} \tag{4.52}$$

$$\Delta E_{ij} = \frac{1}{2} \left[\left(\tilde{\mathbf{G}}^k \cdot \mathbf{g}_p \right) \Delta U_{k/q} + \left(\tilde{\mathbf{G}}^k \cdot \mathbf{g}_q \right) \Delta U_{k/p} \right] \tag{4.53}$$

and the finite element discretization procedure described in the previous paragraphs, functional F can be written in the following quadratic form in terms of "stiffness matrix" $[\mathbf{K}']$

$$F = \Delta \hat{\mathbf{U}}^T [\mathbf{K}'] \Delta \hat{\mathbf{U}} \tag{4.54}$$

where

$$[\mathbf{K}'] = \int_{V_0} [\mathbf{B}]^{\mathrm{T}} [\mathbf{S}] [\mathbf{B}] dV_0 \tag{4.55}$$

and

$$[\mathbf{S}] = [\mathbf{W}]^{\mathrm{T}} [\mathcal{R}'] [\mathbf{W}] + [\mathbf{C}] \tag{4.56}$$

and $[\mathcal{R}']$ is the constitutive matrix containing the tangent elastic-plastic moduli $\mathcal{R}^{ijkl}$ of J_2 - non associative flow theory moduli. Therefore, the positive definiteness of F is equivalent to the positive definiteness of $[\mathbf{K}']$, examined through the evaluation of its eigenvalues at the end of each loading increment. Bifurcation occurs when the smallest eigenvalue of $[\mathbf{K}']$ becomes equal to zero.

Chapter 5

Continuity of Plastic Flow

In previous chapters the non-associative plasticity model has been presented in detail. The main feature of this work has been the adoption of the deformation theory, such that the production of plastic strain is increased for non-proportional loading paths. Using this approach, the elastic-plastic moduli become less stiff, and therefore, this enables improved predictions of the bifurcation load.

As described in Chapter 2, the rate form of the J_2 - deformation theory expressed by equation (2.10) implies that the plastic strain increment is composed by two components, one normal to the yield surface (as in the case of classical J_2 - flow theory) and one tangent to the yield surface. Therefore, the present non-associative theory is associated with higher plastic strains when compared with J_2 - flow associative theory.

5.1 Plastic production ratio

In order to quantify the production of plastic flow, the so-called plastic production ratio is adopted, defined by Hughes and Shakib (1986), as follows:

$$w(\theta) = \frac{\left\|\dot{\mathbf{e}}^{p}\right\|}{\left\|\dot{\mathbf{e}}\right\|} \tag{5.1}$$

where $\dot{\mathbf{e}}$ is the deviatoric part of incremental strain tensor $\dot{\boldsymbol{\varepsilon}}$, and $\dot{\mathbf{e}}^{p}$ is the plastic part of $\dot{\mathbf{e}}$. The value of w depends on angle θ between the outward normal $\mathbf{n}$ and the deviatoric strain increment $\dot{\mathbf{e}}$, as shown in Figure 5 - 1. Equivalently, equation (5.1) can be written in a normalized form:

$$w^{*}(\theta) = w(\theta)\left(1+\frac{H}{3G}\right) \tag{5.2}$$

In the framework of associated plastic flow, the plastic strain rate can be written as

$$\dot{\boldsymbol{\varepsilon}}^{p} = \frac{3\dot{\varepsilon}_{q}}{2q}\mathbf{s} \tag{5.3}$$

where the equivalent plastic strain rate is

$$\dot{\varepsilon}_{q} = \frac{3}{2qH}\mathbf{s}\cdot\dot{\mathbf{s}} \tag{5.4}$$

or equivalently

$$\dot{\varepsilon}_{q} = \frac{1}{1+\frac{H}{3G}}\sqrt{\frac{2}{3}}\left(\mathbf{n}\cdot\dot{\mathbf{e}}\right) \tag{5.5}$$

offering a measure of plastic strain-rate dependence on the direction of strain increment with respect to the outward unit normal to the yield surface $\mathbf{n}$. The

value of w can be expressed as

$$w(\theta)=\frac{1}{1+\frac{H}{3G}}\cos\theta \tag{5.6}$$

or equivalently in its normalized form

$$w^{*}(\theta)=\cos\theta \tag{5.7}$$

where

$$\cos\theta=\frac{(\mathbf{n}\cdot\dot{\mathbf{e}})}{\|\dot{\mathbf{e}}\|} \tag{5.8}$$

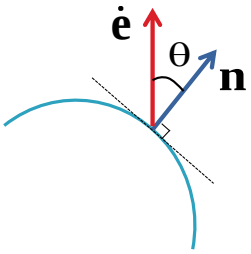

Figure 5 - 1: Schematic representation of deviatoric strain increment and the outward unit normal to von Mises surface $\mathbf{n}$.

In classical plasticity, loading paths tangential to the yield surface $(\theta=\pi/2)$ imply zero plastic deformation, so that $w^{*}=0$ for $\theta=\pi/2$ as shown in Figure 5 - 2, corresponding to elastic behavior. Clearly, for $\theta>\pi/2$ the behavior is also elastic.

For the non-associative flow rule under consideration as expressed in equation (2.10) and using the definition of plastic production ratio in equation (5.1), the following expression for the plastic production ratio can be obtained:

$$w^*(\theta)=\left(1+\frac{H}{3G}\right)\sqrt{A+B\cos^2\theta} \tag{5.9}$$

where

$$A=\frac{1}{\left(1+\frac{h(\varepsilon_q)}{3G}\right)^2} \tag{5.10}$$

$$B=\frac{1}{\left(1+\frac{H}{3G}\right)^2}-\frac{1}{\left(1+\frac{h(\varepsilon_q)}{3G}\right)^2} \tag{5.11}$$

where $h(\varepsilon_q)$ is a function of the Young's modulus and secant modulus, and is defined by equation (2.15).

In Figure 5 - 2 the value of w^* from the present model, expressed in equations (5.9) - (5.11), is also plotted in terms of angle θ with the two continuous lines. The two lines correspond to two levels of equivalent plastic strain ε_q equal to 3% and 5% respectively. There exists a discontinuity at $\theta=\pi/2$, which is due to the non-zero tangential component of $\dot{\boldsymbol{\varepsilon}}^p$. Apart from the fact that this discontinuity is not consistent with the physical problem, it may cause numerical convergence problems. Therefore, a zero value of $w^*=0$ at $\theta=\pi/2$ is desired, and a modification of the plastic flow equation (2.5) is proposed, so that the tangential (non-associative) part of the right-hand side vanishes for θ values approaching $\pi/2$. Towards this purpose, a modified value

of the secant modulus E_s is considered in terms of θ, denoted as $\bar{E}_s$, as follows:

$$\bar{E}_s\left(\varepsilon_q,\theta\right)=E_s\left(\varepsilon_q\right)\left(1-sin^n\theta\right)+E\left(sin^n\theta\right),\ \theta\geq\theta_0 \tag{5.12}$$

where θ_0 is a threshold value quite close to $\pi/2$ and n is a large-valued exponent. Therefore, the values of $h\left(\varepsilon_q\right)$ is replaced by $\bar{h}\left(\varepsilon_q,\theta\right)$

$$\bar{h}\left(\varepsilon_q,\theta\right)=\frac{E\bar{E}_s\left(\varepsilon_q,\theta\right)}{E-\bar{E}_s\left(\varepsilon_q,\theta\right)} \tag{5.13}$$

and the plastic ratio becomes a continuous function of θ, approaching smoothly the value of zero for $\theta=\pi/2$. This is shown in Figure 5 - 2 with the dotted lines for values of θ_0 and n equal to 75° and 300 respectively. In such a case,

$$\bar{w}^*\left(\theta\right)=\left(1+\frac{H}{3G}\right)\sqrt{\bar{A}+\bar{B}\,cos^2\theta} \tag{5.14}$$

$$\bar{A}=\frac{1}{\left(1+\dfrac{\bar{h}\left(\varepsilon_q\right)}{3G}\right)^2} \tag{5.15}$$

$$\bar{B}=\frac{1}{\left(1+\dfrac{H}{3G}\right)^2}-\frac{1}{\left(1+\dfrac{\bar{h}\left(\varepsilon_q\right)}{3G}\right)^2} \tag{5.16}$$

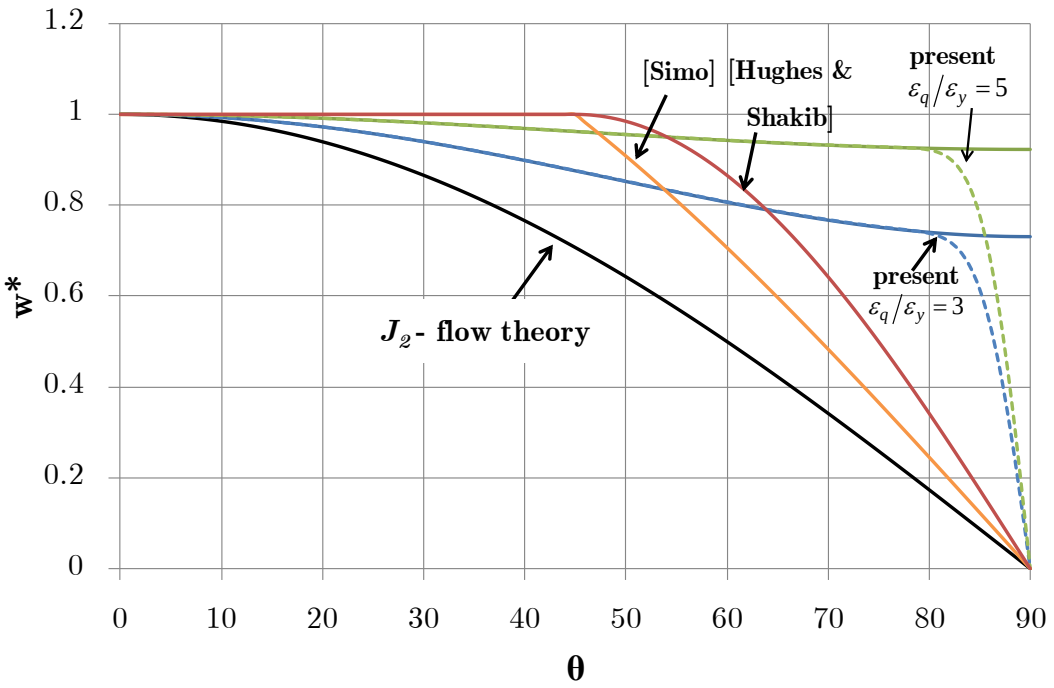

Figure 5 - 2: Variation of plastic production ratio w^* in terms of θ for various plasticity models.

5.2 Comparison with other plasticity models

The normalized values of plastic production ratio w^* in terms of θ, shown in Figure 5 - 2, are also compared with those proposed in the models by Hughes and Shakib (1986) and Simo (1987). The non-dimensional measures of the plastic strain rate for the Hughes and Shakib (1986) model is defined in equation (5.17).

$$w^*(\theta) = \left(1 + \frac{H}{3G}\right) \frac{\cos\theta}{\left(1 + \frac{H'}{3G}\right)} \tag{5.17}$$

where

$$H' = 3G\left[\left(1+\frac{H}{3G}\right)\frac{\cos\theta}{\cos\psi}-1\right] \tag{5.18}$$

$$\psi = \begin{cases} 0 & \text{if } 0 \le \theta \le \theta_{crit} \\ \dfrac{\left(\dfrac{\pi}{2}\right)\left(\theta-\theta_{crit}\right)}{\left(\dfrac{\pi}{2}-\theta_{crit}\right)} & \text{if } \theta_{crit} \le \theta < \dfrac{\pi}{2} \end{cases} \tag{5.19}$$

Loading paths tangential to the smooth yield surface are assumed to engender elastic response and a simple cosine interpolation between θ_{crit} and $\pi/2$ is used to reduce $w^*(\theta)$ to zero.

In the "pseudo-corner" model proposed by Simo (1987), the plastic strain rate can be written as

$$\dot{\mathbf{e}}^p = \dot{\gamma}\left(\mathbf{n}+\hat{\delta}\mathbf{m}\right) \tag{5.20}$$

where

$$\mathbf{n} = \frac{\mathbf{s}}{\|\mathbf{s}\|} \tag{5.21}$$

$$\mathbf{m} = \frac{\dot{\mathbf{e}}-\left(\mathbf{n}\cdot\dot{\mathbf{e}}\right)\mathbf{n}}{\left\|\dot{\mathbf{e}}-\left(\mathbf{n}\cdot\dot{\mathbf{e}}\right)\mathbf{n}\right\|} \tag{5.22}$$

$$\dot{\gamma} = \mathbf{n}\cdot\dot{\mathbf{e}} \tag{5.23}$$

$$\hat{\delta} = \begin{cases} \tan\theta & \text{for } \theta \in \left[-\theta_{crit},\ \theta_{crit}\right] \\ \tan\theta_{crit} & \text{for } |\theta| \in \left[\theta_{crit},\ \dfrac{\pi}{2}\right] \end{cases} \tag{5.24}$$

The non-dimensional measures of the plastic strain rate is defined as

$$w^*(\theta) = \frac{\cos\theta}{\beta}\sqrt{1+\hat{\delta}} \tag{5.25}$$

where

$$\beta = \left(1+\frac{H}{3G}\right) \tag{5.26}$$

In Simo's model, the production of plastic flow coincides with that of J_2 - corner theory for $\theta \in \left[-\theta_{crit}, \theta_{crit}\right]$, and lies between the corresponding values for J_2-flow and J_2-deformation theories for $|\theta| \in \left[\theta_{crit}, \frac{\pi}{2}\right]$. Note that, for the needs of presentation of the results, the value of θ_{crit} equal to 45° is used for the both two models, as shown in Figure 5 - 2.

Chapter 6

Verification Results

In this chapter, numerical results for three benchmark problems of metal shell buckling are obtained to validate the numerical methodology described in the previous chapters. Large-strains are considered with the material model formulation described in Chapter 3. Furthermore, the integration of constitutive models is performed with the backward-Euler method described in section 2.2. The first problem refers to initial wrinkling of stainless steel tubes under uniform axial compression, and comparison with both experimental data and analytical predictions is conducted. The second problem refers to axially compressed imperfect metal cylinders, where the present results are compared with available semi-analytical solutions. The third problem refers to an elongated cylindrical shell, referred to as "tube", and subjected to longitudinal bending, which has also been tested experimentally. In those problems, comparison between the predictions of the J_2 - non-associative plasticity model and those from the classical associative model (J_2 - flow rule) is conducted, towards verifying the reliable applicability of the non-associative model in thick shell buckling problems.

6.1 Initial wrinkling of metal tubes under axial compression

Long, relatively thick tubes and line pipes used to transport fluids experience axial, shell-type buckling mainly when restrained from lateral movement. This, for example, is the case for a pipeline buried in a trench or resting on a deformable foundation. In offshore operations, compression can be caused by the passage of hot hydrocarbons carried from the well to a central gathering point by buried flow lines. Motion of the ground caused by fault movement, landslides, ground subsidence, permafrost melting, or soil liquefaction, can also result in severe compression of the lines. Both loading scenaria can impose compressive strains high enough to result in axial buckling. In most onshore and offshore pipeline operations, diameter-to-thickness ratios (D/t_s) and steel grades are such that buckling occurs in the plastic range.

Unlike elastic shell buckling, in which collapse is sudden and catastrophic, plastic buckling failure is preceded by a cascade of events, where the first instability and collapse can be separated by average strains of 1–5%. The behavior is summarized schematically in the axial stress-shortening response of a long tube shown in Figure 6 - 1 (Bardi and Kyriakides, 2006).

The cylinder is under uniform axial compression, so that a constant state of stress exists around the circumference. In rather thick cylinders, the cylinder material enters into the inelastic range and then buckles. First buckling corresponds to an axisymmetric wavy pattern the cylinder axial stiffness is significantly reduced. Figure 6 - 1 shows schematically the response of such a

cylinder, with a rounded stress-strain material curve that exhibits considerable hardening in the inelastic (post-yield) range.

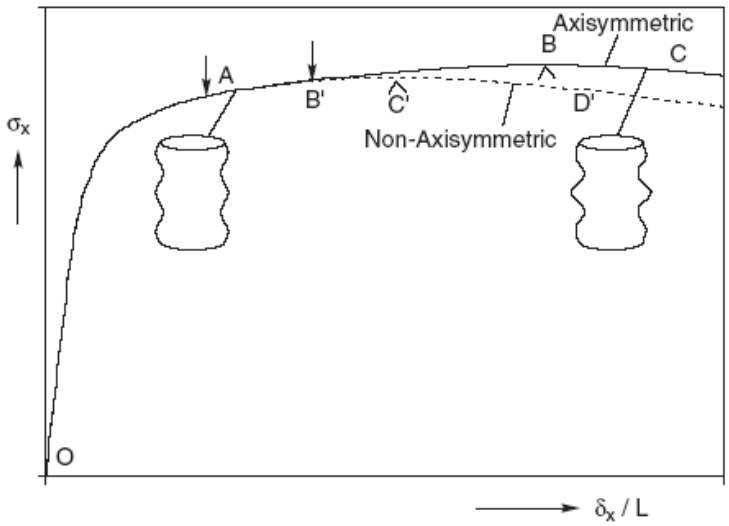

Figure 6 - 1: Stress-shortening responses expected in a compression test of an inelastic circular cylinder. Shown is the onset of wrinkling (A) followed by axisymmetric collapse (B) or non-axisymmetric collapse (C') (Bardi and Kyriakides, 2006).

Upon formation of those axisymmetric waves, the response depends on the value of the D/t_s ratio. In thicker cylinders (*i.e.* low values of D/t_s ratio), a limit load on the load-displacement path occurs, followed by a localization of the axisymmetric wavy pattern, where a single wave develops much more than all the other waves. Subsequently, a second bifurcation to a non-axisymmetric deformation pattern may occur, resulting in a further decrease of axial load capacity.

In thinner cylinders, the transition from the axisymmetric wavy pattern to a non-axisymmetric deformation state is observed before the occurrence of a limit load. This implies a further decrease of cylinder axial stiffness, so that a limit

point occurs quite early. Beyond this limit point, localization of deformation usually occurs, resulting in cylinder collapse and failure.

Numerical results for benchmark problems of metal shell buckling are obtained to validate the numerical methodology described in the previous chapters. The first problem refers to wrinkling of stainless steel tubes under uniform axial compression, and comparison with both experimental data and analytical predictions is conducted. Bifurcation analysis of perfect cylinders, associated with the initial development of wrinkles is described first. Subsequently, simulation of gradual development and localization of wrinkles in initially imperfect cylinders is presented using a nonlinear incremental analysis.

The tubes under consideration have been tested by Bardi and Kyriakides (2006a) and are made of stainless steel material SAF 2507 super-duplex, which can be described for uniaxial tension through a Ramberg-Osgood stress-strain curve [equation (6.1)]

$$\varepsilon = \frac{\sigma}{E}\left[1+\frac{3}{7}\left(\frac{\sigma}{\bar{\sigma}}\right)^{n+1}\right] \tag{6.1}$$

where the values of E, $\bar{\sigma}$ and n have been determined through an appropriate tensile test equal to 194 GPa, 572 MPa and 13 respectively. The cylindrical shells are thick-walled with diameter-to-thickness ratio between 20 and 50, and are appropriately machined so that the buckling area can be considered free of boundary conditions. More details on the specimens and the experimental procedure can be found in Bardi & Kyriakides (2006a).

Initial wrinkling of those tubes as obtained from a bifurcation analysis conducted with the present numerical tools. The numerical results are compared with experimental results and analytical solutions. More specifically, the bifurcation load at first wrinkling and the corresponding wavelength can be calculated analytically using equations (6.2) and (6.3).

$$\sigma_{cr} = \left[\frac{C_{11}C_{22} - C_{12}^2}{3} \right]^{1/2} \left(\frac{t_s}{R} \right) \tag{6.2}$$

$$L_{hw} = \pi \left[\frac{C_{11}^2}{12\left(C_{11}C_{22} - C_{12}^2\right)} \right]^{1/4} \left(Rt_s \right)^{1/2} \tag{6.3}$$

where R and t_s are the radius and wall thickness of the tube and $C_{a\beta}$ are the instantaneous material moduli according to J_2 - deformation plasticity theory, at the bifurcation stage. Expressions for moduli $C_{a\beta}$, for both associative and non-assocative J_2 - plasticity, can be found in Bardi and Kyriakides (2006). It should be noted that first wrinkling of those thick-walled cylinders in the plastic range is always axisymmetric (Figure 6 - 4) as shown analytically by Gellin (1979).

The analytical and numerical predictions for the critical stress and strain are plotted against D/t_s in Figure 6 - 2 and Figure 6 - 3, respectively, together with experimental results reported in Bardi *et al.* (2006b). In this figure, ○ and ● refer to the upper and lower bound of first wrinkling observed in tests (Bardi and Kyriakides, 2006a) respectively. In the same graph, the corresponding analytical and numerical predictions using J_2 - flow (associative) and the present (non-associative) theory both analytically and numerically are also shown. Note

that the numerical predictions of J_2 - flow theory have been obtained from the present finite element technique and the constitutive equations for the associative flow rule; these equations are obtained from the flow rule (2.10) omitting the second term on the right-hand-side. The analytical predictions are obtained from equation (6.2) using the appropriate instantaneous moduli $C_{a\beta}$ for the associative and non-associative case. The comparison with experimental data shows the superiority of the non-associative flow model with respect to the associative flow model in predicting bifurcation in the plastic range. Furthermore, a very good comparison of the present numerical model and the corresponding analytical results from equation (6.2) is shown. The axisymmetric buckling shape is shown in Figure 6 - 4.

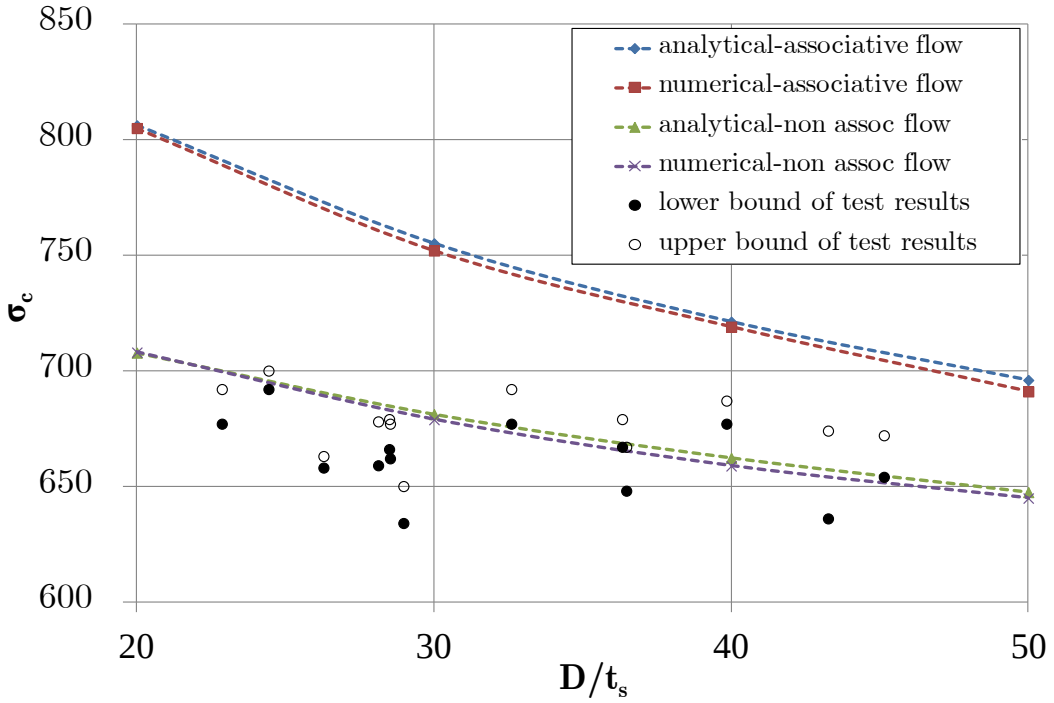

Figure 6 - 2: Critical stress (onset of wrinkling) with respect to specimen D/t_s ratio, analytical predictions refers to equation (6.2)

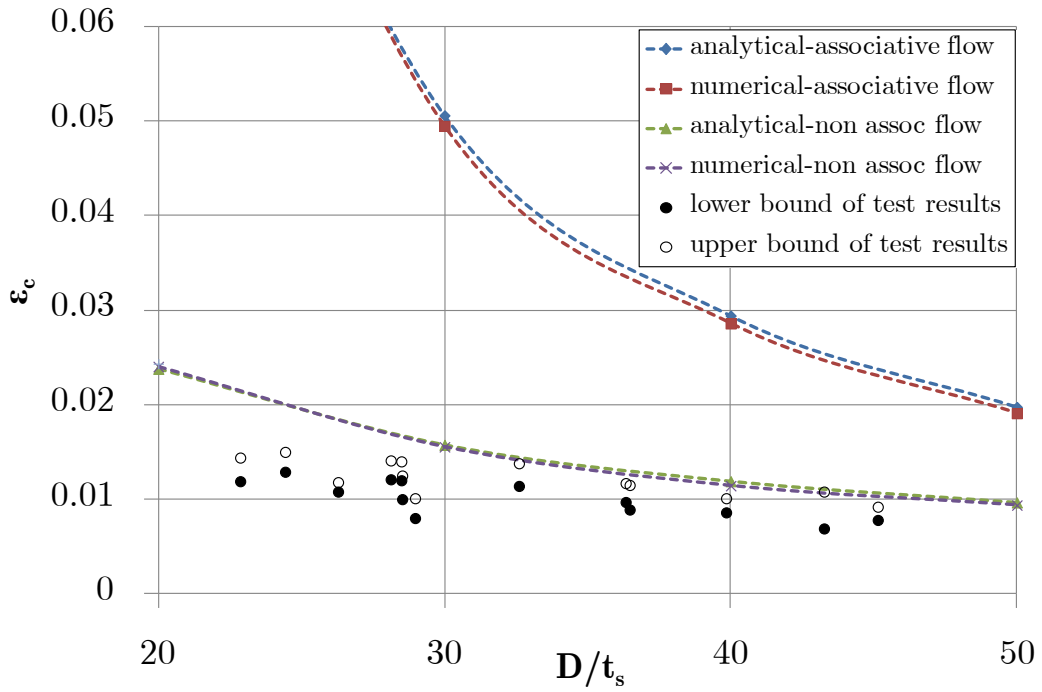

Figure 6 - 3: Critical strain (onset of wrinkling) with respect to specimen D/t_s ratio

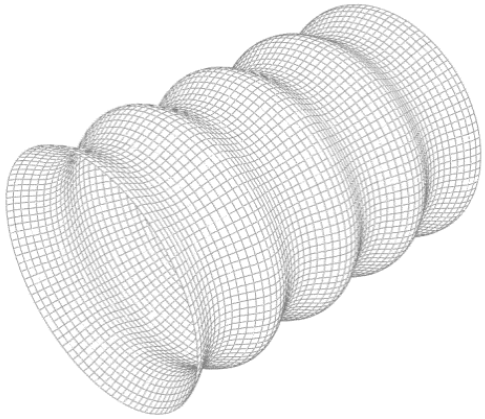

Figure 6 - 4: Bifurcation (first wrinkling) shape of axially loaded stainless steel cylinder (D/t_s =26.3).

Following the above bifurcation analysis, a nonlinear analysis is performed that follows the gradual development of wrinkles under increasing axial compression. Thick-walled cylinders subjected to axial compression, exhibit

limit load instability (occurrence of maximum load on the load-displacement curve), followed by the development of localized buckling patterns. To describe this process, an initially axisymmetrically wrinkled pattern is assumed and gradual development and localization of this wrinkling pattern is monitored. Towards this purpose, a thick-walled cylinder $\left(D/t_s = 26.3\right)$, with the same material is considered, using a tube segment of length equal to seven half-wavelengths. Each half-wavelength corresponds to the first buckling shape of Figure 6 - 4, and an initial wave-type imperfection is imposed with a small amplitude $\omega_{0,max}$ equal to 0.1% of thickness. The half-wave length L_{hw} has been determined from the bifurcation analysis described above, equal to 14.515 *mm*. The load-displacement equilibrium path is shown in Figure 6 - 5a. Considering a small bias in the amplitude of one wrinkle (as initial imperfection), the analysis leads to a maximum load due to wrinkle localization denoted as limit state as shown in Figure 6 - 5a, where the numerical analysis the experimental curve are compared. The comparison between the non-associative model and tests results is very good in terms of the maximum load, the corresponding deformation and the initial post buckling behavior. It is noted that the limit (maximum) load occurs at a value of imposed displacement δ/L equal to 4.5%, which is well beyond the strain at which first wrinkles occur in the perfect cylinder (1.8%), shown in Figure 6 - 5b. This means that first bifurcation may not be related to the ultimate axial compression capacity of the cylinder, as noted by Bardi and Kyriakides (2006). Figure 6 - 5b shows the buckled configuration of the

cylindrical shell and the localization of wrinkling deformation at a value of imposed displacement δ/L equal 5%. In Figure 6 - 5c the evolution of radial displacement along a cylinder generator is shown, illustrating the non-uniform growth of wrinkle amplitude; the central ripple grows significantly more than the others, resulting in localization of wrinkled pattern and loss of structural strength. Finally, in Figure 6 - 5a, the numerical results using the classical J_2 - flow theory are also shown. The comparison is satisfactory up to a certain level, but this associative model does not predict accurately the ultimate load deformation and the initial post buckling behavior.

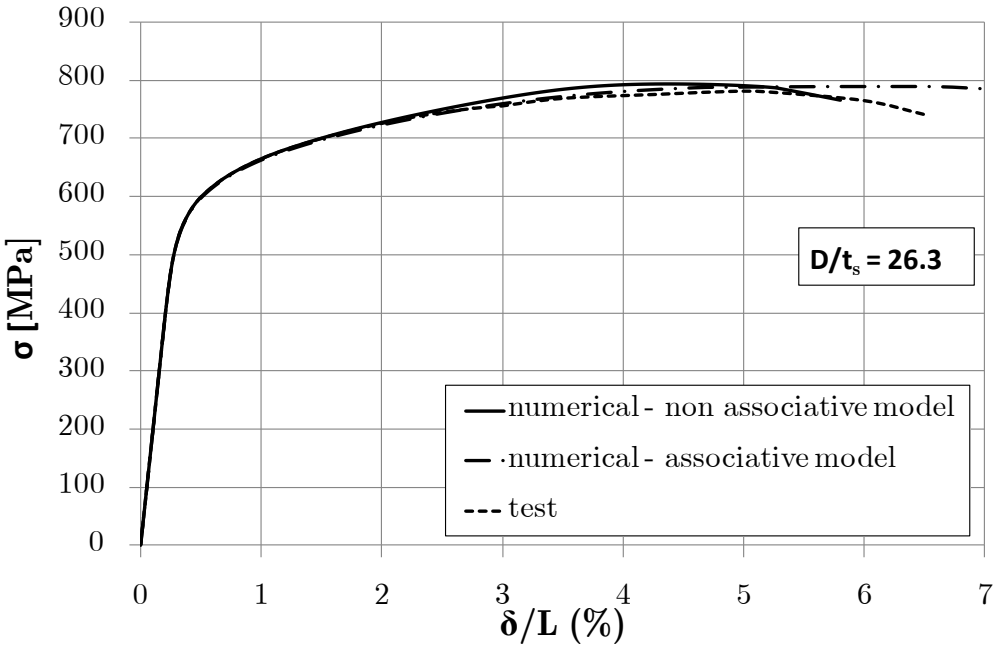

(a)

(b)

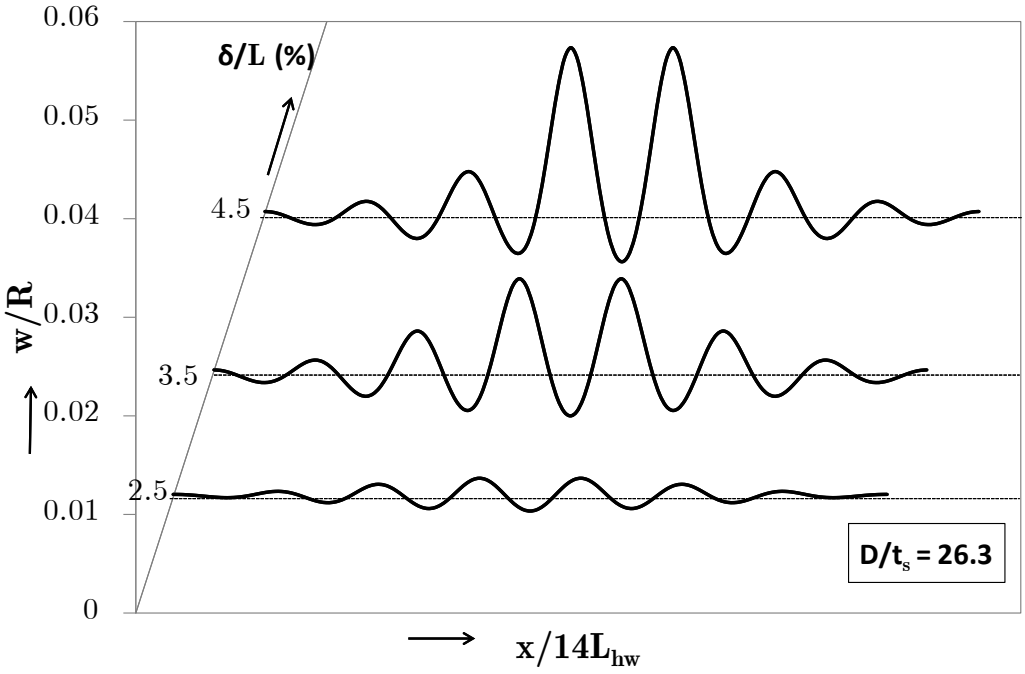

(c)

Figure 6 - 5: (a) Stress-displacement response, comparison with the test result reported in Bardi & Kyriakides (2006); (b) Deformed configuration of axially loaded cylinder with localized wrinkling corresponding to δ/L value of 5%; (c) evolution of radial displacement along a cylinder generator with increasing axial compression for specimen with $D/t_s = 26.3$ and yield stress $\bar{\sigma} = 572\ MPa$.

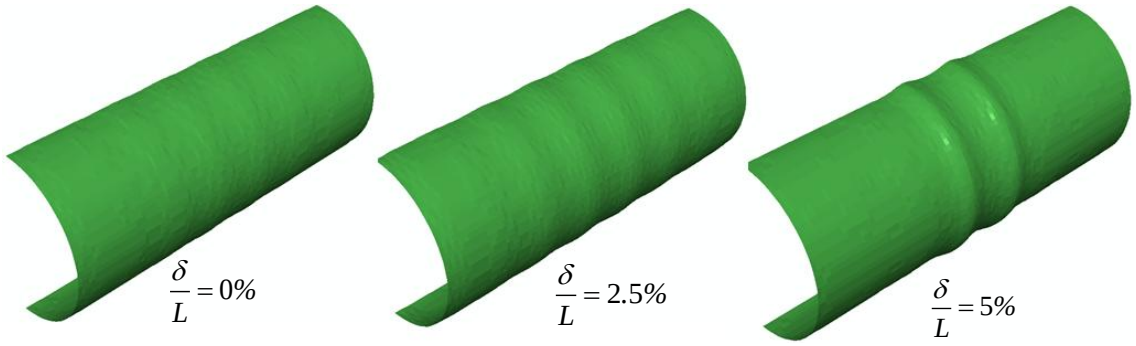

Figure 6 - 6: Reproduction of a deformed configuration of the shell at different values of displacement for specimen with $D/t_s = 26.3$ *and yield stress* $\bar{\sigma} = 572\ MPa$ *.*

6.2 Imperfection sensitivity of cylindrical shells in the inelastic range

The buckling performance of imperfect thick-walled cylinders subjected to axial (meridional) compression has been examined analytically by Gellin (1979). Gellin enhanced the methodology initially proposed by Koiter (1963) for elastic thin-walled cylinders, employing shell kinematics based on DMV shell theory, and elastic-plastic material behavior through J_2 - deformation theory.

Comparison is conducted for a thick-walled cylindrical shell with D/t_s equal to 51. The material behavior can be described by equation (6.2), with E, $\bar{\sigma}$ and n equal to 194 *GPa*, 572 *MPa* and 5 respectively, so that the ratio of the effective yield stress $\bar{\sigma}$ to the classical buckling stress of the elastic shell $\bar{\sigma}/\sigma_c^e$ is 0.5 (σ_c^e is defined equal to $Et_s/\sqrt{3(1-\nu^2)}R$). The analysis assumes an initial imperfection in the form of first axisymmetric buckling mode (see Figure 6 - 7) obtained by a bifurcation analysis, as described above.

Considering a tube segment of length equal to twice the value of half-

wavelength $\left(L = 2L_{hw}\right)$, and the axisymmetric initial imperfection, secondary bifurcation to a non-axisymmetric mode is calculated. The results of the numerical calculations are presented in Figure 6 - 7, where the bifurcation load of the imperfect shell P_{cr} is normalized by the bifurcation load of the perfect shell $P_{cr,0}$ and plotted in terms of the imperfection amplitude $\omega_{0,max}$ showing a very good comparison with Gellin's results.

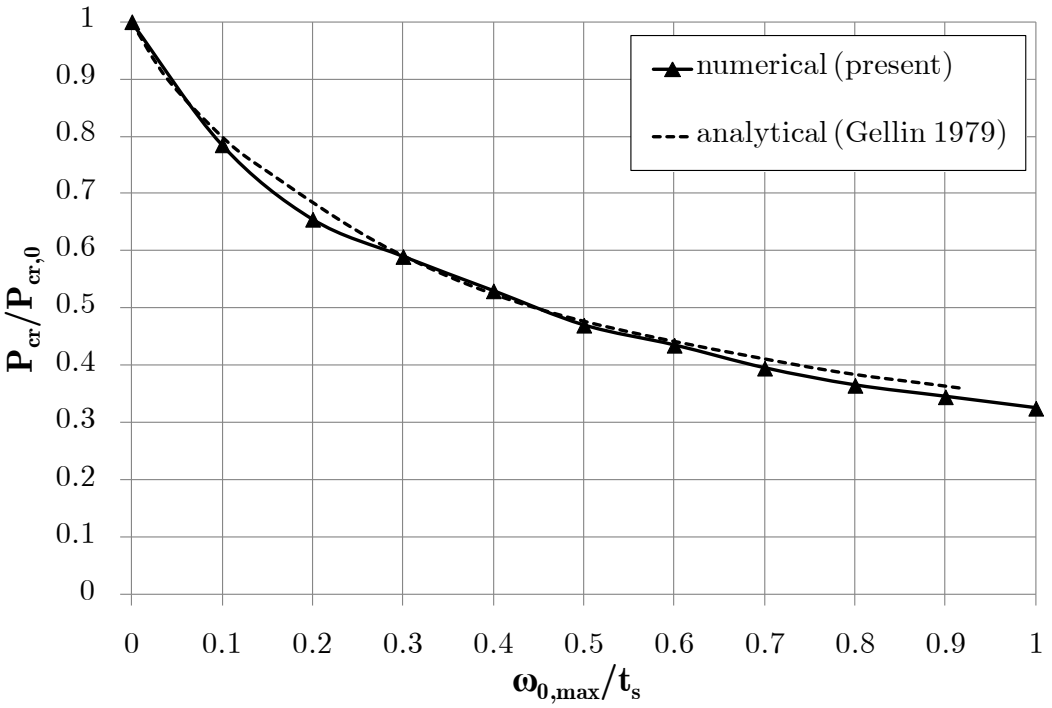

Figure 6 - 7: Imperfection sensitivity in the plastic range for a metal cylinder with $D/t_s = 51$ *and yield stress* $\bar{\sigma} = 572\ MPa$.

6.3 Bending buckling of elongated metal cylindrical shells

Elongated metal cylindrical shells, used in pipeline and piping applications, are often subjected to longitudinal bending. Of particular interest in those applications is the response of such shells, bent into the inelastic range and the

various instabilities which result in their structural failure. Brazier (1927), in a pioneering publication, has demonstrated analytically that bending of relatively thin-walled circular elastic tubes induces ovalization to the tube cross-section. The growth of ovalization causes a progressive reduction in the bending stiffness of the shell, leading to a maximum value of moment, referred to as "limit moment" or "ovalization moment". With increasing bending beyond this "limit point", a drop in moment occurs. In practical applications, this limit moment instability is often preceded by shell bifurcation-type instabilities characterized by short-length axial waves, as demonstrated in recent numerical works [Karamanos and Houliara (2006, 2010)].

In the case of thicker cylindrical shells ($D/t_s < 100$), the response and the ensuing instabilities, are strongly influenced by both cross-sectional ovalization and the plastic behavior of the metal material. Experimental works, together with semi-analytical solutions have demonstrated that although the ovalization imposed on the shell cross-section is relatively small for shells bent into the plastic range, it still leads to the development of a limit moment. Nevertheless, in addition to limit load instability, the shell exhibits various shell-type buckling modes in the form of uniform wrinkles along the compression side of the bent tube. Under increasing bending, localization of wrinkled patterns or secondary buckling into a non-uniform wrinkling pattern has been observed in several experiments.

The above structural behavior is simulated numerically, using the numerical

tools described in the present work. The tube is made of aluminum (AL 6061-T6), diameter and thickness are equal to 31.75 *mm* (1.25 *in*) and 0.889 *mm* (0.035 *in*) respectively, $D/t_s = 35.7$ and has been tested experimentally (Kyriakides and Ju, 1992). Material behavior is described by a Ramber-Osgood of stress-strain curve equation (6.1), with E, $\bar{\sigma}$ and n equal to 67.36 *GPa*, 282 *MPa* and 28 respectively, corresponding to a yield stress of 283.4 *MPa* .

At first, wrinkling on the ovalization bending prebuckling state is determined, and the corresponding half-wavelength is computed (L_{hw}). A sequence of analyses is performed to determine the half-wavelength (Figure 6 - 8). The moment is normalized by the fully-plastic moment ($M_0 = \sigma_Y t_s D^2$) and the curvature is normalized by the value of characteristic value $\kappa_I = t_s / D^2$.

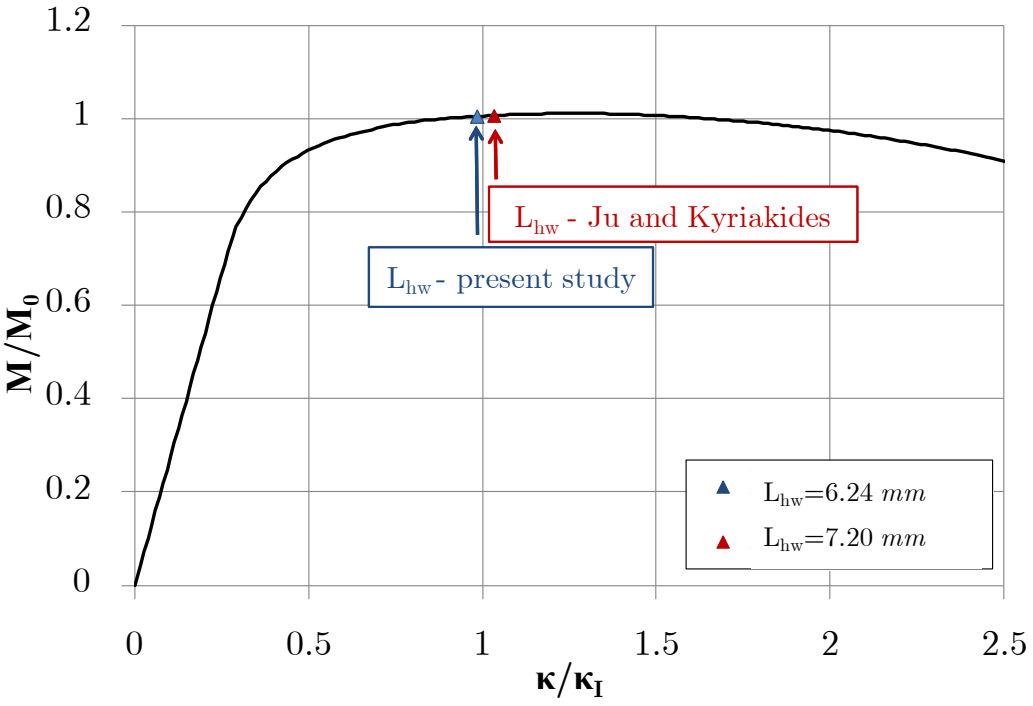

Figure 6 - 8: Comparison of results for the half-wavelength (Kyriakides and Ju, 1992) with present numerical predictions.

The structural response of thick cylindrical shells and the ensuing instabilities are strongly influenced by the plastic behavior of the metal material, as well as by the ovalization of the cross-section, implying a highly nonlinear prebuckling state. Along this nonlinear path, the shell exhibits various shell-type buckling modes in the form of wrinkles along its compression side. First bifurcation occurs in a uniform wrinkling pattern shown in Figure 6 - 9, denoted by the first arrow (↑) on the primary path. Subsequently a secondary bifurcation on the prebuckling path is also detected, in the form shown in Figure 6 - 9 denoted by the second arrow (↑). Figure 6 - 9 shows the predicted ovalization-curvature response for the shell.

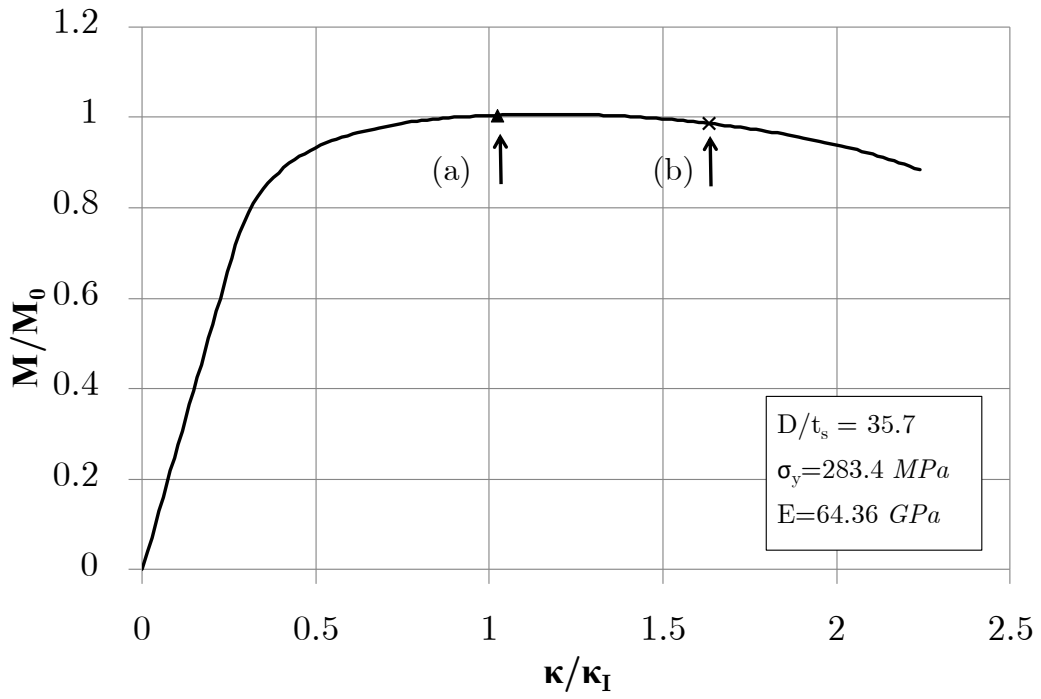

Figure 6 - 9: Moment-curvature diagram of alumium tube with $D/t_s = 35.7$ *and* $\sigma_y = 283.4\ MPa$ *from ovalization analysis; first and secondary bifurcation occurs in (a) and(b), respectively.*

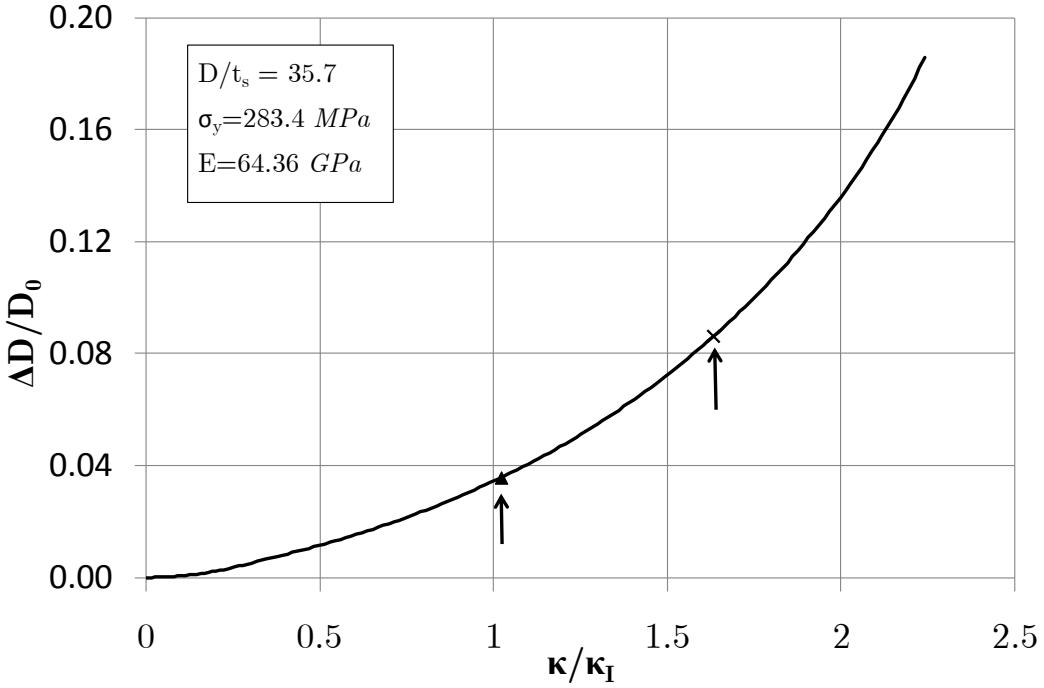

Figure 6 - 10: Ovalization-curvature diagram of aluminium tube with $D/t_s = 35.7$ *and* $\sigma_y = 283.4\ MPa$ *from ovalization analysis.*

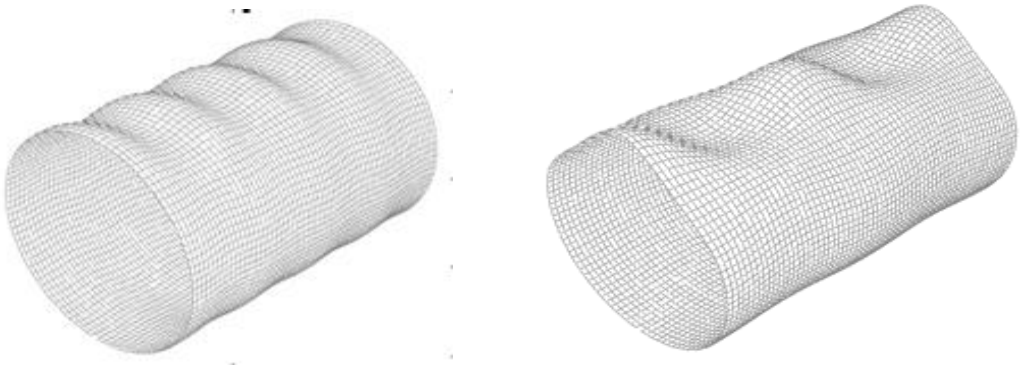

(a) (b)

Figure 6 - 11: Bifurcation shapes of bending loaded aluminium tube with $D/t_s = 35.7$*, (a)* 1^{st} *buckling mode(uniform wrinkling).and (b)* 2^{nd} *buckling mode.*

The post-buckling behavior of the shell can be analyzed by allowing for deformations which vary along the length of the shell. A shell with initial geometric imperfections is considered. The imperfection is in the shape of the critical buckling mode obtained from the bifurcation analysis presented above. The results of the effect of imperfections with amplitudes $\omega_{0,i}$ =0.15% and 0.45% are shown in Figure 6 - 12 using tube segment of length equal to $2L_{hw}$. The main influence of the imperfections on the calculated responses is seen to occur once the shell enters the plastic range of the material. Due to the imperfections, the shell becomes more compliant and the limit load instability occurs at a smaller curvature than that of the perfect shell. The limit point indicated by (↑) on the response, and the secondary bifurcation on the primary path is calculated indicated by (**X**).

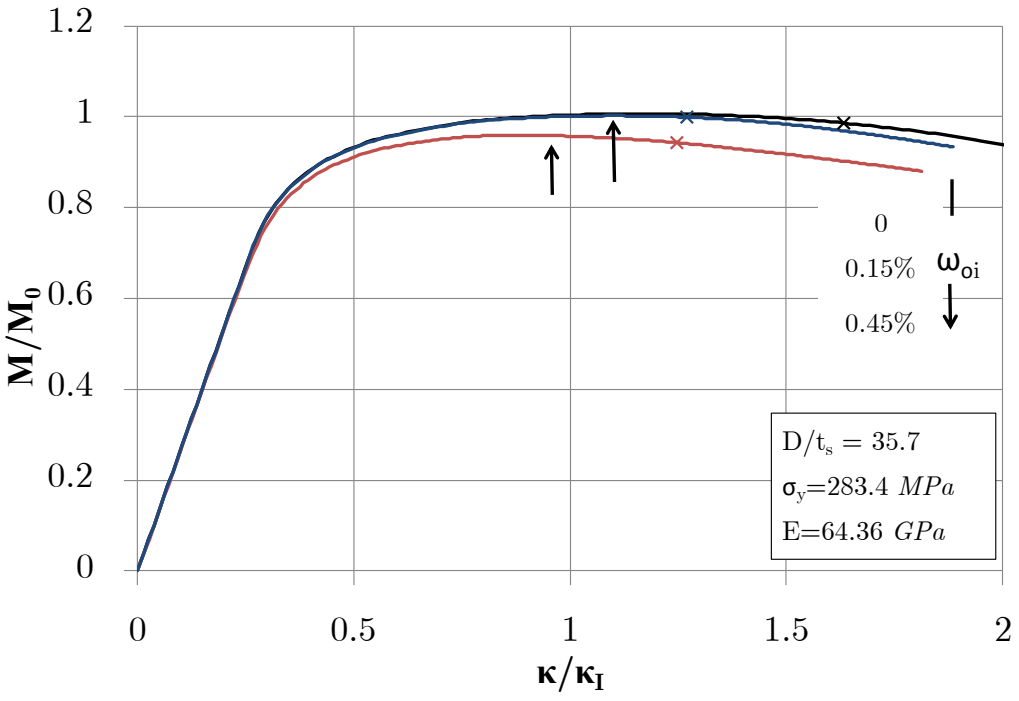

Figure 6 - 12: Moment-curvature diagram of tube with $D/t_s = 35.7$.

From the results presented so far, it has been demonstrated that at some curvature the shell develops uniform wrinkles. As the result, the overall stiffness of the shell is reduced and the limit load develops. It has been shown that structures which exhibit such behavior tend to develop localized buckling soon after the limit load. The possibility of this occurring will be checked by considering a section of the shell containing a number of wrinkles $\left(L = 7L_{hw}\right)$. A small imperfection is included which provides a small bias to the amplitude of the one of the wrinkles. For the shell with $D/t_s = 35.7$ the wrinkles were found to localize. The effect of localization on the response is shown in Figure 6 - 13, where the uniform wrinkle analysis and the localized wrinkle analysis are compared. Results for $\varpi_{0,i}$=0.15% and 0.45% are shown in Figure 6 - 15, respectively, with ϖ_i kept constant and equal to 0.015% of thickness.

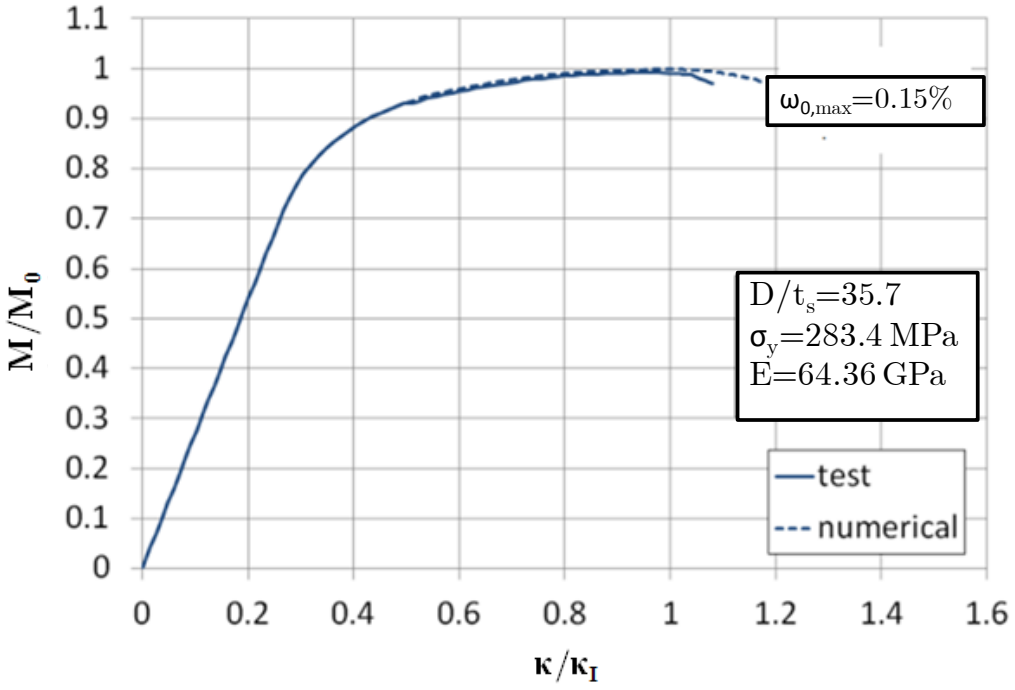

Figure 6 - 13: Comparison of test results (Kyriakides and Ju, 1992) with present numerical predictions.

The progressive development of localized deformations in the shell is illustrated in Figure 6 - 14, which shows the ovalization predicted along the length of the shell analyzed at different value of curvature.

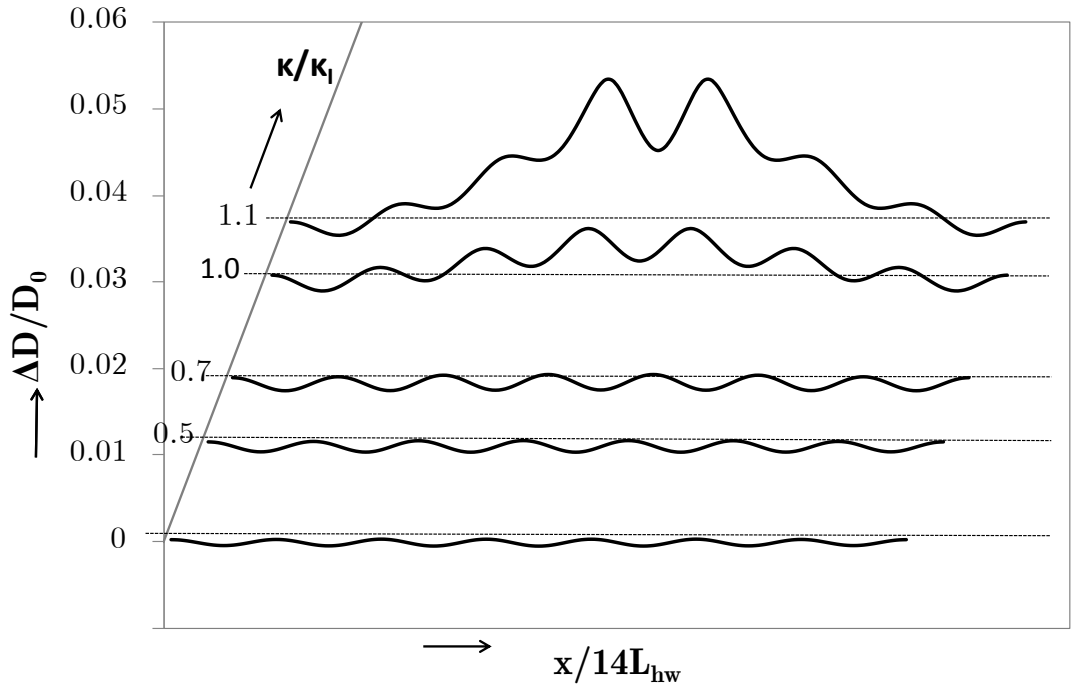

Figure 6 - 14: Ovalization along length of the shell at different value of curvature.

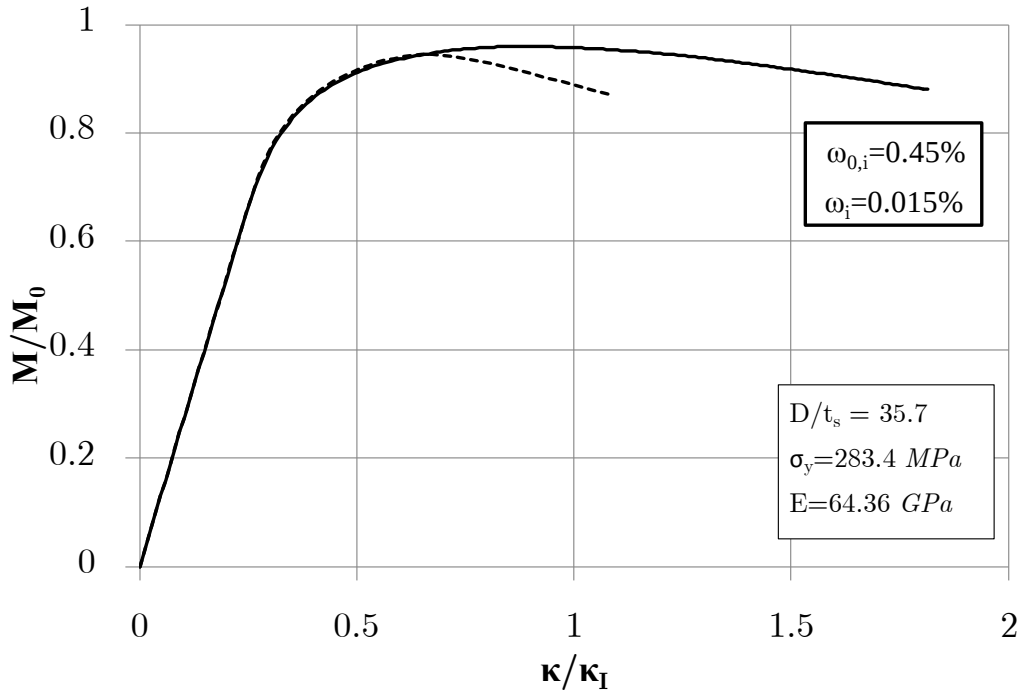

Figure 6 - 15: Comparison of predictions of uniform wrinkle and localized wrinkle analysis.

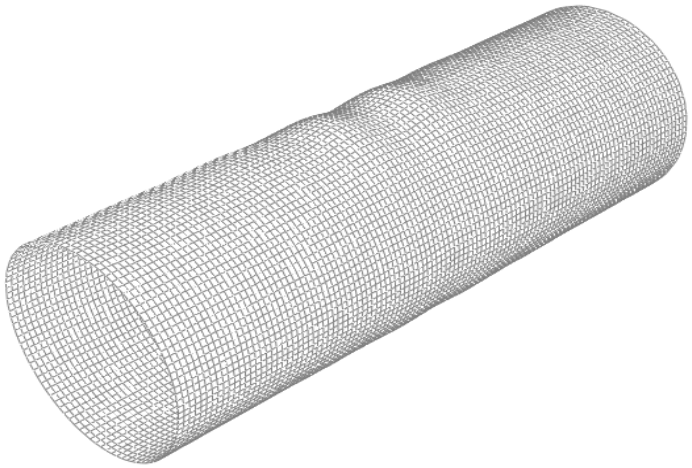

Figure 6 - 16: Deformed configuration of a bent shell with localized wrinkling $\left(D/t_s = 35.7\right)$.

The wrinkles are seen to grow uniformly up to the limit load, beyond which the central part of the shell ovalizes faster than the other parts. Figure 6 - 16 shows the deformed configuration of the shell analyzed, which illustrates the non-uniform growth of the amplitude of the wrinkles. The central wrinkle is grown significantly more the others.

A shell with initial geometric imperfections is considered next. The imperfections are related to the second buckling mode obtained from the bifurcation analysis presented above. The effect of using the shape of the second bifurcation as initial imperfection with different amplitudes is shown in Figure 6 - 17.

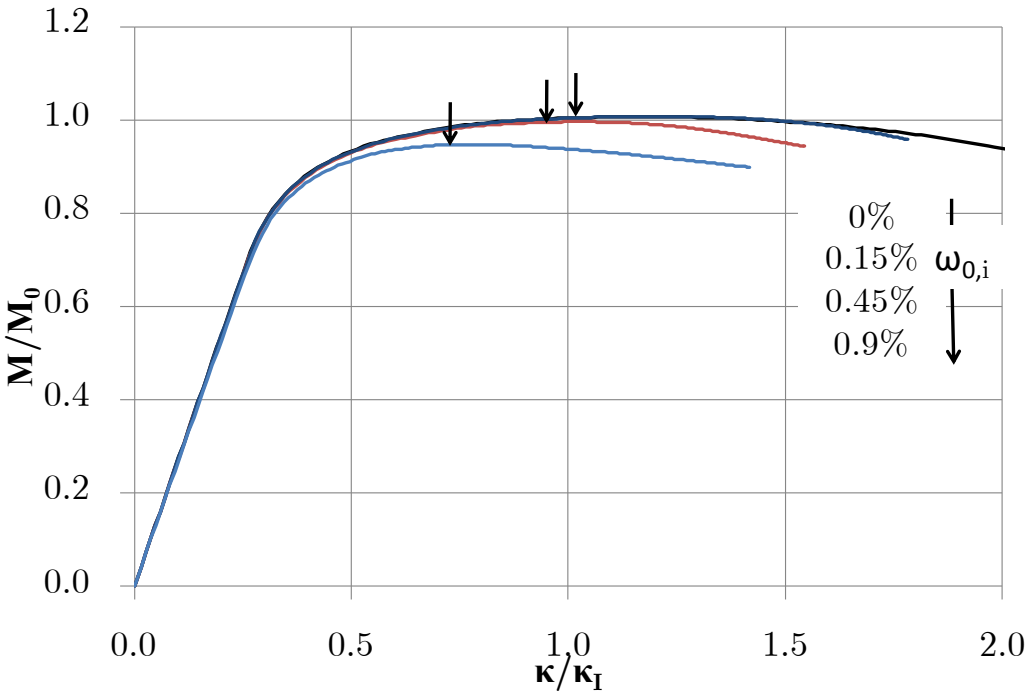

Figure 6 - 17: Moment-curvature diagram of tube with initial imperfection the shape of the second bifurcation

The results show that even very small initial wrinkles of the cylinder wall may have significant effects on the structural response of the cylindrical member under bending loading.

Chapter 7

Steel Tubular Members under Axial Compression and Bending

The numerical formulation developed in the previous chapter is employed for the analysis of high-strength steel circular hollow section tubes. These tubular members are basically thick-walled cylindrical shells that buckle in the plastic range.

7.1 Introduction

High-strength steel circular hollow section (CHS) tubes are becoming popular in a variety of structural engineering applications, such as tubular columns of building systems or members of tubular lattice structures. The principal characteristic of these steel products, with respect to CHS tubes of normal steel grades, is the elevated yield stress value, which implies increased ultimate capacity, resulting in a good relationship between weight and strength. They can also be efficient in cases where space occupancy becomes a critical design criterion.

According to current design practice, the ultimate capacity of steel CHS

members under axial compression and bending loads depends primarily on whether the section is classified as “compact” or “non-compact”, i.e. on the ability of the cross-section to sustain significant inelastic deformation before failure in the form of local buckling. The provisions of EN 1993-1-1 standard specify four (4) cross-sectional classes. More specifically, Class 4 corresponds to thin-walled sections, which are able to sustain compression due to axial/bending load only in the elastic range. On the other hand, Class 1 comprises thick-walled sections that are able to deform well into the plastic regime, without exhibiting local buckling, whereas Classes 2 and 3 refer to intermediate type of structural behavior. For the case of CHS tubular members, classification in EN 1993-1-1 is based on the value of the diameter-to-thickness ratio, as well as on the value of the material yield stress, as shown in the second column of Table 7 - 1. The same classification is also adopted by the CIDECT guidelines (Rondal *et al.*, 1996) for hollow section stability, whereas similar provisions for cross-sectional classification on CHS members can be found in other specifications (e.g. AISC, API RP2A – LRFD).

The above classification provisions have been initially developed for the case of high-strength steel CHS tubular members with $\sigma_Y \leq 460\ MPa$. Within the EN 1993 steel design framework, a new standard has been issued recently (EN 1993-1-12) to specify the applicability of the other EN 1993-1-xx standards in high-strength steel applications. According to EN 1993-1-12, the EN 1993-1-1 classification provisions, shown in Table 7 - 1, may be applied for high-strength

steel members as well. However, the existing classification for CHS tubular members appears to be rather conservative for high-strength steel tubular members; as an example one can readily obtain from Table 1 that CHS sections with $D/t_s = 35$ and $\sigma_Y = 690\ MPa$, are classified as Class 4 sections, which implies a low ultimate capacity, within the elastic range. On the other hand, such a section subjected to bending is expected to exhibit significant inelastic deformation before local buckling.

The key issue in the above classification of CHS members is their cross-sectional strength, mainly in terms of local buckling, which constitutes a shell-buckling problem in the inelastic range. Inelastic buckling of relatively thick-walled steel cylinders under compressive loads has been the issue of significant research. Early experimental observations (Lee 1962; Batterman, 1965) as well as the results of the previous chapter have shown that under pure axial compression or bending, thick-walled cylinders – in contrast with thin-walled ones – do not fail abruptly, but one can observe significant wall wrinkling before an ultimate load occurs. Analytically, a main challenge for solving this problem has been the combination of structural stability principles with inelastic multi-axial material behavior. In particular, it has been recognized that buckling predictions depend on the choice of plasticity theory (Gelin 1979; Tvergaard 1983), and for a thorough presentation of metal cylinder buckling behavior under uniform axial compression, the reader is referred to the recent papers by Bardi & Kyriakides (2006) and Bardi *et al.* (2006).

In addition to uniform axial compression, bending buckling of tubular members has also received significant attention, motivated mainly by their use in pipeline applications. Experimental works indicated that failure of thick-walled tubes under bending is associated with tube wall wrinkling, has several similarities with the case of uniform axial compression, but is characterized by a nonlinear prebuckling state – due to cross-sectional ovalization – and a more localized buckling pattern on the compression side of the cylinder. The reader is also referred to the papers by Ju & Kyriakides (1992) and Karamanos & Tassoulas (1996), where semi-analytical and numerical tools have been developed respectively for simulating the formation of local buckling due to bending. These works have shown that the adoption of a non-associative corner-like plasticity theory may provide the most accurate results with respect to experimental data.

The present chapter aims at employing the non-associative model in order to examine the cross-sectional classification of high-strength steel CHS seamless tubular members. The investigation described in the present chapter is numerical, based on the special-purpose finite element formulation, presented in previous chapters, and is aimed at determining the maximum load at which failure occurs, either because of bifurcation to a wavy pattern or due to localization of deformation. It has been part of an extensive European research program, ATTEL, on the structural behavior of high-strength steel tubular members (Jaspart *et. al.*, 2012). These high-strength steel tubes have also been

considered by Pournara *et al.* (2012) in terms of their structural beam-column behavior. In that work the need for a more reliable classification of high-strength steel CHS sections has been addressed.

The seamless tubes under consideration have yield stress equal or higher than 590 *MPa*, and diameter-to-thickness ratio ranging between 20 and 60, which are typical for structural applications. Initial imperfections and residual stresses from real measurements are taken into account in the present analysis. The numerical results are presented in the form of diagrams, which show the cylinder strength and deformation capacity (axial and bending) in terms of cylinder slenderness, and are aimed towards evaluating the applicability of existing classification rules in EN 1993-1-1 for high-strength steel CHS tubes.

Table 7 - 1: Classification in EN 1993-1-1, based on the value of the diameter-to-thickness ratio

Class	**Class limits**	**Class limits in terms of shell slenderness λ ***
1	$D/t_s \le 50\varepsilon^2$	$\lambda \le \lambda_1 = 0.278$
2	$50\varepsilon^2 \le D/t_s \le 70\varepsilon^2$	$\lambda_1 = 0.278 < \lambda \le \lambda_2 = 0.329$
3	$70\varepsilon^2 \le D/t_s \le 90\varepsilon^2$	$\lambda_2 = 0.329 < \lambda \le \lambda_3 = 0.373$
4	$D/t_s \ge 90\varepsilon^2$	$\lambda > \lambda_3 = 0.373$

* λ is the "shell slenderness" and defined as $\lambda = \sqrt{\sigma_Y/\sigma_e}$, where $\sigma_e = 0.605 EC_x t/R$ is the elastic buckling stress, and the value of C_x is taken equal to 0.6 (Appendix IV)

7.2 Material characterization and imperfection measurements

Results are obtained for 355.6-*mm*-diameter (14-inch) high-strength-steel tubes with thickness ranging between 6.4 *mm* and 16 *mm* covering a wide range of structural CHS sections. Two materials with yield stress equal to 590 *MPa* and 735 *MPa* are used, with nearly constant hardening modulus equal to $E/40$ (Pournara *et al.* 2012), as shown in the nominal stress – engineering strain curve of the high-strength steel material $(\sigma_Y = 735\ MPa)$ in Figure 7 - 1. The elongations limit corresponding to maximum nominal stress 8%.

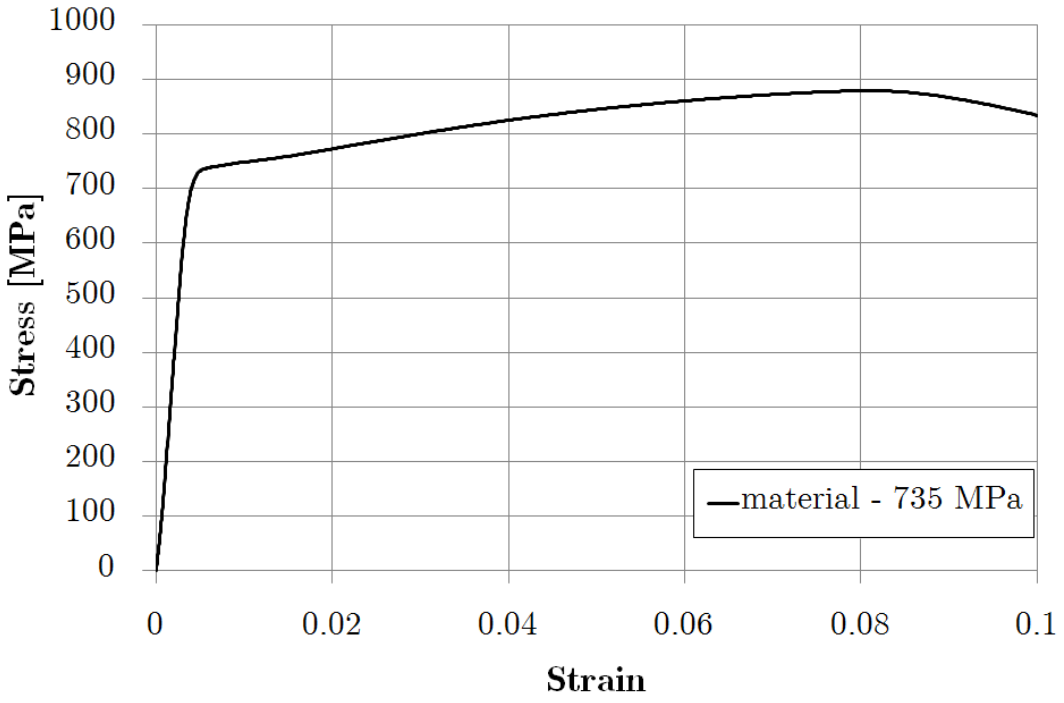

Figure 7 - 1: Nominal stress – engineering strain curve of the high-strength steel material.

The finite element model is capable of including the effects of initial imperfections, by prescribing the configuration of the shell surface in the initial (reference) stage. In the present analysis, the initial imperfection is assumed in a wavy form, similar to the buckling shape obtained from the bifurcation analysis on the pre-buckling equilibrium path. In addition to initial imperfections, the finite element model accounts for the presence of residual stresses, which may have a significant effect on the buckling load. The amplitudes of initial imperfections and residual stresses are obtained from measurements conducted by Centro Sviluppo Materiali SpA on the tubes under considerations in the course of the ATTEL project.

Initial wrinkling measurements have been obtained using an ultrasonic device. Tube wall coordinates were measured at every 10 mm along 8 equally-spaced generators, for a pipe length of equal to about two tube diameters. Typical results from those measurements are shown in Figure 7 - 2(a) for three typical generators.

These measurements along the generators have been processed to estimate initial wrinkling, as well as cross-sectional distortions (*i.e.* out-of-roundness imperfections) at specific cross sections along the tube.

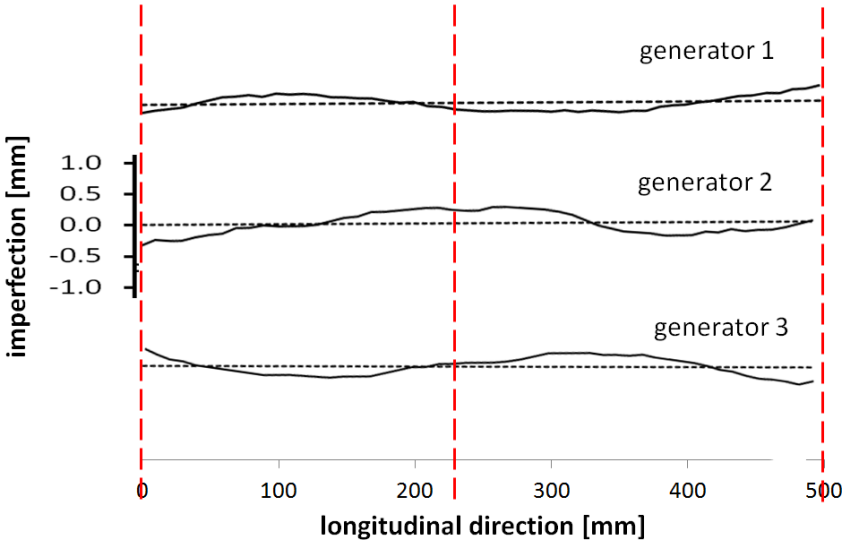

(a)

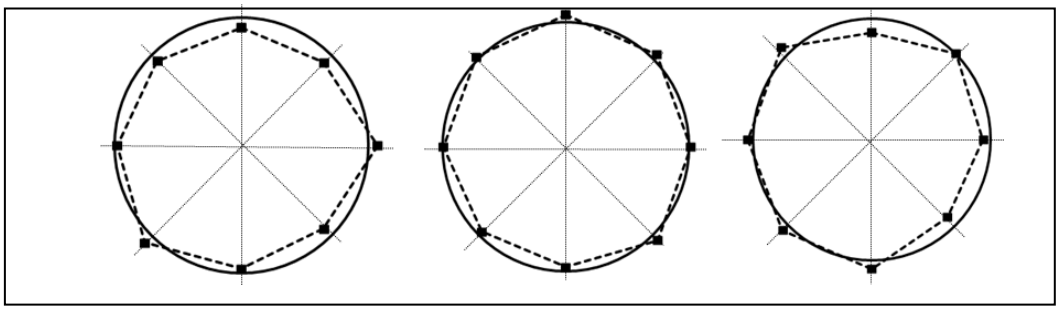

(b)

Figure 7 - 2: Typical data from (a) measurement of generator geometry (b) out-of-roundness of three cross-sections.

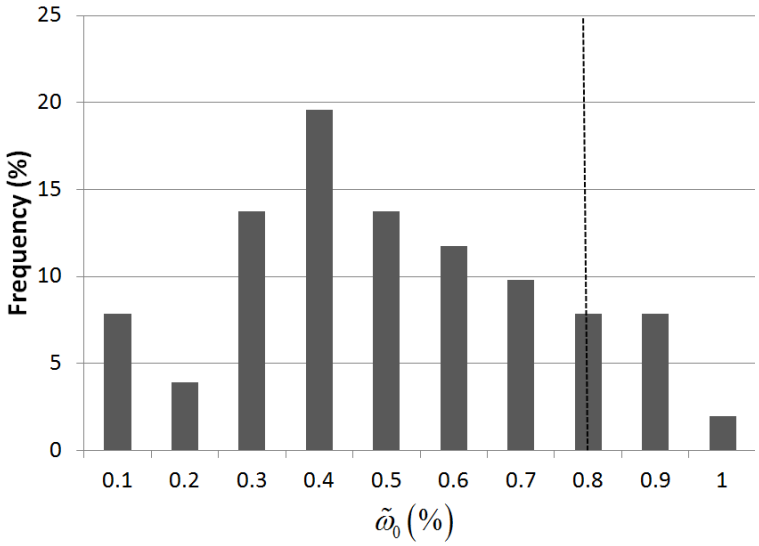

Figure 7 - 3: Statistical evaluation of $\tilde{\omega}_0$, the measured absolute-value amplitude of the axisymmetric imperfection.

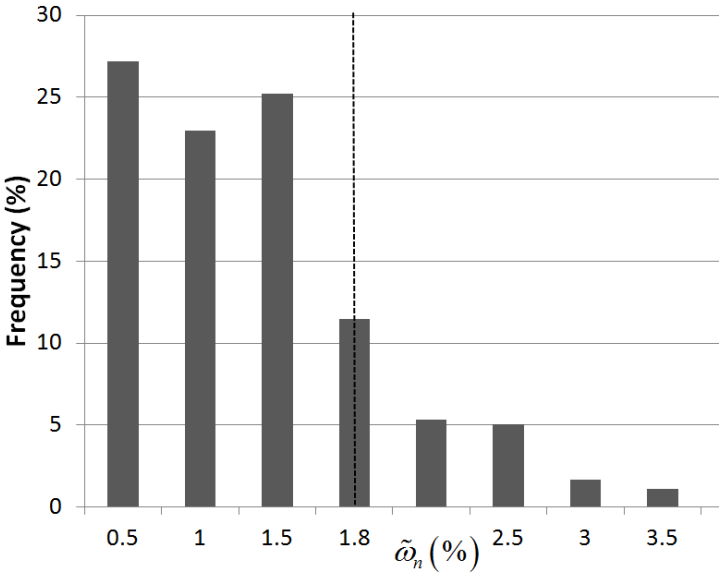

Figure 7 - 4: Statistical evaluation of $\tilde{\omega}_n$, the measured absolute-value amplitude of the non-axisymmetric imperfection.

It is assumed that the deviation of every cross-section from the perfect round shape is the superposition of an "extensional" component, which is uniform around the cross-section, and can be considered as axisymmetric initial imperfection associated with pure “bulging” or “shrinking”, and a non-uniform component which corresponds to cross-sectional out-of-roundness (distortion) as shown in Figure 7 - 2(b). In Figure 7 - 3 and Figure 7 - 4, $\tilde{\omega}_0$ and $\tilde{\omega}_n$ represent the measured amplitudes of the axisymmetric and the non-uniform imperfection components respectively, with respect to tube thickness. A statistical evaluation of $\tilde{\omega}_0$ and $\tilde{\omega}_n$ is offered in those Figures; the values of $\tilde{\omega}_0$=0.8% and $\tilde{\omega}_n$=*1.8%* correspond to an 80% upper limit of the measurements, and are considered as representative initial imperfection values to for the parametric study described in the next section.

Residual stress measurements have also been performed in both the axial and the circumferential hoop direction (Pournara *et al.* 2012). The measurements in the hoop direction have been obtained through the “splitting ring” method, as specified in ASTM E1928-99, and resulted in an opening deformation (gap) of 17.7 *mm*, corresponding to a maximum hoop stress of 122 *MPa* (about 16% of the actual yield stress). Furthermore, to estimate the residual stresses in the axial direction, longitudinal strips have been obtained from the tubes, and their curvature has been measured, corresponding to a maximum stress of 26 *MPa*, which is only 4% of the yield stress. The values of residual stresses in the axial direction are very low, due to the fact that the tubes under examination are

seamless, and therefore, they can be neglected.

7.3 Analysis Methodology

7.3.1 Methodology for axial loading

Infinitely long cylindrical shells with axisymmetric and non-axisymmetric initial imperfections are analyzed under axial compression loading by appropriate implementation of the ‘‘tube-element’’. Non-axisymmetric modes and bifurcations along the equilibrium path are identified. Experimental observations as well as numerical results have shown that first wrinkling in the plastic range is axisymmetric. First, the corresponding bifurcation load and wavelength can be calculated analytically using equations (6.2) and (6.3), and have shown to be very close to the numerical results.

The present analysis follows the steps described in Chapter 6.1. Assuming a half-wave length from equation (6.3), axisymmetric wrinkling on the prebuckling state for the uniformly-compressed cylinder is determined. Then, considering a tube segment of length equal to twice the value of half-wavelength $L = 2L_{hw}$, and an axisymmetric initial imperfection, secondary bifurcation to a non-axisymmetric mode is calculated. In this analysis, the axisymmetric imperfection amplitude ω_0 is 0.8%, as indicated by the corresponding measurements.

Subsequently, two possible limit states are examined. First, localization of the axisymmetric wrinkling pattern is examined, using a tube segment of length

equal to several half-wavelengths. Considering a small bias in the amplitude of one wrinkle, the analysis leads to a maximum load N_1 due to wrinkle localization denoted as limit state (a). In addition, a tube segment of length equal to two half-wavelengths is analyzed with a combination of axisymmetric and non-axisymmetric imperfections, with relative amplitudes ω_0 and ω_n equal to 0.8% and 1.8% respectively, so that a maximum load N_n is obtained. This limit state is denoted as limit state (b). The smallest value of N_1 and N_n determines the ultimate axial load (strength) of the cross-section N_u. The axial shorting δ_u corresponding load N_u is also calculated.

7.3.2 Methodology for bending loading

The second part of this study concerns the prediction of ultimate capacity under bending loading, following the analysis steps described by Ju&Kyriakides (1992). The analysis is similar to the one in axial loading described above. At first, wrinkling on the ovalized bending prebuckling state is determined, and the corresponding half-wavelength is computed L_{hw}. Then, using an initial imperfection on a tube segment of length equal to $2L_{hw}$, secondary bifurcation is detected along the equilibrium path.

Subsequently, two possible limit states are examined, following a methodology similar to the one described for axial loading; (a) localization of wrinkling pattern with an ultimate moment M_1 and (b) a combination of imperfection corresponding to initial and secondary buckling modes associated

with a maximum moment M_n. The minimum value from the corresponding maximum moments M_1 and M_n determines the ultimate moment of the cross-section, denoted as M_u.

7.3.3 Parametric study

The above advanced numerical tools are used to examine buckling of cylindrical high-strength steel shells under pure axial compressive load and pure bending. The cylindrical shells under consideration are thick-walled with properties shown in Table 7 - 2.

Table 7 - 2: Geometric and mechanical properties of tubes

Tube	$t_s\ [mm]$	D/t_s *	$\sigma_Y\ [MPa]$	λ	**Class****
1	6.4	55.56	735	0.517	4
2	8.0	44.45	735	0.463	4
3	10.0	35.56	735	0.414	4
4	12.5	28.45	735	0.370	3
5	14.2	25.05	735	0.347	3
6	16	22.22	735	0.327	2
7	14.2	25.05	590	0.311	2
8	16	22.22	590	0.293	2

** D is equal to 355.6 mm for all tubes,*

*** According to EN-1993-1-1*

The structural behavior is summarized schematically in the axial load-displacement response of the thin-walled Tube 1 in Figure 7 - 5, whereas the behavior of Tube 4 is shown in Figure 7 - 6. The load is normalized with the value $N_y = \sigma_y A$, where A and σ_y are the cross sectional area and the yield stress, respectively. The reported displacement is normalized by the tube length. At a certain displacement value indicated by the first arrow (↓) on the load-displacement curve, first axisymmetric wrinkling is calculated. Secondary bifurcation to a non-axisymmetric mode on the primary path is calculated indicated by the second arrow (↓). The paths corresponding to the two possible limit states are examined, as described in section 7.3.1. The ultimate maximum strength axial load of the cross-section N_u, is equal to N_1, for the localization analysis and is indicated by the arrow (↑) in the two graphs.

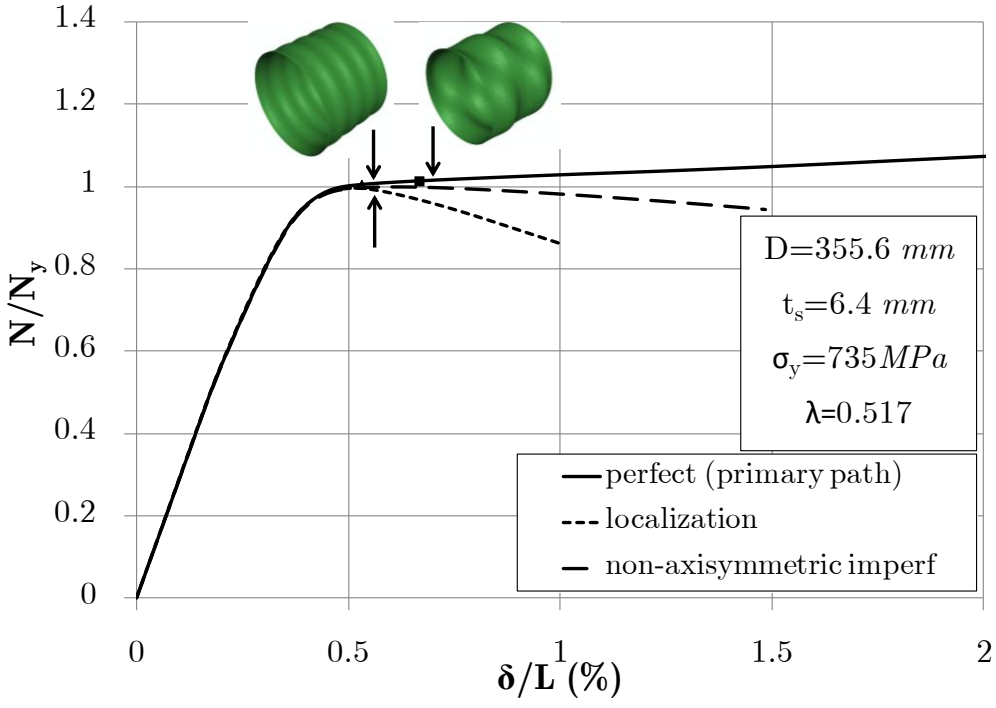

Figure 7 - 5: Axial load – displacement diagram of Tube 1.

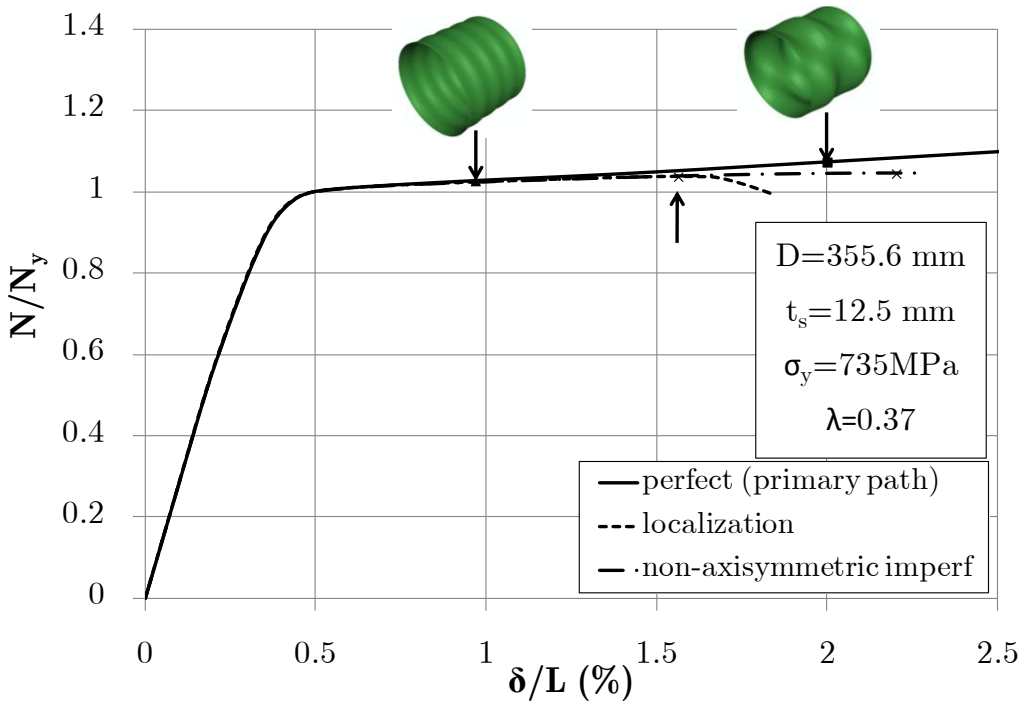

Figure 7 - 6: Axial load – displacement diagram of Tube 4.

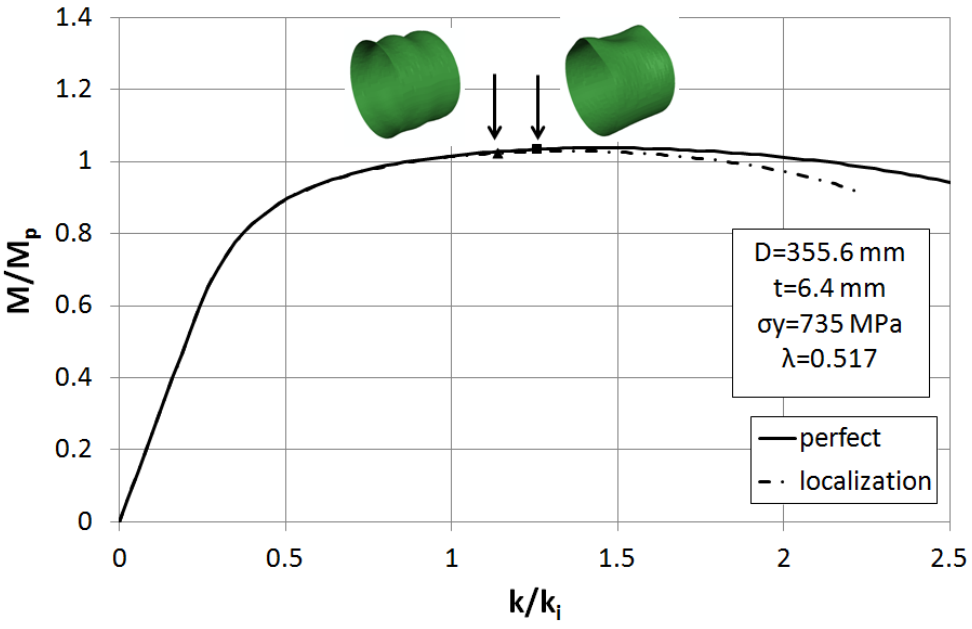

Figure 7 - 7:. Moment-curvature diagram of thin-walled Tube 1.

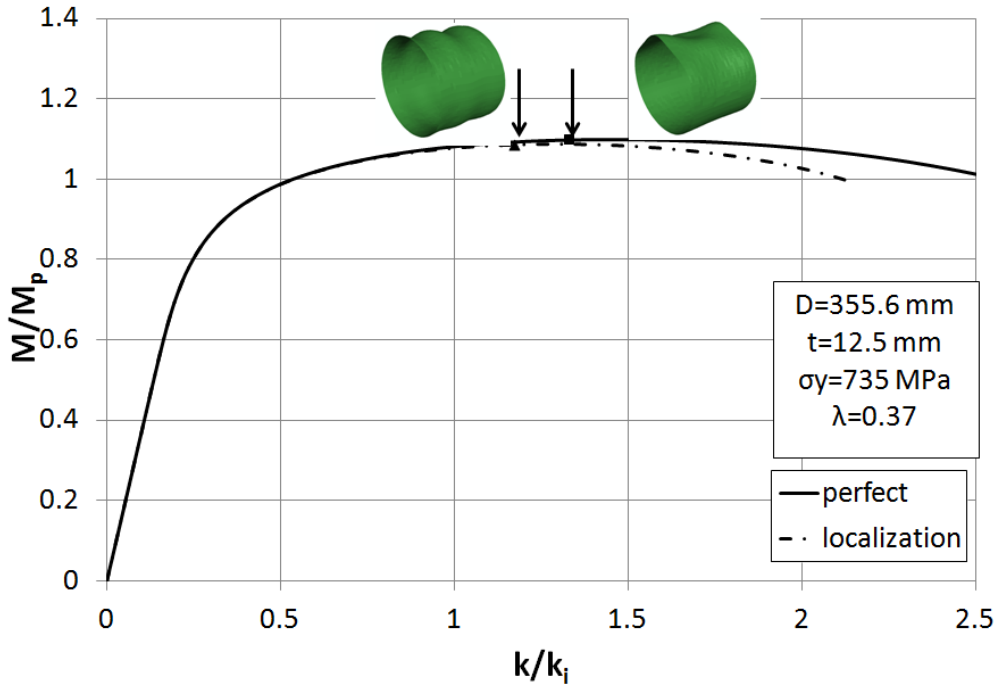

Figure 7 - 8: Moment-curvature diagram of Tube 4.

The bending behavior is shown in the moment- curvature response of Tube 1 in Figure 7 - 7 and of Tube 4 in Figure 7 - 8. The moment is normalized by the fully-plastic moment ($M_p = \sigma_Y t_s D^2$) and the curvature is normalized by the value of characteristic curvature $k_i = t_s / D^2$.

7.4 Comparison with experimental results

Some limited experimental results are also reported on the high-strength steel CHS seamless tubes under consideration for verification purposes. The tests have been conducted by CSM in the course of ATTEL project, and comprise three (3) tests with uniform axial compression, and two (2) tests on bending. The tubes have cross-sections denoted as A, B and C (see Table 7 - 3), and a steel material with yield stress equal to 735 *MPa*. The slenderness values for

sections A, B and C are equal to 0.370, 0.395 and 0.305. The axial load tests failed because of buckle development in the form of bulging near the welds, a typical failure mode for this type of loading. All three tests showed that they are capable of sustaining an axial load significantly higher than the full plastic thrust of the section (see Table 7 - 3). The two bending experiments on sections A and B, because of test set-up limitations, did not reach the local buckling stage. Nevertheless, it has been possible to bend the two tubes at curvature levels corresponding to bending moments higher than the fully plastic moment (see Table 7 - 3).

Table 7 - 3: Experimental results on the high-strength steel tubes

Section	$D\ [mm]$	$t_s\ [mm]$	**Yield Stress [MPa]**	**Ultimate Thust** $N_{u,\exp}\ [kN]$ $\left(N_{u,\exp}/N_y\right)$	**Ultimate Moment** $M_{u,\exp}\ [kNm]$ $\left(M_{u,\exp}/M_p\right)$
A	355.6	12.5	735	10254 (1.033)	1168.6 (1.402)
B	323.9	10	735	7961 (1.082)	805.93 (1.438)
C	193.7	10	735	4414 (1.102)	

classification of HSS CHS members

7.4.1 Comparison with numerical results and test data and discussion

The above predictions of ultimate capacity are plotted against the finite element results and the test data, in Figure 7 - 9 and Figure 7 - 10 for the axial compression and bending respectively, with respect to the slenderness parameter λ. The ultimate axial load and bending moment values are normalized by N_y and M_p respectively. The comparison between numerical results, test data and design provisions indicates that the EN 1993 standard provides a rather conservative ultimate capacity in terms of both axial and bending moment for the value of initial imperfections assumed in the present study.

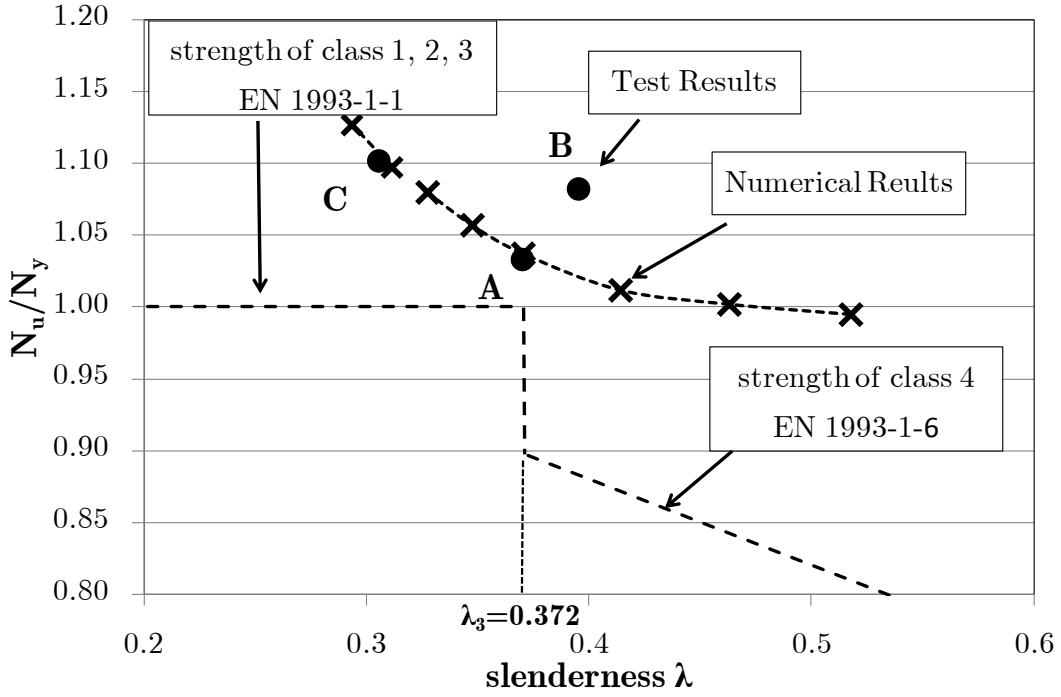

Figure 7 - 9: Stability curve in EN1993 compared with numerical results and experimental data.

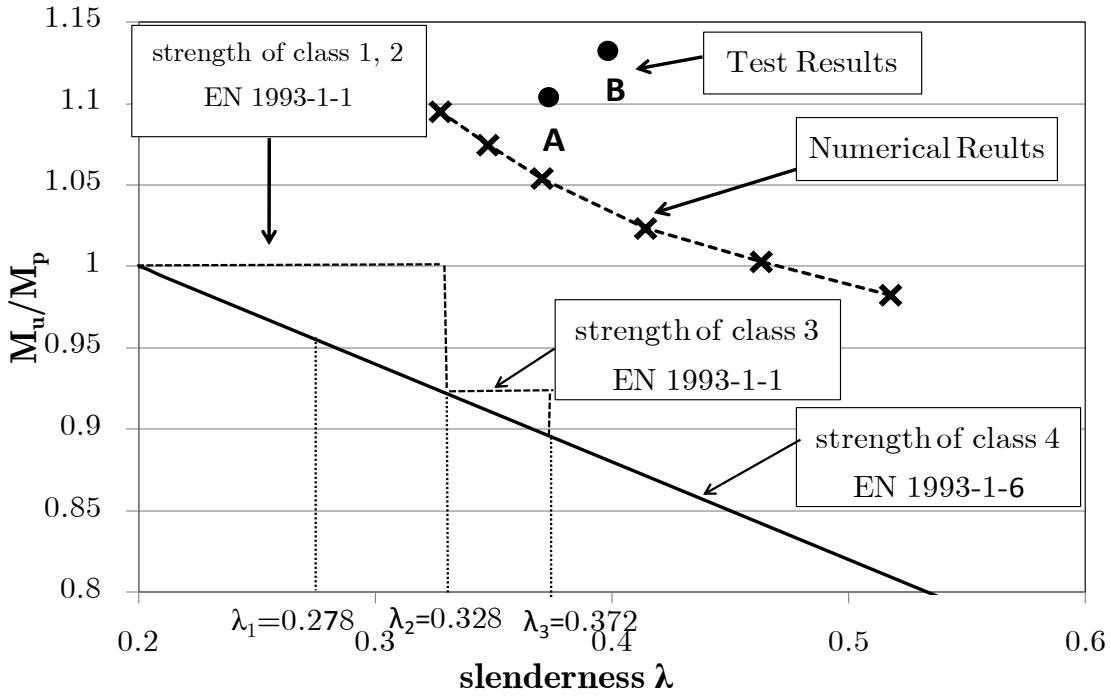

Figure 7 - 10: Stability curve in EN1993 compared with numerical results and experimental data.

In addition, Figure 7 - 11 and Figure 7 - 12 show the numerical results for the deformation capacity of the cross-section for axial (δ_u) and bending (k_u) respectively, normalized by the corresponding values at initial yielding stage (δ_y and k_y), with respect to the value of λ. The values of δ_u and k_u correspond to N_u and M_u respectively. The values of δ_u/δ_y and k_u/k_y indicate significant deformation capacity of the tubes under consideration, well beyond first yielding.

To distinguish between class 1 and class 2, the key issue is deformation capacity. It has been empirically established that a ratio of ultimate deformation over the yield deformation equal to 4, offers a reliable limit for the

"border" between class 1 and class 2 sections.

Therefore, in bending:

- If $M_{\max}$ less than M_y: class 4.
- If $M_{\max}$ less than M_p but higher than M_y: class 3.
- If $M_{\max}$ equal or higher than M_p, and $k_{\max}$ less than $4k_y$: class 2.
- If $M_{\max}$ equal or higher than M_p, and $k_{\max}$ larger than $4k_y$: class 1.

In axial compression

- If $N_{\max}$ less than $N_y \left(= N_p\right)$: class 4.
- If $N_{\max}$ equal or higher than N_y, and $\delta_{\max}$ "very close" to δ_y: class 3.
- If $N_{\max}$ equal or higher than N_y, and $\delta_{\max}$ less than $4\delta_y$: class 2.
- If $N_{\max}$ equal or higher than N_y, and $\delta_{\max}$ larger than $4\delta_y$: class 1.

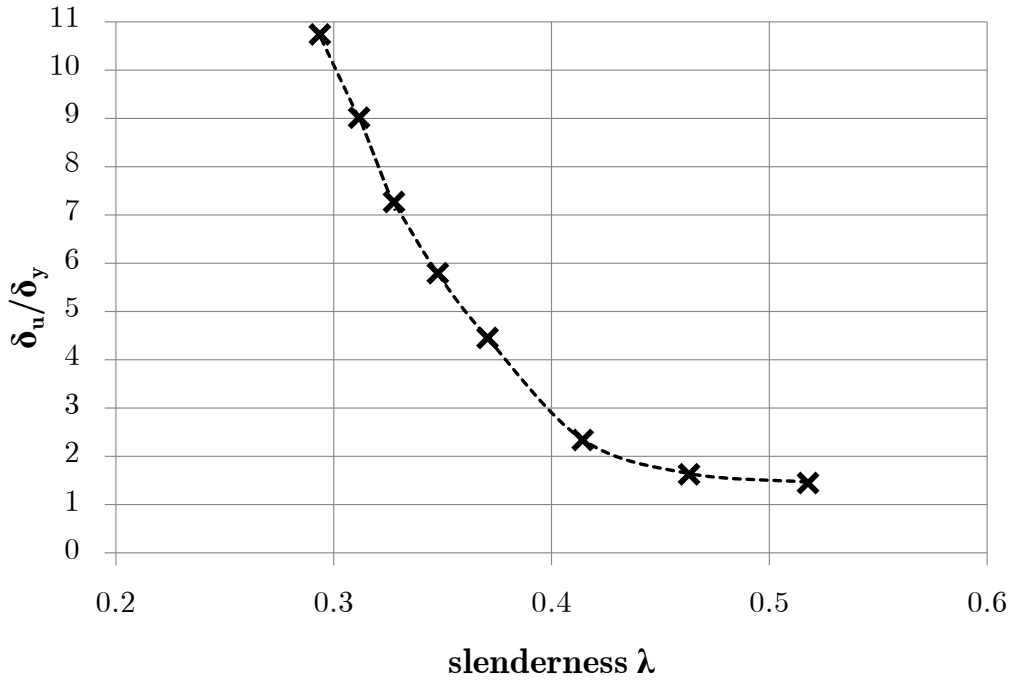

Figure 7 - 11: Deformation capacity of the cross-section under axial load conditions.

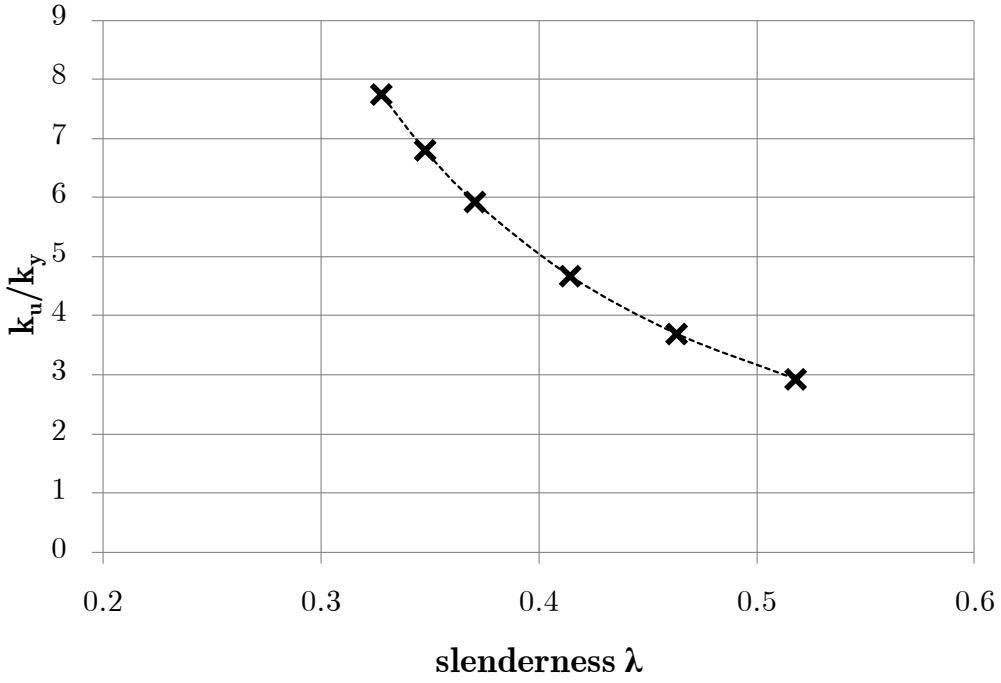

Figure 7 - 12: Deformation capacity of the cross-section under bending moment.

Chapter 8

Conclusions

A large-strain J_2 - non-associative plasticity model has been developed for nonlinear analysis of cylindrical shells. The model maintains the basic formulation and implementation features of the standard J_2 - flow theory, but contains the necessary modifications and enhancements for accurate shell buckling predictions, without any additional parameters required by corner or pseudo-corner theories, reported in previous publications. The model is consistent with shell theory requirements (zero stress normal to the shell laminae), it is numerically integrated through both the robust backward-Euler and forward-Euler substitution scheme.

An enhanced version of the model for large strains is also presented, based on an additive decomposition of the rate-of-deformation tensor. This allows the direct application of the above robust integration schemes in large-strain analysis through a polar decomposition of the deformation gradient and appropriate rotation of the stress and strain tensors, while accounting for zero stress normal to shell laminae. The non-associative constitutive model is implemented within a special-purpose finite element formulation, which uses a

three-node "tube element". Bifurcation buckling in the inelastic range is detected along the equilibrium path through an implementation of the "comparison solid" concept. Special emphasis is paid on the continuity of plastic flow, to overcome numerical problems of convergence.

The numerical results are in excellent agreement with available experimental data and analytical predictions, and demonstrate that the present methodology is capable of describing accurately and efficiently buckling and post-buckling behavior of rather think-walled cylindrical shells in the inelastic range. In addition, the comparison with test data demonstrates the superiority of this non-associative model with respect to the classical associative J_2 - plasticity model in predicting shell buckling in the inelastic range.

Furthermore, wrinkling and post-wrinkling behavior of thick-walled high-strength CHS seamless tubular have been presented in terms of both the ultimate load and the deformation capacity of typical cross-sections, in order to determine their ability to sustain load above the first yield level. The results have been compared with limited test data, and with the EN 1993 provisions for CHS member classification. Considering imperfections and residual stresses obtained from real measurements on high-strength steel seamless tubes, the finite element results indicated significantly higher ultimate capacity with respect to the design rules of the above specification rules, as well as a substantial deformation capacity, indicating the conservativeness of the EN 1993 provisions for high-strength steel CHS member classification.

The contributions of the present dissertation can be summarized in the following:

- A J_2 - non-associative plasticity model is developed, capable of describing the effects of yield surface vertex on the structural response and buckling of shells in an efficient manner.
- Robust integration schemes are presented, accounting for zero stress normal to shell surface and the "consistent moduli" are reported.
- A large-strain J_2 - non-associative plasticity model is also developed for efficient large-strain nonlinear analysis of cylindrical shells, and is integrated using the polar decomposition of deformation gradient and appropriate rotation of stress and rate of deformation tensors.
- The constitutive model is implemented in a user material subroutine and incorporated in an in-house finite element technique for shell buckling analysis.
- The present numerical results are compared successfully with available experimental data and analytical predictions.
- The comparison with test data demonstrates the superiority of this non-associative model with respect to the classical associative J_2 - plasticity model in predicting shell buckling in the inelastic range.

- Buckling calculations on thick-walled seamless tubulars made of high-strength subjected to axial compression and bending are performed, in terms of both the ultimate load and the deformation capacity, and their ability to sustain load well beyond the elastic range is determined.
- Based on the numerical results, considering imperfections and residual stresses obtained from real measurements on high-strength steel seamless tubes, those tubes exhibit significantly higher ultimate load and deformation capacity with respect to the predictions of existing design rules, indicating the conservativeness of current design practice for the case of high-strength steel tubulars.

Appendix I

J_2 - Associative Constitutive Model and Implementation

The classical formulation of J_2 - flow theory with isotropic hardening is described in detail in this Appendix. Furthermore, its numerical integration is presented, using backward-Euler and forward-Euler schemes.

I.1 Model description

In the framework of associated plastic flow the plastic strain rate can be written as

$$\dot{\boldsymbol{\varepsilon}}^p = \dot{\lambda}\frac{\partial F}{\partial \boldsymbol{\sigma}} = \dot{\lambda}\mathbf{s} \tag{I.1}$$

where $\dot{\lambda}$ is a positive scalar.

The consistency condition $\dot{F} = 0$ implies

$$\dot{\varepsilon}_q = \frac{3}{2kH}\mathbf{s}\cdot\dot{\mathbf{s}} \tag{I.2}$$

The von Mises equivalent stress is defined as

$$q = \sqrt{\frac{3}{2}\mathbf{s}\cdot\mathbf{s}} \tag{I.3}$$

and the equivalent plastic strain rate, using equations (I.1) and (I.3) becomes

$$\dot{\varepsilon}_q = \sqrt{\frac{2}{3}\dot{\boldsymbol{\varepsilon}}^p \cdot \dot{\boldsymbol{\varepsilon}}^p} = \sqrt{\frac{2}{3}\dot{\lambda}^2 \mathbf{s}\cdot\mathbf{s}} = \frac{2}{3}\dot{\lambda} q \tag{I.4}$$

Then the plastic strain increment can be expressed as

$$\dot{\boldsymbol{\varepsilon}}^p = \frac{3\dot{\varepsilon}_q}{2q}\mathbf{s} \tag{I.5}$$

and using equation (I.1), equation (I.5) becomes

$$\dot{\boldsymbol{\varepsilon}}^p = \frac{3}{2q}\frac{3}{2qH}(\mathbf{s}\cdot\dot{\mathbf{s}})\mathbf{s} = \frac{3}{2H}(\mathrm{n}\cdot\dot{\mathbf{s}})\mathrm{n} = \frac{3}{2H}\dot{\mathbf{s}}^n \tag{I.6}$$

where $\dot{\mathbf{s}}^n = (\mathbf{n}\cdot\dot{\mathbf{s}})\mathbf{n}$ and $\mathbf{n} = \dfrac{\mathbf{s}}{\|\mathbf{s}\|}$ is the unit normal to the yield surface. The rate form of the classical flow theory in equation (I.6) implies that the plastic strain increment is always normal to the yield surface. The instantaneous moduli for this model can be written as follows

$$\mathbf{D}_{ep} = 2G\mathbf{I} + 3\left(K - \frac{2}{3}G\right)\mathbf{J} - \frac{3G}{q^2}\left(\frac{1}{1+H/3G}\right)\mathbf{s}\otimes\mathbf{s} \tag{I.7}$$

The components of $\mathbf{D}_{ep}$ with respect to the covariant basis can be written

$$D_{ep}^{ijkl} = \frac{E}{2(1+\nu)}\left(g^{jl}g^{ik} + g^{il}g^{jk}\right) + \frac{E\nu}{(1-2\nu)(1+\nu)}g^{ij}g^{kl} - \frac{3G}{q^2}\left(\frac{1}{1+H/3G}\right)s^{ij}\otimes s^{kl} \tag{I.8}$$

I.2 Numerical integration of the J_2 - Associative Plasticity Model

The method employed to integrate the above constitutive equations follows

an elastic predictor–plastic corrector scheme. Using the backward-Euler integration scheme for equation (I.1), the increment of plastic strain is written

$$\Delta\boldsymbol{\varepsilon}^{p} = \frac{3}{2q_{n+1}}\Delta\varepsilon_q \mathbf{s}_{n+1} \tag{I.9}$$

The final stress at stage $(n+1)$ is written

$$\boldsymbol{\sigma}_{n+1} = \boldsymbol{\sigma}^{e} - \frac{3G\,\Delta\varepsilon_q}{2q_{n+1}}\mathbf{s}_{n+1} \tag{I.10}$$

where the purely elastic (trial) stress is defined by the formula $\boldsymbol{\sigma}^{e} = \boldsymbol{\sigma}_n + \mathbf{D}\Delta\boldsymbol{\varepsilon}$. From (I-10) the deviatoric stress is

$$\mathbf{s}_{n+1} = \mathbf{s}^{e} - \frac{3G\,\Delta\varepsilon_q}{2q_{n+1}}\mathbf{s}_{n+1} \tag{I.11}$$

or

$$\mathbf{s}_{n+1} = \frac{1}{\left(1+\dfrac{3G\,\Delta\varepsilon_q}{2q_{n+1}}\right)}\mathbf{s}^{e} \tag{I.12}$$

which shows that the final deviator stress $\mathbf{s}_{n+1}$ is co-linear with the elastic stress $\mathbf{s}^{e}$. Therefore, in the deviatoric plane, "plastic correction" from the elastic predictor onto the yield surface takes place "radially". Squaring equation (I.11), the effective stress at the final state is calculated as follows

$$q_{n+1} = q^{e} - 3G\,\Delta\varepsilon_q \tag{I.13}$$

From (I-13), the yield function becomes

$$q^{e} - 3G\,\Delta\varepsilon_q - k\left(\varepsilon_q\big|_n + \Delta\varepsilon_q\right) = 0 \tag{I.14}$$

The above non-linear equation (I.14) is solved in terms of the equivalent plastic strain $\Delta\varepsilon_q$ using Newton's method. Once $\Delta\varepsilon_q$ is found, equation (I.12) provides $\mathbf{s}_{n+1}$ and (I.11) the final stress $\boldsymbol{\sigma}_{n+1}$. Finally the equivalent plastic strain at stage $(n+1)$ is $\varepsilon_q\big|_{n+1} = \varepsilon_q\big|_n + \Delta\varepsilon_q$, which completes the integration process.

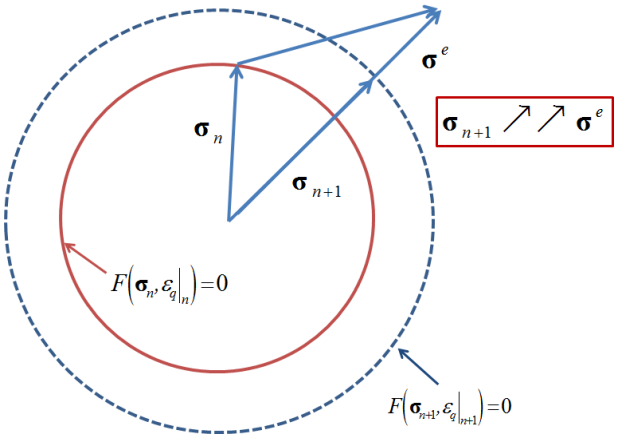

Figure I - 1: Geometrical representation of "radial return" algorithm.

Nevertheless, in accordance with shell theory, it is required that the traction component normal to any shell lamina is zero at any stage of deformation. In such a case, the strain increment can be decomposed in two parts (see equation (2.22)). The final stress becomes

$$\boldsymbol{\sigma}_{n+1} = \bar{\boldsymbol{\sigma}}^e + 2G\,\Delta\varepsilon_{33}\mathbf{a} - \frac{3G\,\Delta\varepsilon_q}{q_{n+1}}\mathbf{s}_{n+1} \tag{I.15}$$

where $\bar{\boldsymbol{\sigma}}^e$ is the elastic predictor that corresponds to the known part of $\Delta\boldsymbol{\varepsilon}$ (eq. (2.28)).It should be noted that $\bar{\boldsymbol{\sigma}}^e$ is different from the elastic prediction $\boldsymbol{\sigma}^e$. From equation (I.15) the hydrostatic and the deviatoric parts of the final stress

are written as

$$p_{n+1} = \bar{p}^e - K\,\Delta\varepsilon_{33}\,g^{33} \tag{I.16}$$

$$\mathbf{s}_{n+1} = \frac{1}{1+\dfrac{3G\,\Delta\varepsilon_q}{q_{n+1}}}\left(\bar{\mathbf{s}}^e + 2G\,\Delta\varepsilon_{33}\mathbf{a}'\right) \tag{I.17}$$

Equation (I.17) shows that $\mathbf{s}_{n+1}$ and $\bar{\mathbf{s}}^e$ are not co-linear and the correction is not on the deviatoric plane. Squaring equation (I.17), the von Mises equivalent stress at the final state is calculated as follows

$$q_{n+1} = \sqrt{\bar{q}^e + 4G\,\Delta\varepsilon_{33}^2\,g^{33}\,g^{33} + 6G\,\Delta\varepsilon_{33}\,\bar{s}^{(e)^{33}}} - 3G\,\Delta\varepsilon_q \tag{I.18}$$

where $\bar{q}^e = \sqrt{(3/2)\,\bar{\mathbf{s}}^e \cdot \bar{\mathbf{s}}^e}$.

From consistency, the final stress has to satisfy the yield criterion and this can be expressed as follows

$$q_{n+1}\left(\Delta\varepsilon_q, \Delta\varepsilon_{33}\right) = k\left(\varepsilon_{q|n} + \Delta\varepsilon_q\right) \tag{I.19}$$

Enforcing the conditions of zero stress normal to any shell lamina ($\sigma_{n+1}^{33} = 0$), and using (I-15) the following equation is obtained

$$\left(q_{n+1} + 3G\,\Delta\varepsilon_q\right) p_{n+1}\,g^{33} - \left(\bar{s}^{(e)^{33}} + \frac{4G}{3}\,\Delta\varepsilon_{33}\,g^{33}\,g^{33}\right) = 0 \tag{I.20}$$

Summarizing the above formulation, equations (I.16), (I.18), (I.20) and the yield criterion (I.19) constitute a system of four equations to be solved for the four unknowns, namely, q_{n+1}, p_{n+1}, $\Delta\varepsilon_q$ and $\Delta\varepsilon_{33}$. Considering $\Delta\varepsilon_q$ and $\Delta\varepsilon_{33}$ as the primary unknowns, equations (I.20) and (I.19) can be solved in terms of

$\Delta\varepsilon_q$, $\Delta\varepsilon_{33}$ using Newton's method as described in more detail in Appendix II-2.

I.3 Linearization moduli for the von Mises Plasticity Model

The consistent rigidity moduli are computed from the basic equation $\mathbf{D}_{ep}^{c} = \frac{\partial \boldsymbol{\sigma}_{n+1}}{\partial \boldsymbol{\varepsilon}_{n+1}}$. In the following, four-order tensor $\partial\boldsymbol{\sigma}_{n+1}/\partial\boldsymbol{\varepsilon}_{n+1}$ is computed for the backward-Euler integration scheme and presented in the previous section. In particular, the final stress $\boldsymbol{\sigma}_{n+1}$ can be written as

$$d\,\boldsymbol{\sigma}_{n+1} = \mathbf{D}\,d\,\boldsymbol{\varepsilon}_{n+1} - 2G\left(\Delta\varepsilon_q\,d\,\mathbf{N}_{n+1} + d\,\varepsilon_q\;\mathbf{N}_{n+1}\right) \tag{I.21}$$

where the dimensionless tensor $\mathbf{N}$ is defined at a certain stress state $\boldsymbol{\sigma}$ by the following expression:

$$\mathbf{N}_{n+1} = \mathbf{N}^{e} = \frac{3}{2\,q^{e}}\mathbf{s}^{e} \tag{I.22}$$

Differentiation of equation (I.22) gives

$$d\,\mathbf{N}_{n+1} = \frac{\partial \mathbf{N}^{e}}{\partial \boldsymbol{\sigma}^{e}}\,d\,\boldsymbol{\sigma}^{e} = \frac{\partial \mathbf{N}^{e}}{\partial \boldsymbol{\sigma}^{e}}\frac{\partial \boldsymbol{\sigma}^{e}}{\partial \boldsymbol{\varepsilon}_{n+1}}\,d\,\boldsymbol{\varepsilon}_{n+1} \tag{I.23}$$

One can show that

$$\frac{\partial \mathbf{N}}{\partial \boldsymbol{\sigma}} = -\frac{1}{q}\mathbf{N}\otimes\mathbf{N} + \frac{3}{2q}\mathbf{I} \tag{I.24}$$

Therefore,

$$\frac{\partial \mathbf{N}^{e}}{\partial \boldsymbol{\sigma}^{e}} = -\frac{1}{q}\mathbf{N}^{e}\otimes\mathbf{N}^{e} + \frac{3}{2q}\mathbf{I} \tag{I.25}$$

and differentiation of the purely elastic (trial) stress gives

$$d\,\boldsymbol{\sigma}^e = \mathbf{D}\,d\,\boldsymbol{\varepsilon}_{n+1} \tag{I.26}$$

Using equations (I.25) and (I.26), equation (I.23) becomes

$$d\,\mathbf{N}_{n+1} = \frac{2\mathrm{G}}{q}\left(\frac{3}{2}\mathbf{I} - \mathbf{N}^e \otimes \mathbf{N}^e\right) d\,\boldsymbol{\varepsilon}_{n+1} \tag{I.27}$$

Differentiation of equation (I.14) gives

$$\frac{\partial q^e}{\partial \boldsymbol{\sigma}^e}\, d\,\boldsymbol{\sigma}^e - 3G\, d\,\varepsilon_q - \frac{d\,k_{n+1}}{d\,\varepsilon_q\big|_{n+1}}\, d\,\varepsilon_q\big|_{n+1} = 0 \tag{I.28}$$

or equivalently,

$$d\,\varepsilon_q = \frac{2G}{3G+H}\,\frac{3}{2q^e}\,\mathbf{s}^e\, d\,\boldsymbol{\varepsilon}_{n+1} \tag{I.29}$$

Substituting,

$$\begin{aligned} d\,\boldsymbol{\sigma}_{n+1} = \mathbf{D}\,d\,\boldsymbol{\varepsilon}_{n+1} - 4G\Bigg\{&\left(\frac{1}{3G+H}\right)\frac{3}{2q^e}\mathbf{s}^e\,\frac{3}{2q_{n+1}}\mathbf{s}_{n+1} \\ &+ \frac{\Delta\varepsilon_q\, G}{q_{n+1}}\left(\frac{3}{2}\mathbf{I} - \left(\frac{3}{2q_{n+1}}\right)^2 \mathbf{s}_{n+1}\otimes\mathbf{s}_{n+1}\right)\Bigg\} d\,\boldsymbol{\varepsilon}_{n+1} \end{aligned} \tag{I.30}$$

so that

$$\mathbf{D}^c_{ep} = \mathbf{D} - 4G\left\{\left(\frac{1}{3G+H}\right)\mathbf{N}_{n+1}\otimes\mathbf{N}_{n+1} + \frac{\Delta\varepsilon_q\, G}{q_{n+1}}\left(\frac{3}{2}\mathbf{I} - \mathbf{N}_{n+1}\otimes\mathbf{N}_{n+1}\right)\right\} \tag{I.31}$$

Finally, the condition of zero stress normal to shell laminae is imposed considering $d\,\sigma^{33} = 0$ in the rigitidy moduli of equation (I.31).

Appendix II

Application of Newton's Method in Constitutive Model Implementation

II.1 J_2 - non-associative model

Equations (2.30), (2.32), (2.36), (2.35) or (2.30), (2.40), (2.41), (2.35) are solved using the Newton method. The unknowns $\Delta\varepsilon_q$ and $\Delta\varepsilon_{33}$ are chosen as the primary unknowns considering that equations (2.35) and (2.36) or (2.35) and (2.41) are the basic equations. Denoting as $\delta\left(\Delta\varepsilon_q\right)$ and $\delta\left(\Delta\varepsilon_{33}\right)$ the corrections of $\Delta\varepsilon_q$ and $\Delta\varepsilon_{33}$, the Newton equations become:

$$\begin{bmatrix} A_{11} & A_{12} \\ A_{21} & A_{22} \end{bmatrix} \begin{bmatrix} \delta\left(\Delta\varepsilon_q\right) \\ \delta\left(\Delta\varepsilon_{33}\right) \end{bmatrix} = \begin{bmatrix} b_1 \\ b_2 \end{bmatrix} \tag{II.1}$$

or

$$\begin{aligned} \delta\left(\Delta\varepsilon_q\right) &= \frac{\left(A_{22}\, b_1 - A_{12}\, b_2\right)}{det\, A} \\ \delta\left(\Delta\varepsilon_{33}\right) &= \frac{\left(A_{11}\, b_2 - A_{21}\, b_1\right)}{det\, A} \end{aligned} \tag{II.2}$$

where

$$det\, A = A_{11}\, A_{22} - A_{12}\, A_{21} \tag{II.3}$$

The $\Delta\varepsilon_q$ and $\Delta\varepsilon_{33}$ is updated by

$$\begin{aligned} \Delta\varepsilon_q &\to \Delta\varepsilon_q + \delta\left(\Delta\varepsilon_q\right) \\ \Delta\varepsilon_{33} &\to \Delta\varepsilon_{33} + \delta\left(\Delta\varepsilon_{33}\right) \end{aligned} \tag{II.4}$$

The iteration continues until $b_1,\ b_2 \to 0$.

For the backward-Euler scheme, the constants A_{ij} and b_i are given in the following expressions:

$$A_{11} = \frac{\partial f_1}{\partial \Delta\varepsilon_q} = \frac{\partial q}{\partial \Delta\varepsilon_q} - \frac{\partial k}{\partial \Delta\varepsilon_q} = \frac{\partial q}{\partial \Delta\varepsilon_q} - H \tag{II.5}$$

$$A_{12} = \frac{\partial f_1}{\partial \Delta\varepsilon_{33}} = \frac{\partial q}{\partial \Delta\varepsilon_{33}} - \frac{\partial k}{\partial \Delta\varepsilon_{33}} = \frac{\partial q}{\partial \Delta\varepsilon_{33}} \tag{II.6}$$

$$\begin{aligned} A_{21} = \frac{\partial f_2}{\partial \Delta\varepsilon_q} = \frac{3G}{h_{n+1}^2} s_n^{33} + p_{n+1} g^{33} \Bigg(& -\frac{3G h'_{1|n+1}}{h_{n+1}^2} \\ & + \frac{\left(3G\,\Delta\varepsilon_q H'_{n+1} + 3G H_{n+1}\right) q_{n+1} h_{1|n+1} - 3G\,\Delta\varepsilon_q H_{n+1} \left(\dfrac{\partial q}{\partial \Delta\varepsilon_q} h_{1|n+1} + q_{n+1} h'_{1|n+1} \right)}{q_{n+1}^2 h_{1|n+1}^2} \Bigg) \end{aligned} \tag{II.7}$$

$$\begin{aligned} A_{22} = \frac{\partial f_2}{\partial \Delta\varepsilon_{33}} = & \left(1 + \frac{3G}{h_{n+1}} + \frac{3G\,\Delta\varepsilon_q H_{n+1}}{q_{n+1} h_{1|n+1}}\right)\left(-K g^{33}\right) g^{33} \\ & - \frac{3G\,\Delta\varepsilon_q H_{n+1} h_{1|n+1} \dfrac{\partial q}{\partial \Delta\varepsilon_{33}}}{q_{n+1}^2 h_{1|n+1}^2} p_{n+1} g^{33} - \frac{4}{3} G g^{33} g^{33} \end{aligned} \tag{II.8}$$

and

$$b_1 = -q_{n+1}\left(\Delta\varepsilon_q, \Delta\varepsilon_{33}\right) + k\left(\varepsilon_{q|n} + \Delta\varepsilon_q\right) \tag{II.9}$$

$$b_2 = -\left(1 + \frac{3G}{h_{n+1}} + \frac{3G\,\Delta\varepsilon_q H_{n+1}}{q h_{1|n+1}}\right) p_{n+1} g^{33} + \left(\bar{s}^{(e)^{33}} + \frac{4G}{3}\Delta\varepsilon_{33} g^{33} g^{33} + \frac{3G}{h_{n+1}} s^{33}\right) \tag{II.10}$$

where

$$\frac{\partial q\left(\Delta\varepsilon_q,\Delta\varepsilon_{33}\right)}{\partial\Delta\varepsilon_q}=\left(\frac{3Gh'_{1|n+1}\,h_{n+1}^{-2}}{1+3G\,h_{n+1}^{-1}}\right)q_{n+1}+\left(\frac{1}{1+3G\,h_{n+1}^{-1}}\right)$$
$$\left\{\frac{\left(3G\,\Delta\varepsilon_q\,H'_{n+1}+3G\,H_{n+1}\right)}{h_{1|n+1}}+\frac{3G\,\Delta\varepsilon_q\,H_{n+1}h'_{1|n+1}}{h_{1|n+1}^{2}}\right.$$
$$\left.+\frac{-9G^2h'_{1|n+1}\,h_{n+1}^{-3}\,q_n^2-3Gh'_{1|n+1}\,h_{n+1}^{-2}\,Q^2-9G^2\,\Delta\varepsilon_{33}\,h'_{1|n+1}\,h_{n+1}^{-2}\,s_n^{33}}{\left(1+3G\,h_{n+1}^{-1}\right)q_{n+1}+3G\,\Delta\varepsilon_q\,H_{n+1}h_{1|n+1}^{-1}}\right\} \tag{II.11}$$

$$\frac{\partial q\left(\Delta\varepsilon_q,\Delta\varepsilon_{33}\right)}{\partial\Delta\varepsilon_{33}}=\left(\frac{1}{1+3G\,h_{n+1}^{-1}}\right)\left(\frac{4G^2\,\Delta\varepsilon_{33}\,g^{33}\,g^{33}+3G\left(\bar{s}^{(e)^{33}}+3G\,h_{n+1}^{-1}\,s_n^{33}\right)}{\left(1+3G\,h_{n+1}^{-1}\right)q_{n+1}+3G\,\Delta\varepsilon_q\,H_{n+1}h_{1|n+1}^{-1}}\right) \tag{II.12}$$

For the forward-Euler scheme, the constants A_{ij} and b_i are given in the following expressions:

$$A_{11}=\frac{\partial f_1}{\partial\Delta\varepsilon_q}=\frac{\partial q}{\partial\Delta\varepsilon_q}-\frac{\partial k}{\partial\Delta\varepsilon_q}=\frac{\partial q}{\partial\Delta\varepsilon_q}-H \tag{II.13}$$

$$A_{12}=\frac{\partial f_1}{\partial\Delta\varepsilon_{33}}=\frac{\partial q}{\partial\Delta\varepsilon_{33}}-\frac{\partial k}{\partial\Delta\varepsilon_{33}}=\frac{\partial q}{\partial\Delta\varepsilon_{33}} \tag{II.14}$$

$$A_{21}=\frac{\partial f_2}{\partial\Delta\varepsilon_q}=-\frac{3G\,H_{n+1}}{q_n h_{1|n}}s_n^{33} \tag{II.15}$$

$$A_{22}=\frac{\partial f_2}{\partial\Delta\varepsilon_{33}}=-\left(1+\frac{3G}{h_n}\right)\left(-Kg^{33}\right)g^{33}+\frac{4}{3}Gg^{33}g^{33} \tag{II.16}$$

and

$$b_1=-q_{n+1}\left(\Delta\varepsilon_q,\Delta\varepsilon_{33}\right)+k\left(\varepsilon_{q|n}+\Delta\varepsilon_q\right) \tag{II.17}$$

$$b_2=-\left(1+\frac{3G}{h_n}+\frac{3G\,\Delta\varepsilon_q\,H_n}{qh_{1|n}}\right)p_{n+1}\,g^{33}+\left(\bar{s}^{(e)^{33}}+\frac{4G}{3}\Delta\varepsilon_{33}\,g^{33}\,g^{33}+\frac{3G}{h_n}s^{33}\right) \tag{II.18}$$

where

$$\frac{\partial q\left(\Delta\varepsilon_q,\Delta\varepsilon_{33}\right)}{\partial\Delta\varepsilon_q}=\left(-\frac{H_n\,q_n^{-1}h_{1|n+1}^{-1}}{\left(1+3G\,h_n^{-1}\right)^2 q_{n+1}}\right)\left(9G^2\left(\frac{1}{h_n}-\frac{\Delta\varepsilon_q\,H_n}{q_n h_{1|n}}\right)q_n^2+3G^2\,Q^2+9G^2\,\Delta\varepsilon_{33}\,s_n^{33}\right) \tag{II.19}$$

$$\frac{\partial q\left(\Delta\varepsilon_q,\Delta\varepsilon_{33}\right)}{\partial\Delta\varepsilon_{33}}=\left(\frac{1}{1+3G\,h_n^{-1}}\right)\left(\frac{4G^2\,\Delta\varepsilon_{33}\,g^{33}\,g^{33}+3G\,\bar{s}^{(e)^{33}}}{\left(1+3G\,h_n^{-1}\right)q_{n+1}}+\frac{9G^2\left(h_n^{-1}+H_n\,\Delta\varepsilon_q\,q_n^{-1}\,h_{1|n}^{-1}\right)s_n^{33}}{\left(1+3G\,h_n^{-1}\right)q_{n+1}}\right) \tag{II.20}$$

II.2 J_2 - associative model

In the framework of associated plastic theory, equations (I.16), (I.18), (I.19) and (I.20) are solved using the Newton method. For the backward-Euler scheme, the constants A_{ij} and b_i are given in the following expressions:

$$A_{11}=\frac{\partial f_1}{\partial\Delta\varepsilon_q}=\frac{\partial q}{\partial\Delta\varepsilon_q}-\frac{\partial k}{\partial\Delta\varepsilon_q}=-3G-H \tag{II.21}$$

$$A_{12}=\frac{\partial f_1}{\partial\Delta\varepsilon_{33}}=\frac{\partial q}{\partial\Delta\varepsilon_{33}}-\frac{\partial k}{\partial\Delta\varepsilon_{33}}=\frac{\partial q}{\partial\Delta\varepsilon_{33}} \tag{II.22}$$

$$A_{21}=\frac{\partial f_2}{\partial\Delta\varepsilon_q}=3G\,\bar{s}^{(e)^{33}}+4G^2\,\Delta\varepsilon_{33}\,g^{33}\,g^{33} \tag{II.23}$$

$$A_{22}=\frac{\partial f_2}{\partial\Delta\varepsilon_{33}}=\left(q_{n+1}+3G\,\Delta\varepsilon_q\right)\left(-Kg^{33}\right)g^{33}-\frac{4}{3q_{n+1}}Gg^{33}g^{33}+\frac{\partial q}{\partial\Delta\varepsilon_{33}}\,p_{n+1}\,g^{33}-\left(\bar{s}^{(e)^{33}}+\frac{4G}{3}\Delta\varepsilon_{33}\,g^{33}\,g^{33}\right)\frac{\partial q}{\partial\Delta\varepsilon_{33}} \tag{II.24}$$

and

$$b_1=-q_{n+1}\left(\Delta\varepsilon_q,\Delta\varepsilon_{33}\right)+k\left(\varepsilon_{q|n}+\Delta\varepsilon_q\right) \tag{II.25}$$

$$b_2 = -\left(q_{n+1} + 3G\,\Delta\varepsilon_q\right) p_{n+1}\, g^{33} + \left(\overline{s}^{(e)^{33}} + \frac{4G}{3}\,\Delta\varepsilon_{33}\, g^{33}\, g^{33}\right) q_{n+1} \tag{II.26}$$

where

$$\frac{\partial q\left(\Delta\varepsilon_q, \Delta\varepsilon_{33}\right)}{\partial \Delta\varepsilon_{33}} = \frac{3G\,\overline{s}^{(e)^{33}} + 4G^2\,\Delta\varepsilon_{33}\, g^{33}\, g^{33}}{q_{n+1} + 3G\,\Delta\varepsilon_q} \tag{II.27}$$

For the forward-Euler scheme, the constants A_{ij} and b_i are given in the following expressions:

$$A_{11} = \frac{\partial f_1}{\partial \Delta\varepsilon_q} = \frac{\partial q}{\partial \Delta\varepsilon_q} - \frac{\partial k}{\partial \Delta\varepsilon_q} = \frac{\partial q}{\partial \Delta\varepsilon_q} - H \tag{II.28}$$

$$A_{12} = \frac{\partial f_1}{\partial \Delta\varepsilon_{33}} = \frac{\partial q}{\partial \Delta\varepsilon_{33}} - \frac{\partial k}{\partial \Delta\varepsilon_{33}} = \frac{\partial q}{\partial \Delta\varepsilon_{33}} \tag{II.29}$$

$$A_{21} = \frac{\partial f_2}{\partial \Delta\varepsilon_q} = -\frac{3G}{q_n} s_n^{33} \tag{II.30}$$

$$A_{22} = \frac{\partial f_2}{\partial \Delta\varepsilon_{33}} = -\left(-Kg^{33}\right) g^{33} + \frac{4}{3} G g^{33} g^{33} \tag{II.31}$$

and

$$b_1 = -q_{n+1}\left(\Delta\varepsilon_q, \Delta\varepsilon_{33}\right) + k\left(\varepsilon_{q|n} + \Delta\varepsilon_q\right) \tag{II.32}$$

$$b_2 = -\,p_{n+1}\, g^{33} + \left(\overline{s}^{(e)^{33}} + \frac{4G}{3}\,\Delta\varepsilon_{33}\, g^{33}\, g^{33} - \frac{3G}{q_n} s^{33}\,\Delta\varepsilon_q\right) \tag{II.33}$$

where

$$\frac{\partial q\left(\Delta\varepsilon_q, \Delta\varepsilon_{33}\right)}{\partial \Delta\varepsilon_q} = \frac{9G^2\,\Delta\varepsilon_q - 3G^2\,Q^2/q_n - 9G^2\,\Delta\varepsilon_{33}\, s_n^{33}/q_n}{q_{n+1}} \tag{II.34}$$

$$\frac{\partial q\left(\Delta\varepsilon_q,\Delta\varepsilon_{33}\right)}{\partial\Delta\varepsilon_{33}}=\frac{3G\,\bar{s}^{(e)^{33}}+4G^2\,\Delta\varepsilon_{33}\,g^{33}\,g^{33}-9G^2\,\Delta\varepsilon_q\,s_n^{33}/q_n}{q_{n+1}} \tag{II.35}$$

Appendix III

Algorithm for Polar Decomposition in Curvilinear Coordinates

This algorithm computes the squares of the principal stretches λ_i^2, $(i=1,2,3)$, which are the eigenvalues of $\mathbf{C}$, by solving in closed form the characteristic polynomial. The algorithm has been introduced by Franca (1989), it is described in the book of Simo and Hughes (1998), pp 244, and is adapted herein for the case of curvilinear coordinates. The covariant base vector and the contravariant (reciprocal) base vector in the beginning of the step $\mathbf{G}_i$, $\mathbf{G}^j$, the covariant base vector and the contravariant base vector in the current configuration $\mathbf{g}_i$, $\mathbf{g}^j$ respectively, are given. Let $a_i, (i=1,2,3)$ be the principal invariants of $\mathbf{U}$ defined as

$$\begin{aligned} a_1 &= g_{ij}G^{ij} \\ a_2 &= \frac{1}{2}\left[\left(g_{ij}G^{ij}\right)^2 - a_{ij}G^{ij}\right] \\ a_3 &= \det\left(g_{ik}\right) \end{aligned} \qquad \text{(III.1)}$$

and

$$b = a_2 - \frac{a_1^2}{3}$$
$$d = -\frac{2}{27}a_1^3 + a_1\frac{a_2}{3} - a_3 \qquad \text{(III.2)}$$

where

$$a_{ij} = g_{ik}g_{jl}G^{kl} \qquad \text{(III.3)}$$

If $b = 0$ $(b < tolerence)$

$$\lambda_1 = \lambda_2 = \lambda_3 = \sqrt{\frac{a_1}{3}} \qquad \text{(III.4)}$$

else

$$m = 2\sqrt{\frac{-b}{3}}$$
$$n = \frac{3d}{mb} \qquad \text{(III.5)}$$
$$aux = 1 - n^2$$

If $aux < 0$ then

$$if\ \ n > 1 \Rightarrow t = 0$$
$$if\ \ n < 1 \Rightarrow t = \frac{\pi}{3} \qquad \text{(III.6)}$$

else

$$t = \frac{1}{3}\arctan\left(\frac{\sqrt{aux}}{n}\right) \qquad \text{(III.7)}$$

end if

$$x_i = m\cos\left[t + \frac{2(i-1)\pi}{3}\right],\ i = 1,2,3 \qquad \text{(III.8)}$$

and

$$\lambda_i^2 = x_i + \frac{a_1}{3}$$
$$\lambda_i = \sqrt{\lambda_i^2} \qquad \text{(III.9)}$$

end if.

Compute the invariants of $\mathbf{U}$

$$i_1 = \lambda_1 + \lambda_2 + \lambda_3$$
$$i_2 = \lambda_1\lambda_2 + \lambda_2\lambda_3 + \lambda_3\lambda_1 \qquad \text{(III.10)}$$
$$i_3 = \lambda_1\lambda_2\lambda_3$$

Furthermore, the coefficients A_i, B_i (i=1,2,3) in the expressions (3.13) and (3.16) for $\mathbf{U}$, $\mathbf{U}^{-1}$ are defined as

$$A_1 = -\frac{1}{D}$$
$$A_2 = \frac{\left(i_1^2 - i_2\right)}{D} \qquad \text{(III.11)}$$
$$A_3 = \frac{i_1 i_3}{D}$$

and

$$B_1 = \frac{1}{i_3}$$
$$B_2 = \frac{-i_1}{i_3} \qquad \text{(III.12)}$$
$$B_3 = \frac{i_2}{i_3}$$

where $D = i_1 i_2 - i_3$.

Appendix IV

Classicification of CHS Tubular Members

Table 1 shows the classification of CHS tubular members according the EN 1993-1-1. For consistency with the present analysis, the slenderness limits have been also given in terms of the so-called "shell slenderness", defined as:

$$\lambda = \sqrt{\frac{\sigma_Y}{\sigma_e}} \tag{IV.1}$$

where

$$\sigma_e = 0.605 E C_x \frac{t}{R} \tag{IV.2}$$

is the elastic buckling stress, and the value of C_x is taken equal to 0.6, representing an infinitely long cylinder, free of boundary condition effects.

For Class 1, 2 and 3 CHS sections ($\lambda \leq 0.372$), the EN 1993-1-1 standard specifies that the ultimate axial compressive capacity N_u is equal to the fully-plastic axial load $N_Y = \sigma_Y A$, where A is the cross-sectional area. If the value of λ exceeds 0.372, then the cross-section is classified as Class 4, implying that buckling occurs in the elastic range, and its ultimate axial compressive capacity N_u is calculated from the EN 1993-1-6 rules for buckling of cylindrical shells, as follows:

$$N_u = \sigma_{x,Rk} A \tag{IV.3}$$

where the buckling strength $\sigma_{x,Rk}$ can be written:

$$\sigma_{x,Rk} = \chi(\lambda)\sigma_Y \tag{IV.4}$$

The reduction function χ depends on shell slenderness as follows:

$$\chi(\lambda) = \begin{cases} 1 & \lambda \le 0.2 \\ 1 - 0.6\left(\dfrac{\lambda - 0.2}{\lambda_P - 0.2}\right) & 0.2 < \lambda \le \lambda_P \\ \alpha/\lambda^2 & \lambda > \lambda_P \end{cases} \tag{IV.5}$$

where, assuming "excellent manufacturing quality", the corresponding value of Q is equal to 40, so that

$$\alpha = \frac{0.62}{1 + 1.91\left(\Delta w_\kappa / t\right)^{1.44}} \tag{IV.6}$$

$$\frac{\Delta w_\kappa}{t} = \frac{1}{40}\sqrt{\frac{R}{t}} \tag{IV.7}$$

$$\lambda_P = 1.581\sqrt{\alpha} \tag{IV.8}$$

For the case of bending loading, those provisions specify that Class 1 and 2 cross-sections have an ultimate moment capacity M_u equal to the plastic bending moment $M_P = \sigma_Y W_{pl}$, where W_{pl} is the plastic bending modulus of the cross-section. For Class 3 sections, M_u is specified equal to the elastic bending moment $M_Y = \sigma_Y W_{el}$, where W_{el} is the elastic bending modulus. Finally, for Class 4 CHS sections, M_u is specified equal to $\sigma_{x,Rk} W_{el}$, where the critical axial stress $\sigma_{x,Rk}$ is calculated from equations (IV.4) - (IV.8) above.

REFERENCES

American Institute of Steel Construction, 2005, *Steel Construction Manual,* Thirteenth Edition, AISC 325-05.

American Petroleum Institute, 1993. *Recommended Practice, Designing and Constructing Fixed Offshore Platforms – Load and Resistance Factor Design.* Recommended practice 2A-LRFD, 1st Edition, Washington, DC.

Aravas, N., 1987. *On the numerical integration of a class of pressure dependent plasticity models,* International Journal for Numerical Methods in Engineering, Vol. 24, pp. 1395-1416.

Argyris, J.H., Papadrakakis, M., Karapitta, L., 2002. *Elasto-plastic analysis of shells with the triangular element TRIC,* Computer Methods in Applied Mechanics and Engineering, Vol. 191, pp. 3613–3636.

Bardi, F.C., Kyriakides, S., 2006. *Plastic buckling of circular tubes under axial compression-part I: Experiments,* International Journal of Mechanical Sciences, Vol. 48, pp. 830-841.

Bardi, F.C., Kyriakides, S., Yun, H. D., 2006. *Plastic buckling of circular tubes under axial compression-part II: Analysis*, International Journal of Mechanical Sciences, Vol. 48, pp. 842-854.

Batterman, S. C., 1965. *Plastic buckling of axially compressed cylindrical shells*, AIAA Journal, 3, pp. 316-325.

Bouwkamp, J.G., Stephen, R.M., 1974. *Full-Scale Studies on the Structural Behavior of Large Diameter Pipe Under Combined Loading*, Report No. UC-SESM 74-1, University of California, Berkeley, Structural Engineering and Structural Mechanics.

Brush D.O., Almroth, B.O., 1975. *Buckling of bars, plates and shells*, McGraw Hill, New York, NY.

Christoffersen, J., Hutchinson, J.W., 1979. *A class of phenomenological corner theories of plasticity*, J. Mech. Phys. Solids**27**, pp. 465–487.

Corona, E., Kyriakides, S., 1988. *On the collapse of inelastic tubes under combined bending and pressure,* International Journal of Solids and Structures, 24(5), pp. 505-535.

Crisfield, M.A., 1983. *An arc-length method including line searches and accelerations*, International Journal for Numerical Methods in Engineering, 19, pp. 1269-1289.

Dvorkin, E. D., Pantuso, D., Repetto, E. A., 1995. *A formulation of the MITC4 shell element for finite strain elasto-plastic analysis,* Computer Methods in Applied Mechanics and Engineering, Vol. 125, pp. 17-40.

European Committee for Standardization, 2005. *Eurocode 3: Design of steel structures. Part 1-1: General rules and rules for buildings*, CEN EN 1993-1-1, Brussels.

European Committee for Standardization, 2007. *Eurocode 3: Design of steel structures. Part 1-6: Strength and Stability of Shell Structures*, CEN EN 1993-1-6, Brussels.

European Committee for Standardization, 2006. *Eurocode 3: Design of steel structures. Part 1-12: Additional rules for the extension of EN 1993 up to steel grades S700*, CEN EN 1993-1-12, Brussels.

Gellin, S., 1979. *Effect of an axisymmetric imperfection on the plastic buckling of an axially compressed cylindrical shell,* ASME J. Appl. Mech. 46, pp. 125–131.

Hencky, H., 1924. *Zur Theorie plastischer Deformationen und der hierdurch im Material hervorgerufenen Nachspannungen,* Z. Angew. Math. Mech., Vol. 4, pp. 323–334 (1924).

Houliara, S., Karamanos, S.A., 2006. *Buckling and post-buckling of pressurized thin-walled elastic tubes under in-plane bending*, International Journal of Nonlinear Mechanics, 41, 4, pp. 491-511.

Houliara, S., Karamanos, S.A., 2010. *Stability of long transversely-isotropic elastic cylindrical shells under bending*, International Journal of Solids and Structures, Vol. 47, No. 1, pp. 10-24.

Hughes, T.J.R., Shakib, F., 1986, *Pseudo-corner theory: A simple enhancement of J_2 - flow theory for applications involving non-proportional damping*, Eng. Comput. Vol.3, pp.116-120.

Hutchinson, J.W., 1974. *Plastic buckling,* Advances in Applied Mechanics, Vol. 14, pp. 67-144.

Jaspart, J.-P. *et al.*, (2012). *Performance-based approaches for high strength tubular columns and connections under earthquake and fire loadings*, project ATTEL final report, RFCS, European Commission, Brussels, Belgium (http://bookshop.europa.eu/).

Jiao H., Zhao X.-L. (2003). *Imperfection, residual stress and yield slenderness limit of very high strength (VHS) circular steel tubes*, Journal of Constructional Steel Research, Volume 59, Number 2,pp. 233-249.

Ju, G.T., Kyriakides, S., 1992. *Bifurcation and localization instabilities in cylindrical shells under bending II: predictions*, International Journal of Solids and Structures, Vol. 29, pp. 1143-1171.

Karamanos, S. A., 2002. *Bending instabilities of elastic tubes*, International Journal of Solids and Structures, 39, 8, pp. 2059-2085.

Karamanos, S. A., Tassoulas, J. L., 1991. *Stability of Inelastic Tubes Under External Pressure and Bending*, J. Engineering Mechanics, ASCE, Vol. 117, No. 12, pp. 2845-2861.

Karamanos, S.A., Tassoulas, J.L., 1996. *Tubular members I: stability analysis and preliminary results*, *Journal of Engineering Mechanics*, ASCE, **122**, 1, pp. 64-71.

Karcher, G.G., Monte Ward, P. E., Spoelstra, G. P., 2009. *Buckling of Cylindrical, Thin Wall, Trailer Truck Tanks and ASME Section XII,* J. Pressure Vessel Technol *135(4).*

Koiter, W. T., 1963. *The effect of axisymmetric imperfections on the buckling of cylindrical shells under axial compression*, Koninkl. Nederl. Akademie van Wetenschappen, Amsterdam, Ser. B, Vol. 66, No. 5.

Kuroda, M., Tvergaard, V., 2001. *A phenomenological plasticity model with non-normality effects representing observations in crystal plasticity.* Journal of the Mechanics and Physics of Solids, Vol 49, pp. 1239–1263.

Kyriakides, S., Corona, E., 2007, *Mechanics of Offshore Pipelines*, Vol. I Buckling and Collapse, Elsevier.

Kyriakides, S., Ju, G. T., 1992. Bifurcation and localization instabilities in cylindrical Shells under bending I: Experiments, International Journal of Solids and Structures, Vol. 29, pp. 1117-1142.

Lee, L. N. H., 1962. *Inelastic buckling of initially imperfect cylindrical shells subjected to axial compression*, Journal of Aerospace Science29, pp. 87–95.

Lubliner, J., 1990. *Plasticity Theory*, Macmillan Publishing Comp., New York.

Malvern, L.E., 1969. *Introduction to the Mechanics of a Continuous Medium*, Prentice-Hall, Englewood Cliffs, NJ.

Mikkelsen, L. P., 1995. *Elastic-viscoplastic buckling of circular cylindrical shells under axial compression*, Eur. J. Mech. A/Solids14, pp. 901–920.

Nagtegaal, J. C., 1982. *On the Implementation of Inelastic Constitutive equations with Special Reference to Large Deformation Problems*, Comp. Methods Appl. Mech. & Engrg., Vol. 33, pp. 469-484.

Neale, K.W., 1981. *Phenomenological constitutive laws in finite plasticity,* Solid Mechanics Archives 6, 79.

Needleman, A., 1982. *Finite elements for finite strain plasticity problems*, Plasticity of Metals at Finite Strain: Theory, Experiment and Computation, edited by E.H. Lee and R.L. Mallet, Rensselaer Polytechnic Institute, Troy, New York, pp. 387-436.

Paraskevopoulos, E., Talaslidis, D., 2006. *Reduction of excessive energy in the four-noded membrane quadrilateral element. Part II: Near incompressibility and J_2 plasticity,* Computer Methods in Applied Mechanics and Engineering, Vol. 196, pp. 356-370.

Peek, R., 2000. *An incrementally continuous deformation theory of plasticity with unloading,* International Journal of Solids and Structures, Vol. 37, No 36, pp. 5009-5032.

Pournara, A. E.., Karamanos, S. A., Ferino, J., Lucci, A., 2012. *Strength and stability of high-strength steel tubular beam-columns under compressive loading.* 14th International Symposium On Tubular Structures, Paper No. 103, London, UK.

Reddy, D. B., 1979. A*n experimental study of the plastic buckling of circular cylinders in pure bending,* Int. J. Solids and Structures, Vol. 15, pp 669-685.

Rondal, J., Würker K.G., Dutta D. Wardenier J., Yeomans N., 1996, *"Structural stability of hollow sections"*, CIDECT (Ed.) and Verlad TÜV Rheinland.

Shaw, P. K., Kyriakides, S., 1985. *Inelastic Analysis of Thin-Walled Tubes Under Cyclic Bending*, International Journal of Solids & Structures, Vol. 21, pp.1073-1100.

Simo, J. C., 1987, *A J_2 - flow theory exhibiting a corner-like effect and suitable for large-scale computation*, Computer Methods in Applied Mechanics and Engineering, Vol. 62, pp.169-194.

Simo, J. C., Hughes, T. J. R., 1998. *Computational Inelasticity,* Springer, New York.

Simo, J. C., Taylor, R. L, 1985. *Consistent Tangent Operators for Rate Independent Elasto-Plasticity*, Computer Methods in Applied Mechanics and Engineering, Vol. 48, pp.101-118.

Simo, J. C., Taylor, R. L, 1986. *Return Mapping Algorithm for Plane Stress Elastoplasticity*, International Journal for Numerical Methods in Engineering, Vol. 22, pp.649-670.

Ting, T. C. T., 1985. *Determination of $\mathbf{C}^{1/2}$, $\mathbf{C}^{-1/2}$ and more general isotropic tensor functions of $\mathbf{C}$.* J. Elasticity, 15(3):319–323.

Tutuncu I, O'Rourke T., D., 2006. *Compression behavior of nonslender cylindrical steel members with small and large-scale geometric imperfections,* ASCE Journal of Structural Engineering, pp. 1234 - 1241.

Tvergaard, V., 1983. *Plastic buckling of axially compressed circular cylindrical shells*, Thin-Walled Structures**1**, pp. 139–163.

Tvergaard, V., Needleman, A., 1983. *On the development of localized buckling patterns*, in Collapse: The Buckling of Structures in Theory and Practice, (ed. by J. M. T. Thompson and G. W. Hunt), Cambridge University Press, 1-17.

Van Foeken, R., J., Gresnigt, A., M., 1994. *Effect of buckling deformations on the burst pressure of pipes,* TNO, 94-CON-R1008, Rijswijk, The Netherlands.

Vazouras, P., Karamanos, S. A., Dakoulas, P., 2010. *Finite element analysis of buried steel pipelines under strike-slip fault displacements*, Soil Dynamics and Earthquake Engineering, Vol. 30, No. 11, pp. 1361-1376.

Vazouras, P., Karamanos, S. A., Dakoulas, P., 2012. *Mechanical Behavior of Buried Steel Pipes Crossing Active Strike-Slip Faults,* Soil Dynamics and Earthquake Engineering, Vol. 41, pp. 164-180.

Vazouras, P., Dakoulas, P., Karamanos, S. A., 2015. *Pipe–soil interaction and pipeline performance under strike–slip fault movements*, Soil Dynamics and Earthquake Engineering, Vol 72, pp. 48–65.

Yun, H., Kyriakides, S., 1990. *On the beam and shell modes of buckling of buried pipelines,* Soil Dynamics and Earthquake Engineering, Vol 9, No 4, pp.179-193.

Zimmerman, T.J.E., Stephens, M. J., DeGeer, D. D., and Chen, Q., 1995. *Compressive Strain Limits for Buried Pipelines*, Offshore Mechanics and Arctic Engineering Conference, Vol. V, Pipeline Technology, pp. 365-378.